UNIVERSITY OF OKLAHOMA

GRADUATE COLLEGE

CATALYTIC ACYLATION, HYDROGENATION AND

HYDRODEOXYGENATION OF LIGNIN-DERIVED AROMATIC MOLECULES

A DISSERTATION

SUBMITTED TO THE GRADUATE FACULTY

in partial fulfillment of the requirements for the

Degree of

DOCTOR OF PHILOSOPHY

By

NHUNG N DUONG
Norman, Oklahoma
2018

CATALYTIC ACYLATION, HYDROGENATION AND
HYDRODEOXYGENATION OF LIGNIN-DERIVED AROMATIC MOLECULES

A DISSERTATION APPROVED FOR THE
SCHOOL OF CHEMICAL, BIOLOGICAL AND MATERIALS ENGINEERING

BY

_____
Dr. Daniel E. Resasco, Chair

_____
Dr. Ronald Halterman

_____
Dr. Lance L. Lobban

_____
Dr. Steven P. Crossley

_____
Dr. Bin Wang

Xin dành tặng ba mẹ yêu quý.

To my beloved family.

Acknowledgements

I want to thank all my friends that have always been by my side in the hard moments and shared with me wonderful life and work experiences: Huong, Uyen, Yen, Thong, Son, chi Tu, Dachuan, Cristian, Gap, Zheng, Lu, Taiwo, Abhishek, Valeria, Santiago, Nick, Lawrence, Felipe, anh Tuong, anh Ngoc, anh Minh, chi Van Anh… They have brought a lot of love and laugh to my life, making my life as OU more enjoyable and memorable.

Table of Contents

vii

List of Tables

List of Figures

Abstract

Lignin-derived phenolic molecules are studied for three different chemistries including acylation, hydrogenation and hydrodeoxygenation. Acylation is an effective C-C bond forming reaction to condense acetic acid and lignin-derived aromatic compounds into acetophenones, valuable precursors to fuels and chemicals. However, acetic acid is intrinsically an ineffective acylating agent. Here, we report that its acylation activity can be greatly enhanced by forming intermediate aromatic esters, directly derived from acetic acid and phenolics. Additionally, the acylation reaction was studied in the liquid phase over acid zeolites and was found to happen in two steps, (1) formation of an acylium ion and (2) C-C bond formation between acylium ion and the aromatic substrate. Each one of these steps can be rate-limiting, depending on the type of acylating agent and aromatic substrate. The O-containing substituents such as -OH and $-OCH_3$ can activate aromatic substrates for step (2), with $-OH > -OCH_3$, while alkyl substituent $-R$ cannot. At the same time, the aromatic esters can rearrange to acetophenones via both an intramolecular pathway and, preferentially, an intermolecular one.

Next, the interaction of phenolic molecules with metal surfaces are investigated via two different chemistries: hydrogenation (HY) and hydrodeoxygenation (HDO). Feeding m-cresol over Pt catalyst over a wide range of temperature from 110 to 350℃ shows that m-cresol conversion increases then decreases and later increases again with temperature. This non-linear Arrhenius relationship is found to not happen due to equilibrium limitation or poisoning but rather because of fast drop in m-cresol surface coverage as temperature increases. A Langmuir-Hinshelwood kinetic model is developed for HY reactions of m-cresol to 3-methylcyclohexanone and 3-methylcyclohexanol. Based on

this model, the intrinsic energy barrier for of hydrogenation of cresol to ketone is 31 kJ/mol, cresol to alcohol is 26 kJ/mol, ketone to alcohol is 28 kJ/mol. The adsorption enthalpy of *m*-cresol was found to be 76 kJ/mol with adsorption entropy of 124 J/molK. The binding energy of *m*-cresol on Pt surface was reported in the literature to be much higher, 180-220 kJ/mol. Based on the kinetic fitting, the adsorption enthalpy and entropy both suggest that the kinetically active species for m-cresol hydrogenation have weakly adsorbed configurations rather than strongly absorbed ones.

At temperature higher than 300℃ on Pt catalyst, *m*-cresol start to undergo C-O bond cleavage (HDO), creating toluene as the product. Therefore, the conversion of m-cresol starts to increase with temperature after 300℃. Previous studies of *m*-cresol HDO show that on metals of low oxophilicity, such as Pt or Pd, the direct C−O bond cleavage is not possible. Therefore, HDO requires an indirect pathway via tautomerization. By contrast, on metals of higher oxophilicity, such as Ru or Rh, the direct C−O bond cleavage is possible, and toluene can be directly obtained from *m*-cresol. These studies show that the HDO activity correlates directly with the metal oxophilicity, which in turn depends on the position of the d-band center relative to the Fermi level. This catalytic descriptor depends on (1) type of metal and (2) extent of coordination of the metal atoms. In the last part of this study, the effect of the second factor will be investigated. It is demonstrated that a Rh/SiO$_2$ catalyst with small particles (low coordination sites) is more active for HDO than one with larger particles (high coordination sites). At the same time, the low coordination site is more prone to deactivation and loss of HDO selectivity. These experimental results are combined with the DFT calculations, which show that the energy barrier for direct C−O bond cleavage is lower on a step site than on a terrace site. At the

same time, it is shown that a step site requires a higher energy barrier to remove adsorbed

molecular fragments to regenerate the activity than a terrace site, which explains the faster

deactivation rate observed on catalysts with small, more defective metal clusters.

Lignin-derived Phenolic Molecules in Biomass Conversion

Extensive use of fossil fuel in our modern life today has raised a lot of concerns from an environmental point of view due to excessive emission of CO_2 and other pollutants such as NO_x, SO_x... To solve this problem, biofuel is an attractive renewable energy resources because it has a lower net CO_2 emission with the ability to replace fossil fuel directly without the need to modify our current infrastructures. Among different types of biomass, lignocellulosic biomass is an attractive resource because of its abundance and low cost. Extensive research on lignocellulosic biomass conversion to renewable chemicals and fuels have been executed in recent years[2-9]. Lignocellulosic biomass is composed of three main components: hemicellulose, cellulose and lignin, in which lignin accounts for an important fraction (~23-33 wt% in softwood and 16-25 wt% in hardwood)[6, 10]. Among the three components, lignin has the highest decomposition temperature, at about 300-500℃, it will decompose to phenolic derivatives which are aromatic molecules with different oxygen functionalities such as –OH or –OR. In this current contribution, different chemistries are studied for the upgrading of these lignin-derived phenolic molecules in the process of converting biomass into fuels, including Acylation, Hydrogenation and Hydrodeoxygenation.

There are different ways to convert biomass to biofuel, in which one of the most common and inexpensive ways is starting from fast pyrolysis to get bio-oil followed by catalytic upgrading of bio-oil to obtain biofuel. Bio-oil is a complicated mixture, but in general, the compounds in bio-oil can be grouped into three different families: light oxygenates, sugar derivatives and lignin derivatives. Due to its high oxygen content, bio-

oil is very corrosive with a low heating value and thus cannot be used directly as fuel. Direct hydrotreating of bio-oil will produce mostly short chain C5-C6 hydrocarbons and light gases, which have low economic values. However, the oxygen content also makes bio-oil reactive for many different C-C coupling chemistries, which can be used to combine different families in bio-oil into longer chain molecules that are more suitable for fuel applications. Because of the complexity of the mixture, one pot upgrading of the whole bio-oil mixture is impossible because it contains a significant amount of small carboxylic acids (light oxygenates), which promotes side reactions, particularly polymerization of sugar derivatives, leading to catalysts deactivation and lower carbon yield to desirable products. Therefore, in the upgrading process, the first step is to separate these three different families into different streams, then apply different chemistries to convert them into more valuable products, which is illustrated in **Figure 1**.
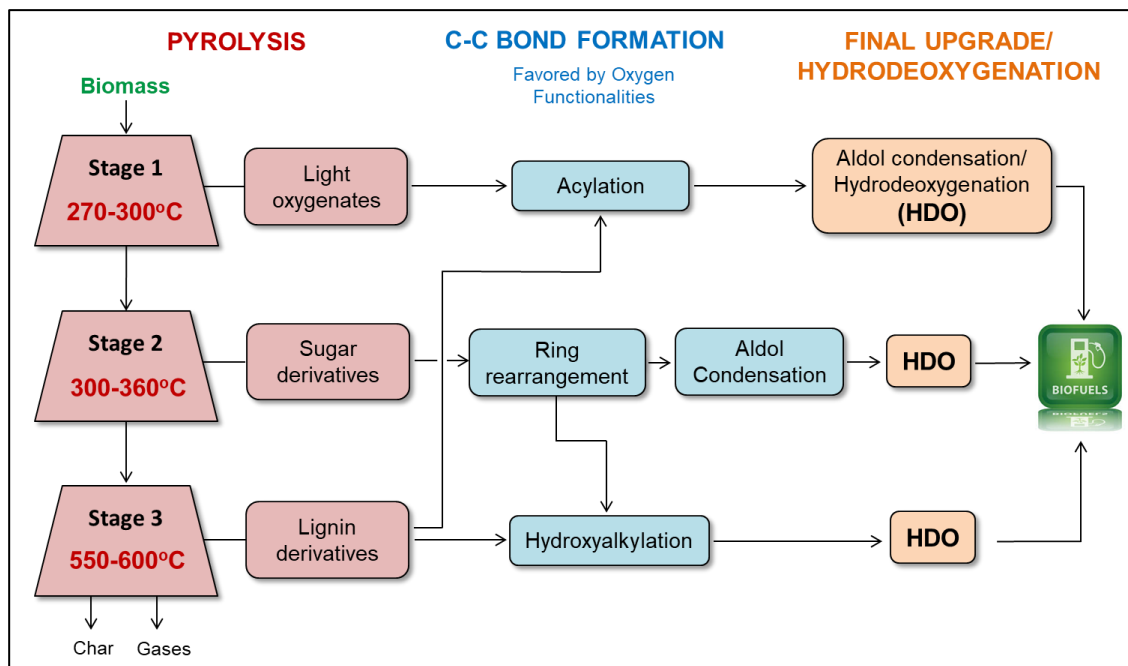
Figure 1. Multi-stage pyrolysis followed by catalytic cascade for biomass upgrading

Because different components of biomass decompose at different temperatures, we have proposed to use the pyrolysis temperature as a mean of separation. Biomass is pyrolyzed at different temperatures to produce different streams that are enriched in a particular chemical family. After that, the streams undergo different chemistries for C-C coupling, as further demonstrated in **Figure 2**, to create longer chain molecules before the final upgrade step of hydrodeoxygenation to remove oxygen and make fuel hydrocarbons.[11-12]
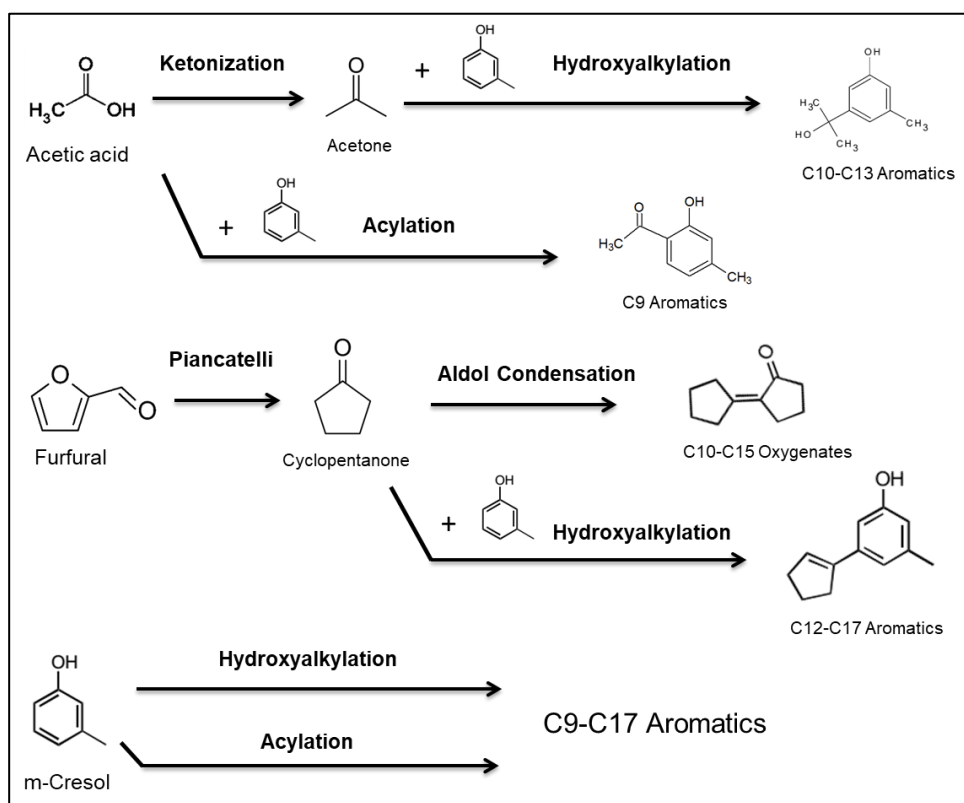
Figure 2. Different C-C coupling strategies in liquid phase

In chapter 1, the acylation of phenolic molecules is investigated as a potential C-C bond formation chemistry for liquid phase upgrading. The activity of different acylating

agents and phenolic substrates are compared in order to understand the reaction mechanism. Particularly, the possibility of using acetic acid as an acylating agent is also investigated, because acetic acid is another major component in bio-oil.

After the C-C bond formation steps, it is needed to remove oxygen from these phenolic molecules to convert them to hydrocarbons. The hydrodeoxygenation (HDO) reaction of phenolic molecules has been extensively studied with different type of metal catalysts such as metals[13-14], metal-zeolite bifunctionals[15] or metal carbides on both real pyrolysis bio-oil and model compounds. Therefore, to understand how the phenolic molecules interact with metal surfaces becomes very important.

Under hydrogen pressure, at high temperature (270°C and above) many metal catalysts (Pt, Rh, Ru, Ni, Fe…) are active for HDO of phenolics to alkyl aromatics. Besides HDO, these metals are also active for hydrogenation (HY) of the aromatic ring. Interestingly, the selectivity between HY vs HDO changes with temperature, as HY reactions are exothermic and thus limited by equilibrium at high temperature, while HDO becomes more dominant. Understanding the mechanism of both HDO and HY reactions will give insights on how the phenolic molecule interacts with metal surface over a wide range of temperature. For biomass conversion application purpose, HDO is the required final upgrading step to make fuel hydrocarbons, while many HY products of phenolics such as cyclic ketones and alcohols can be used as alkylating agents to create longer chain molecules or as precursors for polymer synthesis. HY study is presented in chapter 2 and HDO study is presented in chapter 3 of this work.

I. Acylation of Phenolic Molecules by Acetic Acid - Enhancement of Acetic Acid Activity by Forming an Intermediate Aromatic Ester

Motivation and Literature Reviews

Liquid phase upgrading of pyrolysis products is an important process in the conversion of lignocellulosic biomass to fuels.[16-21] The typical bi*o*-oil obtained by condensation of biomass pyrolysis vapors is an unstable liquid, which cannot be easily reheated for vapor phase upgrading or fractionation since this reheating would result in polymerization and significant carbon losses. The presence of light acids, consisting primarily of acetic acid, in these streams enhances polymerization reactions and favors corrosion upon storage. Acetic acid is the most abundant species in many biomass derived streams, for example, the liquid product from raw oak after torrefaction at 270°C contains 51% acetic acid on a dry basis.[22] Converting acetic acid to low value products by conventional hydrotreating would dramatically reduce the total renewable carbon that can be converted to gasoline/diesel range transportation fuels. Therefore, to prevent this loss and stabilize the mixture, different strategies involving C-C forming reactions have been developed to capture these reactive light acids into longer and more stable molecules. One approach that has been widely investigated involves the ketonization of acetic acid to acetone,[5, 7] followed by aldol condensation of acetone to form longer chain products[2] or hydrogenation of acetone to isopropanol followed by alkylation of isopropanol with phenolic compounds.[8] The major limitation of these two strategies is that the ketonization step results in a significant carbon loss due to the formation of one mole of CO_2 evolved

5

for every two moles of acetic acid converted. This results in a maximum theoretical carbon yield of only 75%. Another alternative that has been considered is the partial hydrogenation of acetic acid to ethanol followed by alkylation of ethanol with phenolic compounds. However, the hydrogenation of acetic acid requires high H_2 consumption and ethanol is an ineffective alkylating agent. Alternatively, acetic acid could be used directly as an acylating agent for phenolic compounds producing aromatic ketones that could be directly hydrotreated or further upgraded to longer chain molecules via aldol condensation. Since phenolic compounds derived from lignin also account for a large fraction of bi*o*-oil, this approach appears promising and might result in very high carbon capture in the fuel-range liquid.

Friedel-Crafts acylation of aromatics is a well-known and extensively investigated reaction in organic chemistry that produces aromatic ketones from an acylating agent and an aromatic substrate. Different acylating agents such as carboxylic acids, acyl halides or acyl anhydrides have been investigated, with acid catalysts including $AlCl_3$, HF, zeolites or heteropolyacids.[23-24] It has been recently shown that over H-ZSM5 at 220°C the vapor phase acylation proceeds via dehydration of acetic acid to form an acyl intermediate, in which acetic acid may well act as an acylating agent.[25] These intermediates can desorb as ketenes at elevated temperatures, resulting in catalyst deactivation. However, by incorporating an effective substrate such as methylfuran, selective direct acylation may result.[26] The selective acylation with highly active acyl acceptors have been proposed as intermediate compounds for the production of renewable specialty surfactants.[27]

In the condensed liquid phase, especially in the complex liquid environment of bi*o*-oil, the phenomena involved in acylation reactions may be more complicated due to solvent effects, mass transfer limitations, and catalyst deactivation by heavy products.[28-31] In the liquid phase, the acyl halides and anhydrides have shown to be effective acylating agents, in which the acylation reaction proceeds via formation of an acylium ion intermediate.[32-34] Also, it has been reported that Brønsted acid zeolites are more effective than Lewis acid zeolites for the acylation of furan by lauric anhydride.[27] However, with acetic acid as the acylating agent, the reaction mechanism in liquid phase still remains elusive. For example, it is unclear whether the reactive intermediate is an acylium ion, as in the vapor phase reaction[35-36] or it involves a Lewis-coordinated carboxylic acid species.[32] The nature of the rate-limiting step in the liquid phase is equally debatable. Some studies[30] have proposed that the C-C bond formation is rate-limiting, while others have found significant overall rate differences when varying the acylating agent, suggesting that formation of the reactive intermediate is the rate-limiting step.[37] To shed more light into this important reaction, the present contribution investigates the nature of the most crucial intermediates and attempts to determine the rate controlling steps.

Furthermore, since the lignin-derived aromatic compounds have very diverse structures, which ultimately are combinations of different substituents on the aromatic ring, the reactivity of different aromatic substrates has been investigated. It is expected that the ring substituents should have an important impact on the electrophilic substitution reaction of the intermediate species with the aromatic ring. Regardless of the complexity of the lignin-derived aromatic mixture, in general, the substituents can be separated into

three main groups, including hydroxyl –OH, alkoxy –OR and alkyl –R substituents on the aromatic ring. Model compounds with each functional group are systematically studied here to provide insight into the effects of said substituents on the activity and selectivity for acylation. Therefore, by independently changing the nature of the acylating agent and the aromatic substrate we have attempted to elucidate the relative importance of the potential rate controlling step(s), formation of the active intermediate or C-C bond formation, under different reaction conditions.

It must be noted that when acetic acid is used as a reactant in the presence of phenol or phenol-derivatives over zeolite catalysts, it produces aromatic esters. They can undergo isomerization to a hydroxyaromatic ketone, a reaction known as Fries rearrangement.[38-39] A quantitative comparison of the activity between these esters and acetic acid for the acylation reaction has not yet been attempted. Furthermore, there are two possible paths for the Fries rearrangement reaction, one intramolecular and the other intermolecular. Early work assumed that orth*o*-hydroxyaryl ketones are formed via the intramolecular pathway, while the para isomer is formed via intermolecular interactions. However, recent studies have shown that the mechanism may be more involved than this simple description.[23] Here, we have investigated the Fries rearrangement reaction in the liquid phase with both, aromatic esters and aromatic substrates present in the feed, and have compared the yields of ortho and para isomers under different reaction conditions to quantify the contribution of each pathway.

Catalyst Characterization

The Brønsted acid density of the three zeolites was determined by temperature program desorption (TPD) of isopropyl amine (IPA). The other physical characteristics of these catalysts have been studied by XRD, SEM, and DRIFTS. These characteristics, along with detailed experimental procedures have been reported elsewhere. [8, 17, 25]

Results and Discussion

1. Nature of acylating agent

1.1.   Acylation of m-cresol by acetic acid (AA)

1.1.1.   Performance of different zeolites

The acylation of *m*-cresol by acetic acid was tested over three different zeolites, H-ZSM5, HY and H-Beta. **Table 1** reports the measured BET areas and acid site densities for each sample.

Table 1: Characterization of the zeolites

Zeolite	Surface area[a] (m^2/g)	Brosted acid sites density (mmol/g)
H-ZSM5 (Si/Al=25)	425	0.74
HY (Si/Al=30)	720	0.29
H-Beta (Si/Al=19)	710	0.54

[a] According to the manufacture

As shown in **Table 2**, only two measurable products, *m*-tolyl acetate and 2'-hydroxy-4'methylacetophenone (HMAP), were obtained from *m*-cresol and acetic acid. The former is an esterification product while the latter is an acylation product. Trace amounts

of 2,2-bis(4-hydroxy-2-methylphenyl)propane were observed, as previously reported by

Rohan *et al.* and Vogt *et al* [28-29, 38].

Acetic Acid   *m*-Cresol   HMAP   *m*-Tolyl Acetate
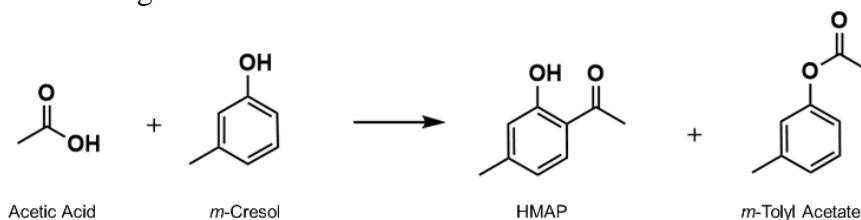
Table 2: Conversion and yields to acylation (2'-hydroxy-4'methylacetophenone - HMAP) and esterification (m-tolyl acetate) products from the reaction of m-cresol and acetic acid over different zeolites. Reaction conditions: 1g zeolite in 80ml of 1M acetic acid with 8M m-cresol, 250℃, 1hr

Zeolite	Pore Size (nm)	Selectivity of HMAP	Selectivity of *m*-tolyl acetate
H-ZSM5 (Si/Al=25)	0.55-0.56	47%	53%
HY (Si/Al=30)	0.66-0.67	65%	35%
H-Beta (Si/Al=19)	0.74	70%	30%

In line with previous studies,[40-41] at similar acetic acid conversion (50-60%), H-Beta

gives somewhat higher selectivity to the desired acylation product (HMAP) than HY and

even higher than H-ZSM5. The difference in product selectivity might be ascribed to the

pore size of the zeolites. That is, the catalysts with larger pores (HY and H-Beta) result

in higher selectivity toward the acylation product HMAP, as compared to the one with

smaller pore size (H-ZSM5), which favors the formation of the ester, an easier reaction

that probably can occur on the external surface, and partly homogeneously in the liquid

phase, as shown below. Due to its higher selectivity to the desirable product, HMAP, H-

Beta was selected as the preferred catalyst to study the acylation reaction in greater detail.

1.1.2.   *Role of the aromatic ester as an effective acylation intermediate*

To identify the primary and secondary products, we followed the product distribution as a function of the extent of reaction in the batch reactor. However, since the catalyst deactivation was found to be significant (**Figure 3**) to accomplish different extents of reaction the activity runs were carried out for a fixed 1 hour period over varying amounts of catalyst, as shown in **Figure 4**.
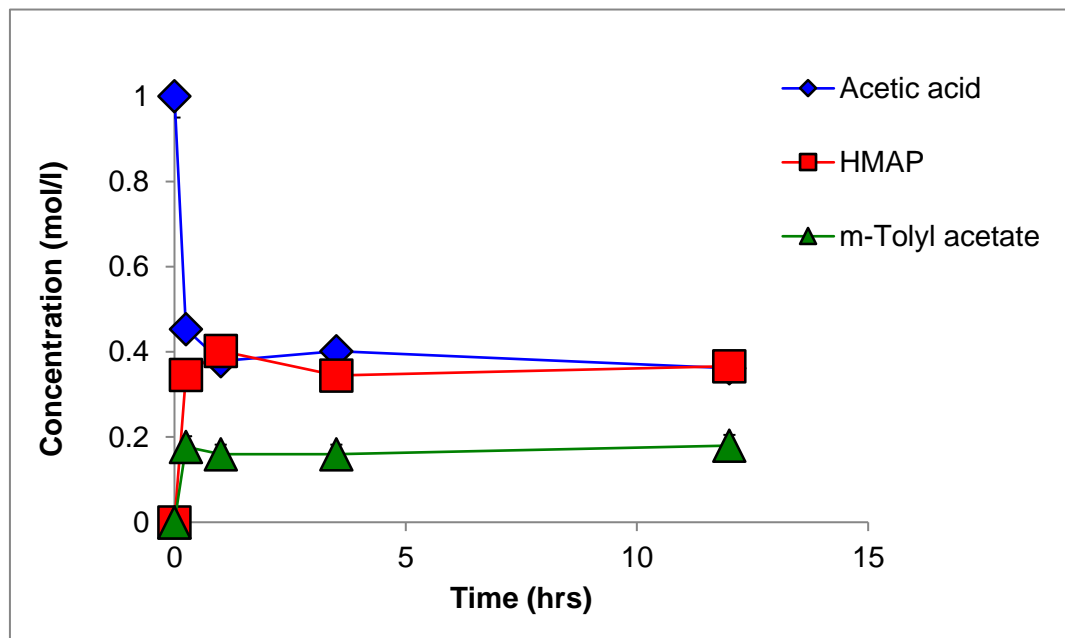
Figure 3. The concentration of products and acetic acid over different reaction time. Reaction conditions: 1M acetic acid with 8M m-cresol, 250℃, 1g H-Beta
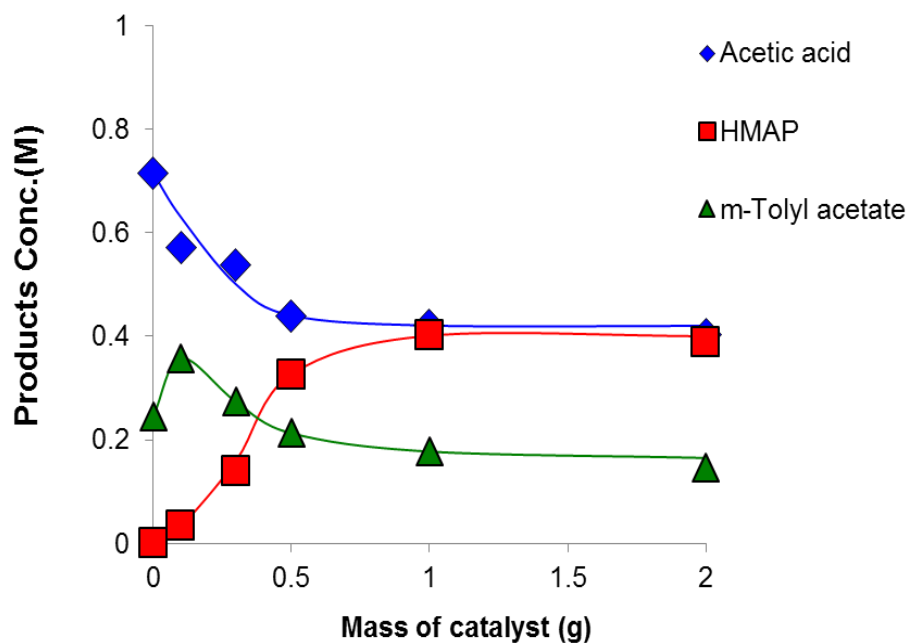
Figure 4. The concentration of products and acetic acid over different amount of H-Beta. Reaction conditions: 1M acetic acid with 8M m-cresol, 250°C, 1hr

It can be observed that formation of the *m*-tolyl acetate ester was observed even without a catalyst, which indicates that esterification to *m*-tolyl acetate is self-activated by the acetic acid in the liquid phase. However, as the amount of catalyst increased from zero to 1 g, larger amounts of *m*-tolyl acetate were observed, indicating that esterification is catalyzed by the zeolite. Interestingly, the concentration of the ester gradually decreased with the extent of reaction, which shows that the ester is further converted. The desirable product HMAP is seen to continuously increase from zero without a catalyst, slowly at low extent of reaction (small amount of catalyst), and more rapidly at high extent of reaction (larger amount of catalyst). This trend suggests that HMAP is a secondary product, presumably involving the *m*-tolyl acetate ester, initially formed. To

further support this hypothesis, the acylation activity of acetic acid was compared to that of *m*-tolyl acetate over a small amount of zeolite Beta of 0.1g, as shown in **Figure 5.** It is clearly shown that, under the same reaction conditions, the yield of HMAP from *m*-tolyl acetate (14 %) is significantly higher than that from acetic acid (3%).

Kumari et al. has compared the acylation activity of acetic acid vs. acetic anhydride for phenol acylation reaction in the vapor phase over zeolite Beta[37], in which acetic anhydride was shown to be more active than acetic acid. At temperature of 250°C and similar phenol/acylating agent ratio, the yield of acylation from acetic anhydride is five times higher than that of acetic acid, which is about the same order of difference as m-tolyl acetate vs. acetic acid acylation yield as shown in **Figure 5**.
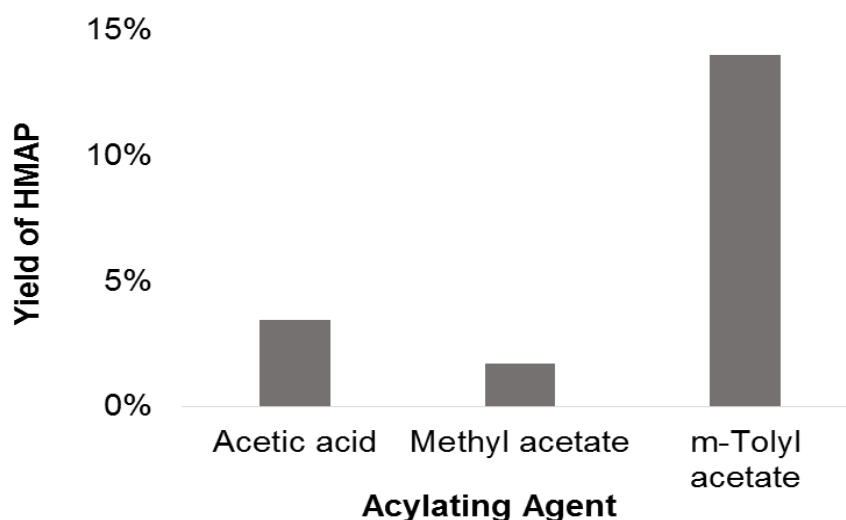
Figure 5. The yield HMAP with different acylating agents. Reaction conditions: 1M acylating agent in m-cresol, 250°C 0.1g HBeta 1hr
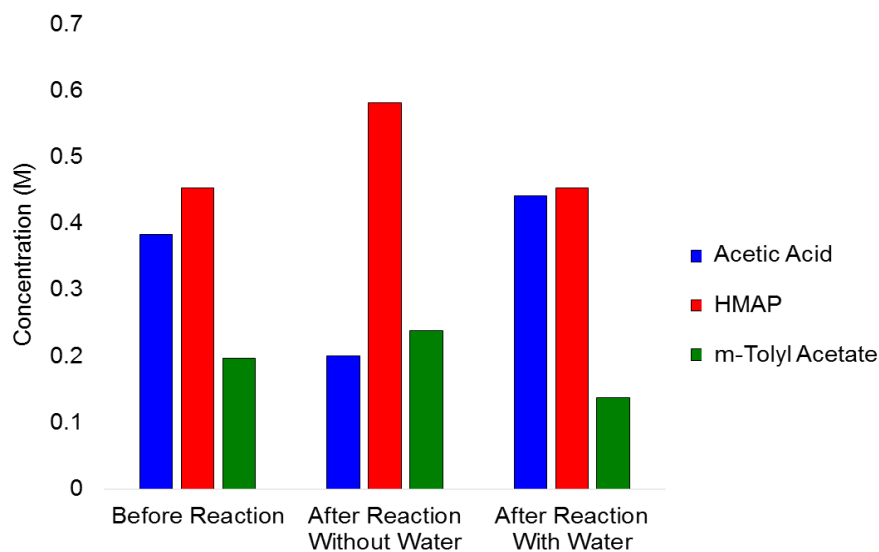
Figure 6. Concentration of acetic acid, 2'-hydroxy-4'-methylacetophenone (HMAP) and *m*-tolyl acetate before and after equilibrium test. Reaction conditions: 80ml solution of 0.38 M acetic acid, 0.45 M HMAP and 0.2 M *m*-tolyl acetate with 1g H-Beta Si/Al=19, 250°C 1hr.

1.1.3.   Reverse reaction and equilibrium limitations

As shown in **Figure 4**, when the mass of catalyst was larger than about 1g, there was no further change in product distribution, indicating that the reaction reached equilibrium. To investigate the reversibility of the reaction, a mixture of acetic acid, HMAP, and *m*-tolyl acetate at the same composition of that reached after 1 h reaction was prepared (0.38 M acetic acid, 0.45 M HMAP and 0.2 M *m*-tolyl acetate). The only difference between this prepared mixture and the reaction mixture is that no water was present, while water is produced during reaction. Therefore, when this mixture was exposed to 1 g of fresh H-Beta catalyst, an additional production of HMAP was observed, showing the role of water in the reverse reaction. Water can easily react with acetyl ion to form acetic acid and water would compete with aromatic substrate (*m*-cresol) to pick up with acetyl ion, thus inhibit the formation of HMAP. In fact, as shown in **Figure 6,** when the same mixture

14

was prepared with added excess water, no additional HMAP was obtained either, but only a slight conversion of the *m*-tolyl acetate to acetic acid.

1.2.   Acylation activity of different esters with m-cresol

After showing that aromatic esters are effective acylating agents, we tested the reactivity of an alkyl ester (methyl acetate) to assess the importance of the aromatic group in the effectiveness of the acylating agent. It is possible that the presence of the aromatic ring affects the ester dissociation during the formation of the active intermediate species, affecting the acylating rate. Indeed, as seen in **Figure 5**, methyl acetate is a much less effective acylating agent than the aromatic ester, resulting in only 2% acylation yield (HMAP), compared to *m*-tolyl acetate which results in 14% yield.

Interestingly, as shown in **Figure 7**, the evolution of the HMAP yield shows an initial slow increase with increasing extent of reaction, but the variation is more pronounced at higher extent of reaction, reaching a relatively high concentration (0.27 M). This behavior indicates that HMAP is not a primary product but rather a secondary product from *m*-tolyl acetate, a transesterification product of methyl acetate and *m*-cresol. The concentration of *m*-tolyl acetate remains constant with increasing mass of catalyst, which means that it is consumed and produced at similar rates. This phenomenon is similar to

15

the case of acetic acid shown above, in which acetic acid was not active but it underwent

esterification with *m*-cresol to create an aromatic ester that has high acylation activity.
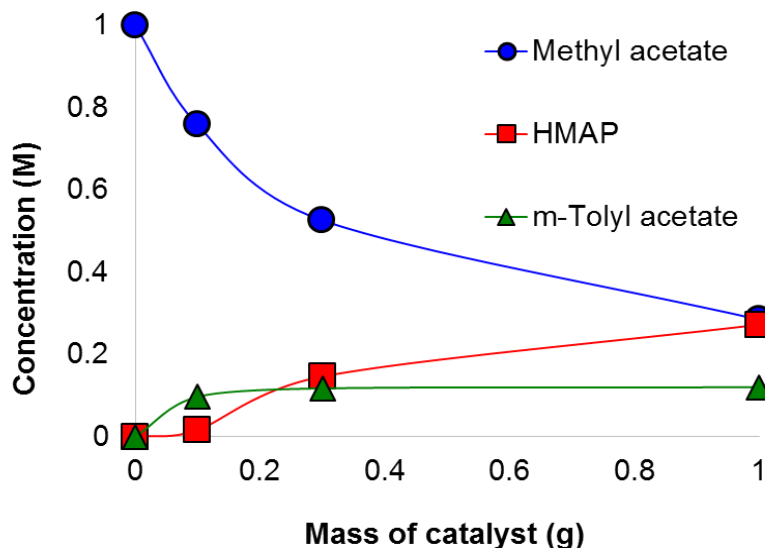
Figure 7. The concentration of products and methyl acetate over different amount of H-Beta.
Reaction conditions: 1M methyl acetate with 8M m-cresol 250°C 1hr.

As mentioned above, until now the nature of the electrophilic intermediate species

was unclear, since both an acylium ion and a Lewis-coordinated acetic acid have been

proposed in the literature.[35-37] Here, our results clearly show that acetic acid by itself is

not an active acylating agent, but rather it requires the formation of an aromatic ester,

which rules out the possibility that the Lewis-coordinated acetic acid is the active

intermediate. Furthermore, being a much bulkier compound, coordination of an aromatic

ester on zeolite Lewis acid to generate an active electrophilic intermediate would be less

likely due to steric hindrance, which would inhibit the approach of an aromatic substrate.

Therefore, a more plausible pathway is one in which the aromatic ester generates an

acylium ion, which couples with the aromatic substrate. Since both, acetic acid and

aromatic esters can form acylium ions, the much higher rate observed with the latter
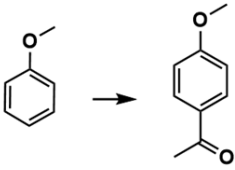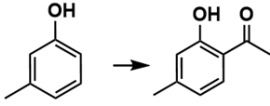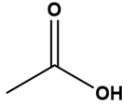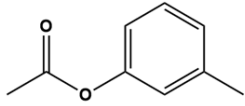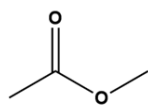
would indicate that they can form acylium ions much more rapidly than the former. These results agree with DFT-calculated activation barriers for formation of acylium ion from acetic acid, *m*-tolyl acetate and methyl acetate (see section 4, below).

1.3. Acylation of anisole by different acylating agents over H-Beta

Anisole does not have a free phenolic –OH substituent, thus it is not able to form directly an aromatic ester with acetic acid. By contrast, when the substrate is *m*-cresol, acetic acid and methyl acetate can form an aromatic ester, which has a higher acylation activity. The comparison of the acylation rate between anisole and *m*-cresol with different acylating agents will help confirm the role of the aromatic ester. The acylation product of anisole is *p*-methoxyacetophenone (*p*-MXAP).

Indeed, as shown in **Table 2**, the acylation rate with *m*-cresol was much higher than with anisole when acetic acid and methyl acetate were the acylating agents (40% and 27% *vs.* 4%). This significant difference in activities is attributed to the ability of *m*-cresol to undergo esterification with acetic acid and transesterification with methyl acetate to form *m*-tolyl acetate, a more efficient acylating agent. When *m*-tolyl acetate was used as the acylating agent, the acylation yield of anisole improved to 30%, compared with 4% in the case of acetic acid and methyl acetate, which proves again the high acylation activity of the aromatic ester.

Table 3. Yield of acetylated products of different aromatic substrates by different acylating agents, *p*-MXAP from anisole and HMAP from *m*-cresol. While *P*-methoxyacetophenone (*p*-MXAP) and its isomer (*o*-MXAP) were observed in the acylation of anisole, *o*-MXAP only appeared in negligible amounts. Reaction conditions: 1M acylating agent with 8M of aromatic substrate, 1g HBeta Si/Al=19, 250^{0}C 1hr.

Acylating agent / Phenolic substrate	Anisole → p-MXAP	m-cresol → HMAP
Acetic acid	4%	40%
m-cresyl acetate	21%	52%
methyl acetate	4%	27%

The simultaneous conversion of acetic acid and anisole on H-ZSM5 has been previously reported in the literature with *p*-MXAP as the dominant product.[42] However, in the present work, *p*-MXAP remains almost insignificant (less than 5% yield) across the broad ranges of temperature (145-250°C), time (1-18 hrs), and catalyst amount (H-Beta 1-5g) investigated.

2. *Nature of aromatic substrate*

As described above, the acylation reaction follows a tw*o*-step mechanism (1) formation of acylium ion and (2) C-C coupling between the acylium ion and the aromatic substrate. The second step is an electrophilic substitution reaction, in which the substituents in the aromatic ring may have an activating or a deactivating effect. For example, substituents such as –OH, –OR, –R are known to be activating, and *o-, p-*

directing due to their ability to stabilize the carbocation intermediate.[43] We have investigated the effect of the –OH, –OCH$_3$ and –CH$_3$ substituents by using phenol, anisole, and toluene, respectively, and *m*-cresol to study the combination of –OH and –CH$_3$ substituents.

2.1. *Comparison acylation rates of anisole (–OCH$_3$) and toluene (–CH$_3$)*

It is clear that aromatic esters are effective acylating agents. Therefore, in this section, phenyl acetate was used as the common acylating agent to compare the activity of different aromatic substrates, i.e. anisole *vs.* toluene. The product yields and aromatic ester consumption are compared in the **Table 4**. Under identical reaction conditions, the yield of acylated anisole is about twenty times higher than that of acylated toluene, in agreement with previous results by Derouane *et al.*[30], who reported the same trend when using acetic anhydride as the acylating agent. It is interesting that while the acylation rate is affected by the type of acylating agent, when the acylating agent is very effective, the rate is also affected by the nature of the aromatic substrate.

Table 4. Product yield for the acylation of anisole (p-MXAP: p-methoxyacetophenone) and toluene (MAPs: o- and p-methylacetophenone) with phenyl acetate ester as acylating agent, along with HAPs (o- and p-hydroxy acetophenones) and o-AXAP (o-acetoxyacetophenone) arising from rearrangement of phenyl acetate. Reaction conditions: 80ml 1M phenyl acetate in anisole or toluene, 0.1g H-beta 250°C 1hr

	Anisole	Toluene
p-MXAP (from anisole)	19%	-
MAPs (from toluene)	-	1%
HAPs and AXAP	4%	4%
Unbalanced phenyl acetate (%)	0	6%
Total Yield	23%	5%
Conversion of phenyl acetate (%)	23%	11%

In addition to the acylation, other products have been observed, including *o*-HAP, *p*-HAP and *o*-AXAP, which can result from the Fries rearrangement of phenyl acetate. They had similar total yield in both cases (anisole and toluene), which suggests that these products do not derive from acylation of toluene or anisole feed. In the case of anisole, the conversion of phenyl acetate is equal to the yield of acylated products, i.e. the total carbon balance is 100%. By contrast, in the case of toluene, more than half of the phenyl acetate converted was missing from the measurable products. This low carbon balance suggests that a significant fraction of the acetyl ions formed from the aromatic ester cannot be efficiently picked up by toluene and they may be further converted to ketene (via dehydration) and subsequently to coke, which lowers the total liquid yield. It worth to mention that the carbon balance for all of the other results that are reported in this study is as high as more than 90%.

2.2. *Comparison of anisole (–OCH₃), phenol (–OH) and m-cresol (–OH + –CH₃) as aromatic substrates with single and double substituent*

To compare the activity of phenol, anisole and m-cresol, we had to use two aromatic esters. One might presume that the most straightforward way to compare the activity of different substrates would be using the same aromatic ester under the same reaction conditions, as we have done in the previous section. However, the higher complexity of the reactions involving these three aromatic substrates makes the comparison more problematic. For example, phenol and m-cresol can undergo transesterification with any aromatic ester and form phenyl and m-tolyl aromatic esters, respectively, through their -

20

OH group. Consequently, depending on the aromatic substrate and acylating agent, a mixture of two aromatic esters will be generated in the reaction mixture. For example, if the aromatic substrate is m-cresol and the acylating agent is phenyl acetate, m-tolyl acetate will be produced. Likewise, if phenol is the aromatic substrate and the acylating agent is m-tolyl acetate, phenyl acetate will be generated. Thus, in both cases, an uncertainty due to the potentially different activity of the two aromatic esters would be created in the rate of the first step (acylium ion forming), which would make the comparison invalid. In order to avoid this complexity, we have used mixtures of phenol and anisole with phenyl acetate (which has no methyl group) as the acylating agent. Likewise, we have used mixtures of m-cresol and anisole with m-tolyl acetate (which has one methyl group in the m-position) as the acylating agent. In this way, the impact of transesterification will be eliminated.
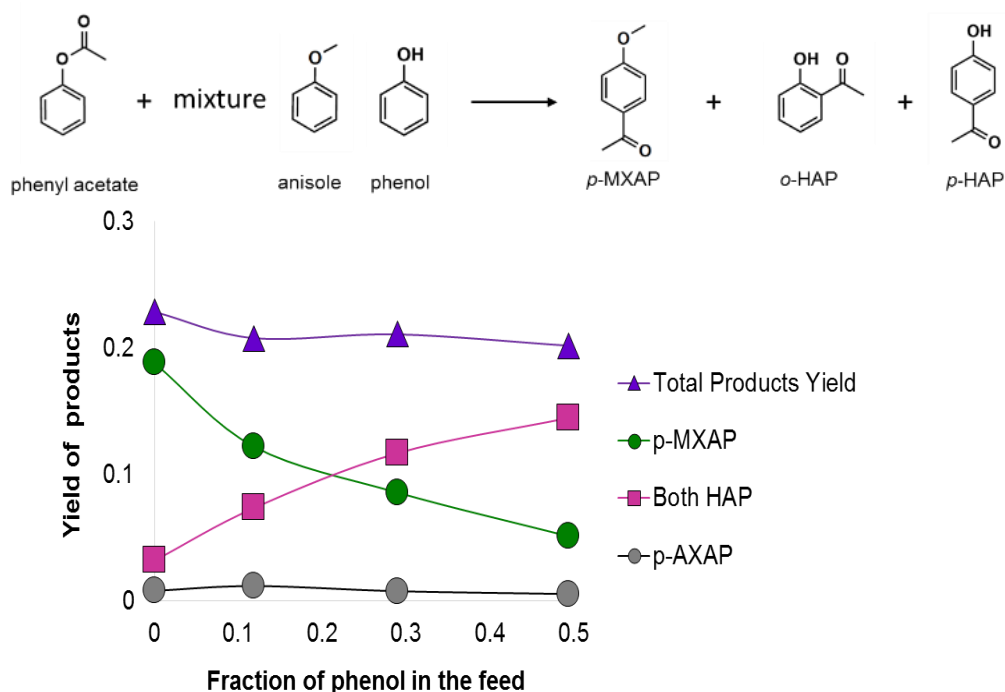
Figure 8. Product distribution vs. fraction of phenol in the feed. Reaction conditions: 1M phenyl acetate in mixture of phenol and anisole, 0.1g H-Beta with 80ml feed, 1hr 250°C

21

Reactions of pure anisole with the two aromatic esters reveal that phenyl acetate results in approximately a factor of two higher yield of acylated anisole than *m*-tolyl acetate. Then, to compare the relative activity of the different aromatic substrates, anisole was used as the reference since it was run simultaneously with phenol or with *m*-cresol. In **Figure 8**, the yield of acylation products obtained by using phenyl acetate as acylating agent was plotted versus fraction of phenol in the aromatic substrates feed. As shown in the scheme below, the acetylated products from anisole is *p*-methoxyacetophenone (*p*-MXAP) and the ones from phenol are *o*-hydroxyacetophenone (*o*-HAP) and *p*-hydroxyacetophenone (*p*-HAP).

A minor product of this reaction is *p*-acetoxyacetophenone (*p*-AXAP), which is the coupling product between phenyl acetate and acetyl ion. It has been previously proposed[44] that *o*-HAP is a primary product from the intramolecular rearrangement of phenyl acetate, and that *p*-HAP is a secondary product formed via hydrolysis of *p*-AXAP. However, our results show that the amount of *p*-HAP increases proportionally with the phenol in the feed, while *p*-AXAP is independent of the phenol concentration. Therefore, the formation of *p*-HAP cannot be directly linked to the hydrolysis of *p*-AXAP.

In **Figure 9**, the yield of acylation products obtained by using *m*-tolyl acetate as acylating agent was plotted versus fraction of *m*-cresol in the aromatic substrates feed. As shown in the scheme below, the acetylated product from anisole is *p*-methoxyacetophenone (*p*-MXAP) and the one from *m*-cresol is 2'-hydroxy-4'-methylacetophenone (HMAP).
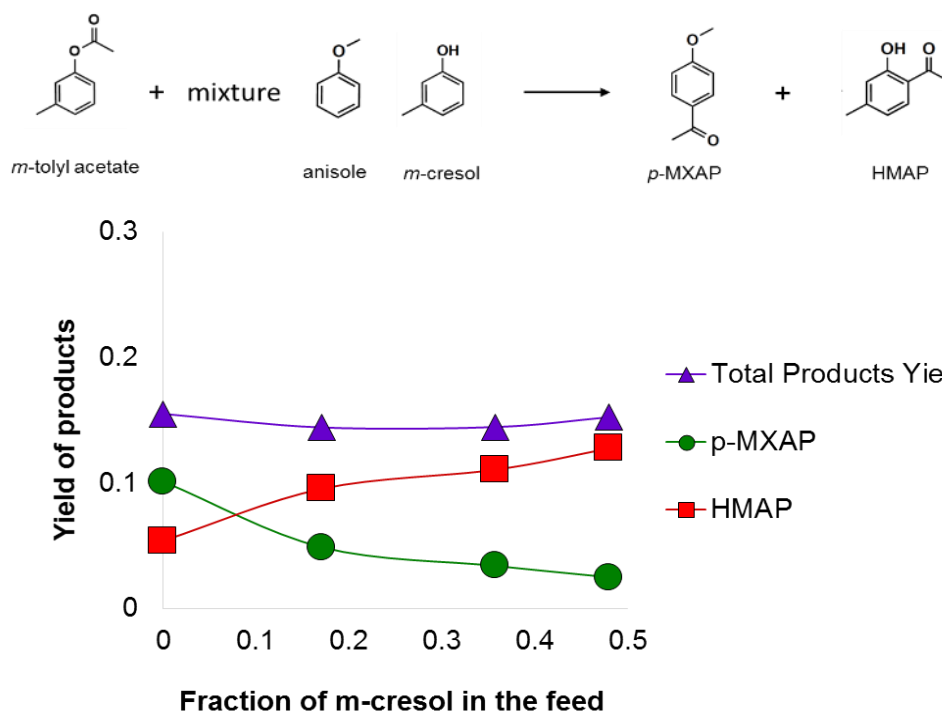
Figure 9. Product distribution vs. fraction of m-cresol in the feed. Reaction conditions: 1M m-tolyl acetate feed with mixture of m-cresol and anisole at different fraction of m-cresol, 0.1g H-Beta with 80ml solution, 1hr 250℃

In **Figures 8** and **9,** it is seen that the total yield of acetophenones is approximately constant at 22% and 15%, respectively, with varying phenol/anisole and *m*-cresol/anisole ratios ranging from 0-1. This remarkable result indicates that the total acylation yield does not depend on the composition of the aromatic substrate mixture, but only on the nature of the aromatic ester (acylating agent). The total carbon balance was always higher than 90% in all cases. Furthermore, as the fraction of phenol or *m*-cresol in the feed increases, the selectivity toward their corresponding acylation products also increases.

One additional reaction that may complicate the analysis of the products in this case is the Fries rearrangement, which is the isomerization of an aromatic ester to a

23

hydroxyaryl ketone. To compare the acylation products of phenol, anisole and *m*-cresol, it is needed to differentiate the acylated products arising from the direct acylation of the aromatic substrates in the initial feed from those resulting from the aromatic esters via Fries rearrangement. Since the methoxy group in anisole is stable under reaction conditions, and the only acylation product arising from anisole is *p*-MXAP, it can be concluded that all the hydroxyaryl ketones obtained when using only anisole as the substrate arise from Fries rearrangement. Furthermore, the yield of Fries rearrangement products only depends on the nature and initial concentration of the aromatic esters, and not on the composition of the aromatic substrates feed, therefore, we can safely subtract them from the product distribution in the same amounts observed when feeding only anisole. In **Figs 8 and 9**, the initial concentration of esters is kept constant at 1M, the concentrations of Fries rearrangement products are 0.02M *o*-HAP and 0.012M *p*-HAP for phenyl acetate, and 0.05M HMAP for *m*-tolyl acetate (as observed when the fraction of phenol and *m*-cresol is 0). Then, the acylated products of the aromatic feed are calculated by subtracting these amounts from the total acetophenone products. While these amounts are smaller than the acylated products, it is important to conduct this correction to obtain a precise analysis for the discussion below.

   Accordingly, **Figure 10** has been constructed from **Figs. 8 and 9**. In this figure, it shows the fraction of acylated anisole (*p*-MXAP) in the corrected acylated products *vs.* the fraction of anisole in the feed. The solid line with a slope of 1 would represent equal acylation selectivity for anisole in comparison with *m*-cresol or phenol. Yields observed above this line would indicate that anisole is more selective than either phenol or *m*-

cresol, since a small increase in the anisole fraction in the feed leads to a great increase in the fraction of acylated anisole in the products. By contrast, the yield observed below that line mean that anisole is less selective than either phenol or cresol. **Figure 10** shows that indeed, this is the case, anisole is less selective than both *m*-cresol and phenol. That is, the selectivity of the aromatic substrates decreases in the order of *m*-cresol > phenol > anisole. It shows that the hydroxyl –OH and methoxy $–OCH_3$ substituents can activate the aromatic ring, and the presence of a methyl group $–CH_3$ at the *meta* position may further enhance the selectivity of the aromatic substrate. However, the methyl group alone is not effective enough to activate the aromatic ring for efficient C-C coupling activity, as proven in the case of toluene.
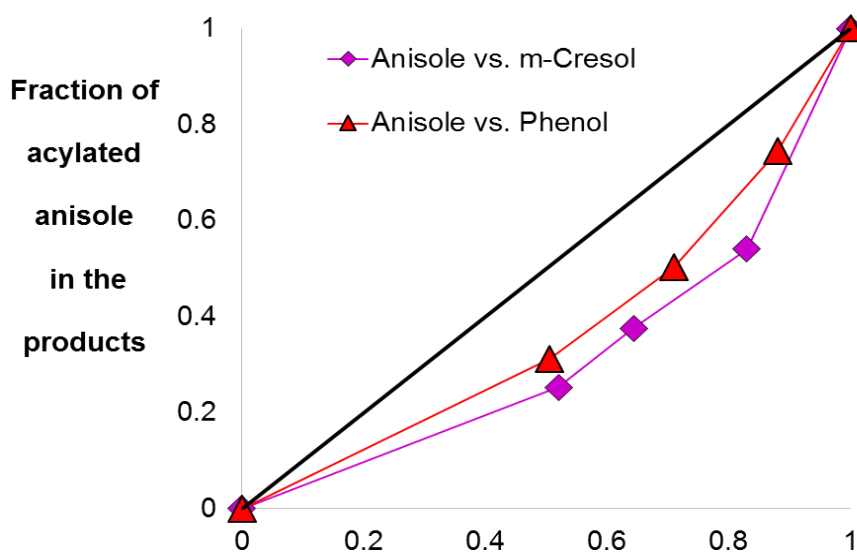
Figure 10. Fraction of acylated anisole (p-MXAP) in the acylated products from aromatic substrate feed vs. fraction of anisole in the aromatic substrate feed, based on figure 8 and 9

3. *Inter and intra molecular rearrangement of phenyl acetate*

Fries rearrangement of aromatic esters, particularly phenyl acetate, has been reported and investigated extensively in the literature[23, 45-46]. In the case of phenyl acetate, both *o-*

25

and *p*-HAP are products of this Fries rearrangement reaction. It could proceed via either inter or the intramolecular mechanism. In the intramolecular mechanism, the ester rearranges itself into *o*-HAP. While in the intermolecular mechanism, the ester decomposes into phenol and acylium ion, and the phenol molecule couples with acylium ion to form both *o*- and *p*-HAP.

As mentioned above, the amount of HAPs obtained when phenyl acetate is fed with pure anisole corresponds to Fries rearrangement products of phenyl acetate. If this Fries rearrangement reaction had happened via an intermolecular mechanism exclusively, when phenol is introduced into the aromatic substrate feed, the ratio between *o*- and *p*-HAP would have been constant. In the intermolecular mechanism, phenyl acetate decomposes to acetyl ion and phenol. This phenol should behave analogously to the phenol molecule present as the aromatic substrate feed, which in turns has the same preference to pick up an acylium ion at an *o*- or a *p*- position, resulting in a constant ratio of *o*- to *p*- products. In **Figure 11,** the ratio of *o*-HAP to *p*-HAP has been plotted *vs.* the fraction of phenol in the feed when phenyl acetate was fed with different mixtures of anisole and phenol. It is observed that the *o*- to *p*- ratio first decreases and then reaches a plateau at increasing fraction of phenol in the feed. This trend indicates that the Fries rearrangement of phenyl acetate does not only occur intermolecularly only, but also intramolecularly. When fraction of phenol in the feed is zero, the total yield of HAPs is small and the intramolecular *o*-HAP product dominates, making a high *o*- to *p*- ratio. As the fraction of phenol in the feed increases, phenol couples with the acylium ion to form HAPs. Thus, the fraction of intramolecular *o*-HAP products starts decreasing and the *o*-

to *p-* ratio approaches the value that represents the reference of a phenol molecule to pick

up the acylium ion at *o-* and *p-* positions.
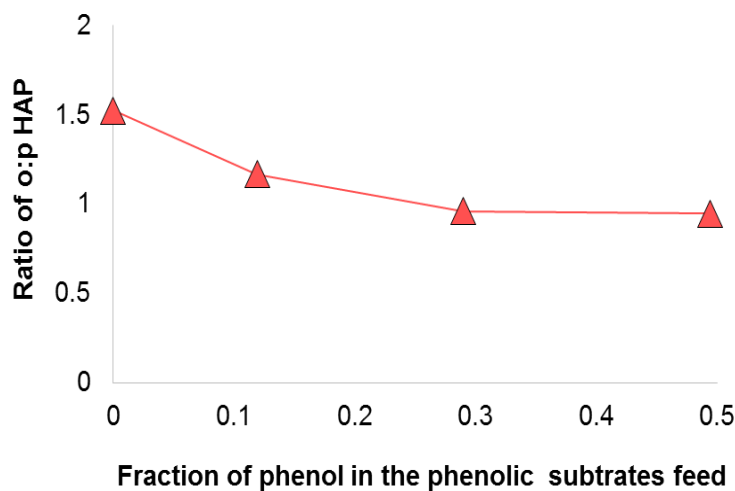
Figure 11. Ratio of o: p HAP product vs. fraction of phenol in the feed of phenol and anisole Reaction conditions: 1M phenyl acetate in mixture of phenol and anisole, 0.1g H-Beta with 80ml feed, 1hr 250°C
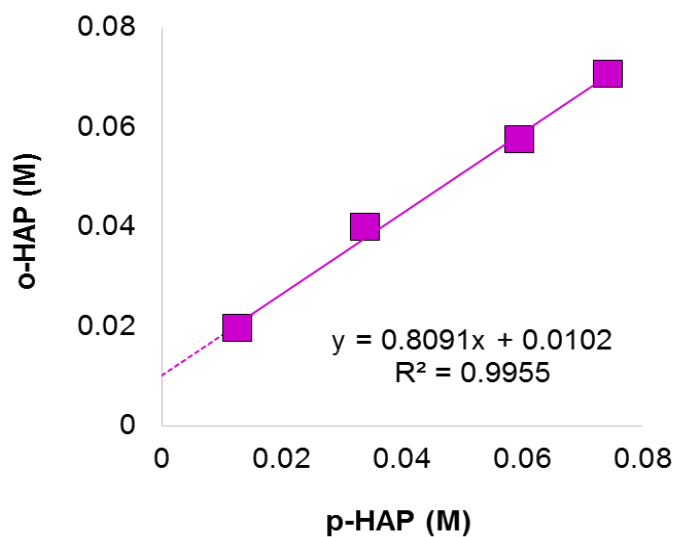
Figure 12. Concentration of o-HAP vs. p- HAP product. Reaction conditions: 1M phenyl acetate in mixture of phenol and anisole, 0.1g H-Beta with 80ml feed, 1hr 250°C

To quantify the fraction of products obtained via the intramolecular mechanism, the *o*-HAP was plotted *vs. p*-HAP, as shown in **Figure 12**. A linear relationship between *o*- and *p*-HAP is clearly apparent. The intercept of this line is the concentration of intramolecular *o*-HAP product, which is 0.01M, and the slope means that when a phenol molecule couples with acetyl ion, the chance of forming *o-* or *p-* isomer is 0.8. The total Fries rearrangement product yield of phenyl acetate is 0.032M and the intramolecular product yield is 0.01M. Therefore, the amount of intermolecular HAPs is 0.032M minus 0.01M, which is 0.022M.

Based on these results, we can calculate the selectivity of intra *vs.* inter-molecular Fries rearrangement products, as reported in **Table 5.**

Table 5. Selectivity of intra vs. inter-molecular mechanism for Fries rearrangement of phenyl acetate

	Intramolecular Mechanism	**Intermolecular mechanism**
Selectivity	30% *o*-HAP only	70% *o*-HAP : *p*-HAP=0.8

In previous studies, intramolecular pathway was identified as the main contributor to the production of *o*-HAP from phenyl acetate. Simultaneously, in the Fries rearrangement, *o*-HAP is the primary product while *p*-HAP is secondary.[47] However, this study has shown that while the intramolecular pathway does occur, the intermolecular one is dominant. Additionally, while the intramolecular *o*-HAP product is primary, the intermolecular *o-* and *p*-HAP products are clearly secondary.

4. DFT calculations of the acylium ion formation

Regarding the nature of the acylating agent, experimental results have shown that acetic acid and methyl acetate have low acylation activity, while *m*-tolyl acetate is effective. To further investigate the meaning of these results, DFT calculations were conducted to calculate the energy barriers for the formation of acetyl ions from these three different acylating agents: acetic acid, methyl acetate and *m*-tolyl acetate, as shown in **Figure 13**.
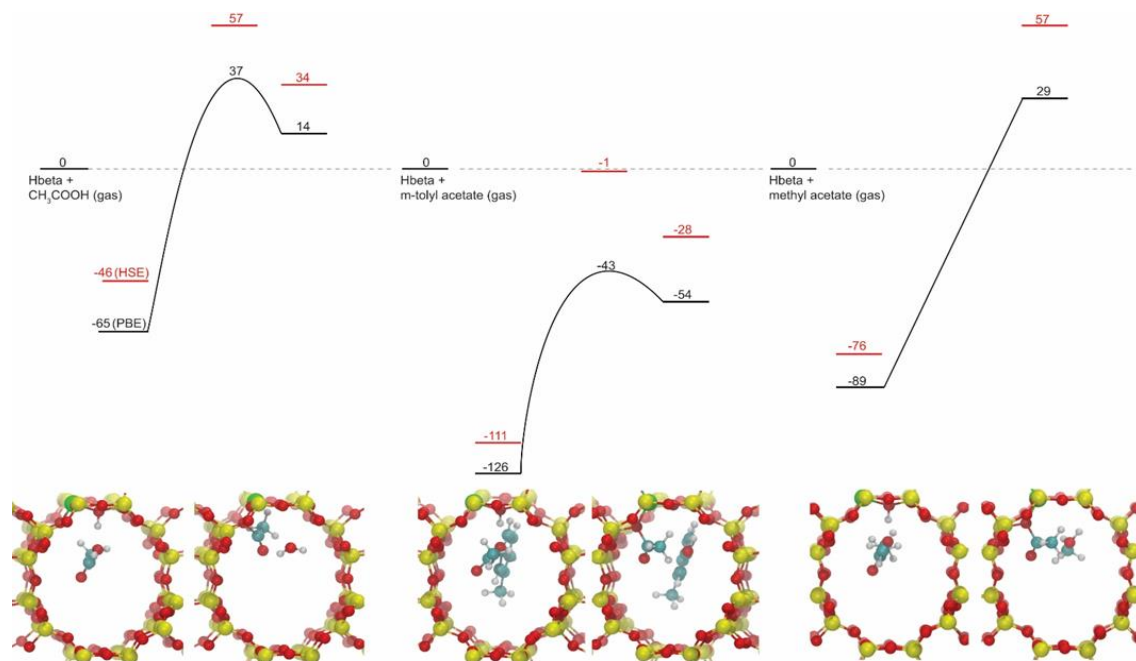
Figure 13. DFT calculation for the acetyl ion formation for acetic acid (left), m-tolyl acetate (middle) and methyl acetate (right) in HBeta. The initial and final structures are shown at the bottom. The values calculated using the PBE and HSE functionals are shown in black and red, respectively.

From the results in **Table 6**, the lowest intrinsic activation energy for acetyl ion formation is from *m*-tolyl acetate (83 kJ/mol), followed by acetic acid (102 kJ/mol) and finally methyl acetate (118 kJ/mol). Furthermore, due to the strong adsorption of *m*-tolyl acetate, the apparent activation energy required for the formation of acetyl ion of *m*-tolyl

acetate is significantly lower, compared to the other two acylating agents. Interaction between the bulky aromatic moiety and the zeolite framework stabilizes both the initial adsorption of the acetate and the formed acetyl ion. For both acetic acid and methyl acetate, the apparent activation barrier is about 30 kJ/mol in the DFT-PBE calculations and about 60 kJ/mol in the DFT hybrid calculations. In the latter case, the calculation of the activation barrier is improved by using the HSE hybrid functional to reduce the delocalization error[48] (see methods). In the case of methyl acetate, the reverse reaction to form methyl acetate from acetyl ion and methanol is barrier-less, indicating that this reverse reaction would be easy. These DFT results suggest that *m*-tolyl acetate will be the most active acylating agent, in good agreement with the experimental results.

Table 6. Heat of adsorption and true activation energy of different acylating agents

	$\Delta H_{adsorption}$ (kJ/mol)	$\Delta H_{true\ activation}$ (kJ/mol)
Acetic acid	-65	102
Methyl acetate	-89	118
***m*-Tolyl acetate**	-126	83

5. *Rate-limiting step*

From the discussion in the previous sections, it has been demonstrated that the acylation reaction occurs in tw*o*-steps, (1) formation of acylium ion and (2) C-C bond formation between aromatic substrate and acylium ion. What is not clear from this analysis is whether one of the two steps can be considered rate-limiting. In fact, as observed in **Table 3**, the nature of the acylating agent used has a significant impact on the reaction yield. When the aromatic substrate is *m*-cresol or anisole, aromatic esters are proved to be effective acylating agents, while acetic acid and methyl acetate are not.

Therefore, one could argue that step (1), which is the formation of the acylium ion, is the rate-limiting step. However, when the same aromatic ester was used as the acylating agent the nature of the aromatic substrate also affected greatly the observed yield. That is, with phenyl acetate as acylating agent anisole gave a much higher acylation yield than toluene, as seen in **Table 4**. It can be concluded that, in the C-C bond formation with the acylium ion, aromatic substrates that have oxygen-contained functional substituents (e.g., phenol, anisole, *m*-cresol) are effective while alkylated aromatic substrates such as toluene are not. Therefore, one could argue that, in the last case, step (2) is the rate-limiting step. This is in agreement with recent reports investigating the mechanism of C-C bond formation over methylfuran, in which the ability of the aromatic compound to stabilize the positive charge of the acylium ion was found to lower the activation barrier for C-C coupling to the point where it was no longer rate-controlling.[26] Based on these observations, it can be concluded that in this reaction there is not a definite rate-limiting step, but it depends on the relative energy barriers for steps (1) and (2). When a less effective acylating agent, such as acetic acid or methyl acetate is used, the rate-limiting step is the formation of acylium ion (1). However, when an effective acylating agent (e.g. aromatic ester) and a poor aromatic substrate (e.g. toluene) are used, the rate-limiting step becomes the C-C bond formation (2). Therefore, a high acylation yield is only obtained when both the acylating agent and aromatic substrate are effective. Interestingly, when an aromatic ester is used as the acylating agent with aromatic substrates that have oxygen-contained functional substituents such as phenol, anisole and *m*-cresol, step (1) formation of acylium ion is the rate-limiting step and the total acylation yield depends on the type of

31

aromatic ester, as seen in section 2.2. Phenyl acetate has a higher acylation yield than *m*-tolyl acetate, suggesting that the nature of the exiting group is important for the formation of acylium ion. Phenyl is less bulky than tolyl group and maybe easier to leave, therefore the acylation yield of phenyl acetate is higher compared with *m*-tolyl acetate.

Conclusions

In this study, liquid phase acylation over zeolite Beta has been investigated and proven to occur via a tw*o*-step mechanism, (1) formation of acylium ion followed by (2) C-C bond formation between aromatic substrate and acylium ion. Experimental results and DFT calculations have shown that aromatic esters are effective in generating acylium ions while acetic acid and alkyl acetate such as methyl acetate are not. However, if acetic acid or methyl acetate is fed with aromatic substrates that contain -OH substituent, they can undergo fast esterification or transesterification to create aromatic esters, which are more active acylating agents, resulting in high yield of the acylation products. This finding has important consequences for bi*o*-oil upgrading since acylation could become an effective way to enhance the utilization of acetic acid without loss of carbon, as would occur with the alternative C-C bond forming ketonization. One could pretreat the lignin-derived aromatic streams to convert the abundant alkoxy substituent compounds (Ar-OR) to phenolic derivatives (Ar-OH). This pretreatment can easily be done via transalkylation by feeding the mixture over zeolite to convert the alkoxy –OR to hydroxyl –OH and alkyl –R functional groups.[49] Therefore, even though acetic acid is not a good acylating agent, it can undergo esterification with these phenolic compounds (Ar-OH) to produce aromatic esters, and further creates the desired acetophenones, versatile molecules that can be

directly hydrotreated[50] to drop-in fuels or further upgraded to longer chain molecules via different chemistries such as aldol condensation due to the ketone functionality.[16, 51]

Furthermore, in this reaction, once the acylium ions are generated, the aromatic compounds with oxygen-containing functionalities, such as hydroxyl –OH and alkoxy –OCH$_3$, are all active to pick them up with the activity of this C-C coupling step decreasing in the order of *m*-cresol > phenol > anisole. Alkyl aromatic compounds such as toluene are not as effective for picking up the acylium ions, which leads to a low acylation yield and high loss of acylium ion to coke. The presence of oxygen-contained functional groups in the lignin derived aromatic compounds was not considered favorable due to the requirement for intensive hydrotreating step. However, as shown in this study, these functional groups have the advantage of activating the aromatic ring and make them easier in the upgrading process, particularly for C-C bond formation reactions. It is thus very important to perform C-C coupling reaction via acylation with the available functionalities in bi*o*-oil before the hydrotreating process.

In the last part of the study, the Fries rearrangement of phenyl acetate to HAPs was investigated to differentiate between the intermolecular and intramolecular reaction pathway. The reaction was found to happen via both mechanisms, in which the intermolecular one is more dominant.

Experimental and DFT Details

Experimental

Three H-form zeolites were used as catalysts. Two of them (Beta CP814C, and ZS*M*-5 CBV-5524G) were received in the NH$_4$-form and then converted to the H-form by

calcining under air at 600°C for 5 hours, after a linear heating ramp of 2°C/min. The third sample was an HY zeolite (CBV 760) received in the H-form from the manufacturer (Zeolyst International).

The reactions were carried out in the liquid phase using a 160-mL batch stainless steel autoclave reactor (Parr Corporation). The reactor is equipped with a stirring impeller, temperature controller, pressure gauge, and sampling port. The reactions were tested over a wide range of temperatures, under N$_2$. The initial pressure of N$_2$ was kept constant at 500 psi, the total volume of reactants was 80 ml and the stirring speed 500 rpm. In a typical reaction run, a measured amount of zeolite was mixed with the reactant mixture in the reactor vessel. After the reactor was sealed and pressurized with N$_2$, the temperature was increased to the desired value. After reaction, the reactor was rapidly cooled down to room temperature and the liquid product was filtered and analyzed on a GC-MS (Shimadzu) for identification and GC-FID (Agilent HP 5890) for quantification.

DFT calculations

Density functional theory calculations were performed using the VASP package[52] to investigate the reaction mechanism. The PBE (Perdew-Burke-Ernzerhof) exchange-correlation potential[53] was used, and the electron-core interactions were treated in the projector augmented wave (PAW) method.[54-55] The van der Waals interactions have been taken into account through the s*o*-called DFT-D3 semi-empirical method via a pair-wise force field.[56-57] The calculations have been performed using an H-beta unit cell that includes 64 Si and 128 O atoms. One Si atom was replaced by one Al atom, so the Si/Al

ratio was 63/1. The structure of the unit cell was taken from an experimental work (a = 17.829 Å, b = 17.829 Å, c = 14.671 Å)[58] and fixed during the calculation. All the atoms were relaxed until the atomic forces were smaller than 0.02 eV Å^{-1}, using a single Γ point of the Brillouin zone with a kinetic cut off energy of 400 eV. The nudged elastic band (NEB)[59] method has been used to find the transition state and calculate reaction barriers. The transition states have been further verified by vibrational calculations. An HSE (Heyd-Scuseria-Ernzerhof) hybrid functional[60-61] was used to calculate the total energy of the initial, transition, and final states that had already been optimized by DFT-D3 calculations to reduce the underestimation of the reaction barriers caused by the charge delocalization error of the local and semi-local exchange-correlation functionals.[48]

II.   Negative Effect of Temperature on Hydrogenation Reactions and Weak Adsorption of m-Cresol on Pt Surface

Motivations and Literature Reviews

As mentioned in the introduction, understanding about hydrogenation reaction of phenolic molecules on metal catalysts will help us understand better about the interaction of the phenolic molecules with metal surfaces over a wide range of temperatures. Based on this knowledge, the reaction conditions can be tuned toward the desirable products. There have been extensive studies on HDO[1, 62-63] but the HY reaction mechanism remains elusive, therefore, this work will concentrate on HY of phenolic molecules. In this study, m-cresol is chosen as the model compound to represent the phenolic molecules with hydroxy group (-OH) functionality. The hydrogenation of m-cresol is investigated on Pt catalyst, as Pt is known as a good hydrogenation catalyst. To focus only on the metal surface and minimize any metal-support interaction, SiO_2 is used as the support.

Previous studies have shown that at temperature of 300℃, Pt/SiO_2 is active for both HY and HDO of m-cresol, but HDO dominates.[1] Wang et al. has investigated the hydrogenation mechanism for o-cresol on Pt(111) with different H coverage and shows that high H coverage surface reduces the energy barrier for hydrogenation steps.[64-65] Study from Talukdar et al. for phenol conversion over Pt and Pd at temperature 200-275 ℃ has shown that the main products are hydrogenation of phenol cyclohexanone and cyclohexanol, while the HDO products to benzene and cyclohexane were insignificant. The hydrogenation conversion was dropping with temperature, and while Pt is more active for total hydrogenation conversion, Pd is more selective toward cyclohexanone

formation.[66] Another report from Liu et al. has also report exclusive selectivity of phenol hydrogenation to cyclohexanone over bifunctional Pd - Lewis acid catalyst.[67]

Similar to results from Talukdar et al., the negative effect of temperature on phenol hydrogenation was also observed by Singh et al., and the reason for this drop was attributed to poisoning of dehydrogenated phenol species at high temperatures.[68] According to the author, the dehydrogenated species are formed from adsorbed phenol on the catalysts surface, and at high temperature, these species are created at higher rate, therefore, they will block the active sites and as a result, the activity drops at high temperatures. This theory of dehydrogenated species presented on the metal surfaces was also proposed by Vannice et al., in which the authors reported the reversible maximum activity of benzene and toluene hydrogenation on different metals such as Pt and Pd.[69-75] According to the author, the dehydrogenated species are formed at higher temperatures, competing for sites with benzene or toluene and as a result, the coverage of benzene and toluene drops at increasing temperature. However, the formation of these dehydrogenated poison species is not kinetically or thermodynamically favored based on DFT calculations. DFT results show that the dehydrogenation of benzene to phenyl on Pt(111) is +76 kJ/mol endothermic, while the first hydrogenation step is only +11 kJ/mol endothermic with energy barrier of 74 kJ/mol.[76] Another study for hydrogenation of toluene on $Pt/A_{12}O_3$ by Castano et al. also observed the negative effect of temperature on toluene conversion and explained it in term of the drop in coverage of toluene at increasing temperature.[77]

Based on these results, the hydrogenation of m-cresol on Pt will be investigated over a wide range of temperature to see the activity of the catalyst, additionally, the hydrogenation products 3-methylcyclohexanone and 3-methylcyclohexanol are also used as feed.

Materials and Methods

Catalyst preparation:

1% wt. Pt/SiO_2 catalyst was prepared by incipient wetness impregnation of SiO_2 (Davisil grade 923) with an aqueous solution of chloroplatinic acid hexahydrate, purchased from Sigma-Aldrich (ACS reagent, ≥37.50% Pt basis). After impregnation, the catalyst was dried overnight at 120℃ followed by heating under air at 400°C for 3 h.

Catalysts characterization by TEM and CO chemisorption:

Metal particle size was determined by both TEM and CO chemisorption, as summarized in **Table 7**. TEM images, as shown in **Figure 14**, were obtained on a JEOL 2000 field emission system operated at 200 kV. The particle size was measured on 230 particles and the particle size distribution is presented in **Fig**.15.

For CO chemisorption, the catalyst was first reduced in a 60 sccm H_2 for 1 hour at 300°C, cooled down and purged in He at room temperature for 30 min. Then the CO uptake is measured by sending pulses of CO until saturation and the ratio of CO/Pt was calculated.[78]

Table 7. Particle size and dispersion based on TEM and CO chemisorption

	TEM	**CO Chemisorption**
d_P (nm)	2.3	1.4
Dispersion	50%	80%
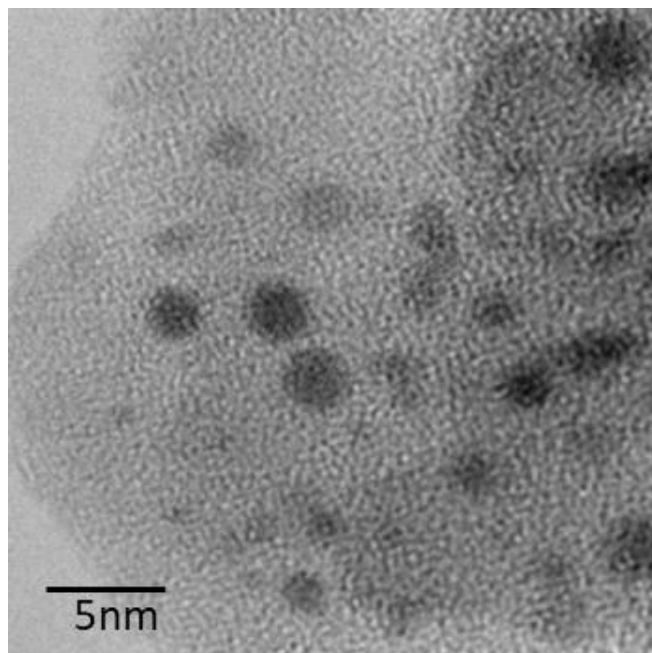
Figure 14. HR-TEM of Pt/SiO2
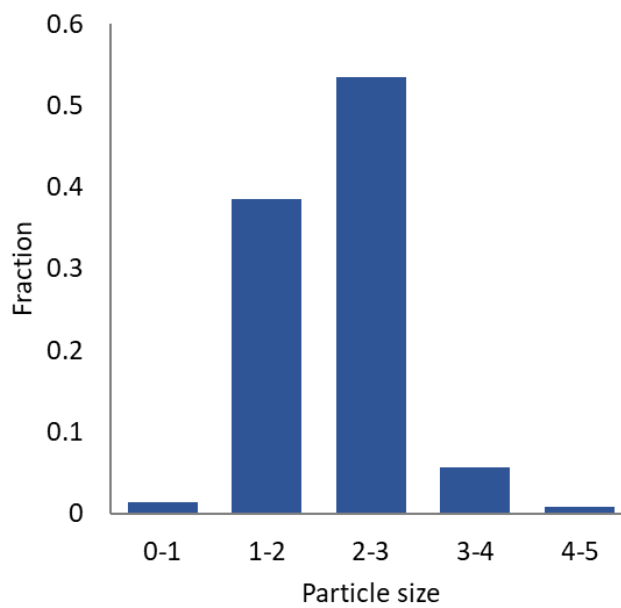
Figure 15. Particle size distribution of Pt/SiO2

Catalytic Measurements:

The experiments were executed in vapor phase with a plug flow reactor at atmospheric pressure. In a typical experiment, the catalyst (250-350 μm pellet) was packed in a 200cm stainless steel vertical tube reactor and pre-reduced in-situ under continuous flow of 60 sccm H_2 at 300°C for 1 h. Subsequently, the temperature was lowered to the reaction temperature, keeping the catalyst bed under H_2 flow during the entire time of the experiment. The liquid feed is continuously injected via a syringe pump and vaporized into H_2 stream. The H_2/feed molar ratio was kept more than 40:1 to minimize deactivation. The products were analyzed online by GC (Agilent HP 5890) using an HP-Innowax capillary column equipped with a FID detector.

Result and Discussion

1. *Non-linear Arrehnius Profile of m-Cresol conversion on Pt/SiO2*

The conversion of m-cresol was tested at different temperatures in the range of 140-300°C, the conversion of m-cresol was plotted on an Arrhenius plot with temperature as shown in **Figure 16**.
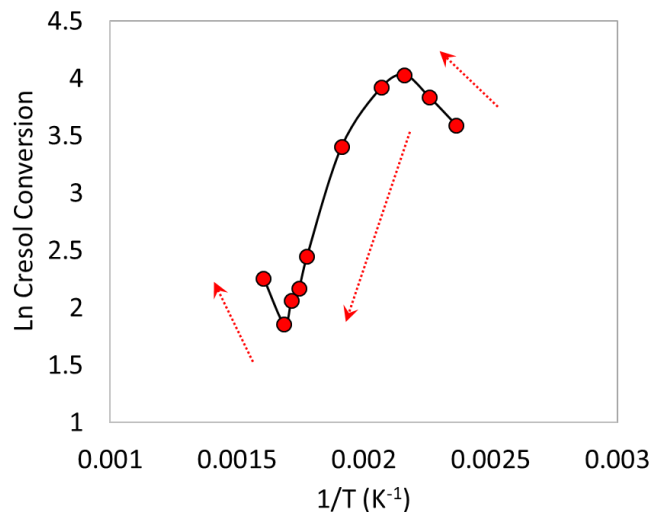
Figure 16. Arrhenius plot of ln(cresol conversion) vs. 1/T

The products distribution as functions of W/F are shown in **Figure 17** for 150, 190 and 250 ℃. At the temperature range from 140 to 250℃, the main products are hydrogenation products, 3-methylcyclohexanone (ONE) and 3-methylcyclohexanol (OL), while the hydrodeoxygenation product, toluene (TOL), remains insignificant (≤ 3% selectivity). When temperature increases from 270 to 300℃, toluene starts to increase, while ONE and OL decrease.

At 150 ℃, as shown in **Figure 17a**, 3-methylcyclohexanol (OL) appears to be a secondary product, as the slope of the OL yield curve is 0 at low W/F, suggesting OL is produced from 3-methylcyclohexanone (ONE). However, at higher temperatures, 190 ℃ and 250 ℃ as shown in **Figure 17b-c**, the yield curve of OL does not slope of zero at low W/F, suggesting that it could also be a primary product from m-cresol. Based on these observation, a reaction pathway was proposed as shown in **Figure 18**, which includes hydrogenation/dehydrogenation reactions among m-cresol, ONE and OL. This reaction pathway is aligned with previous study.[1]

41
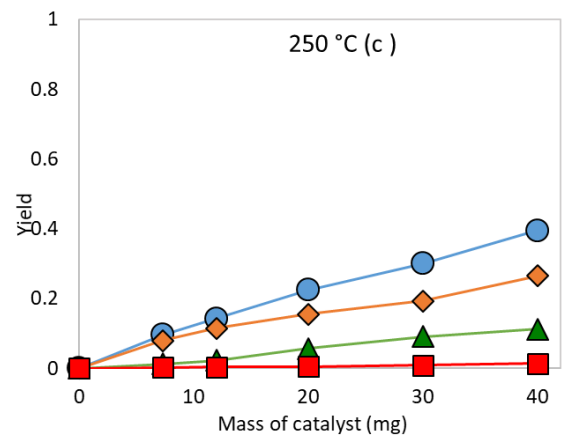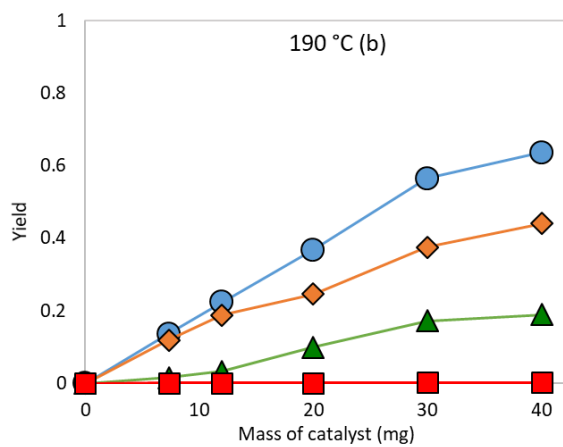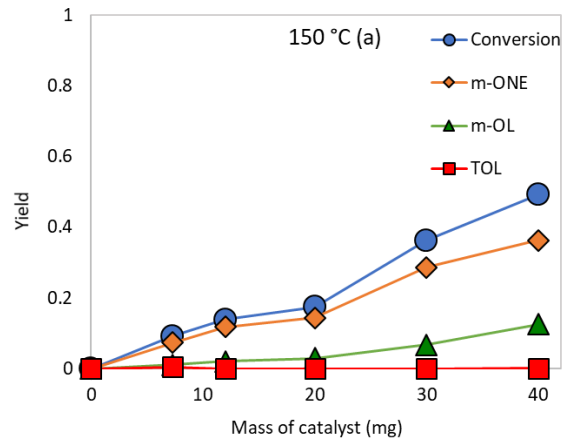
Figure 17. Product distribution as a function of W/F at different temperatures. (a) 150, (b) 190, (c) 250. Reaction conditions: $P_{cresol,feed}$=0.02 atm, 60 sccm H_2
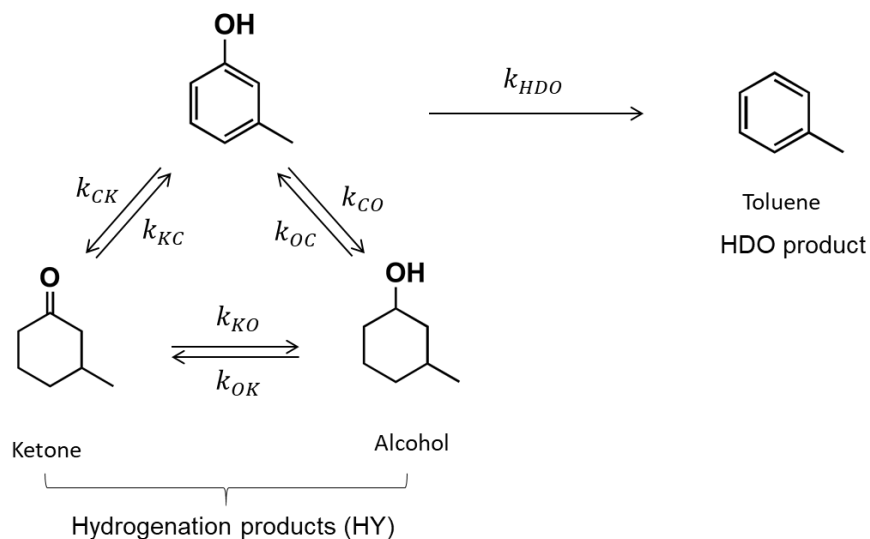
Figure 18. Reaction pathway for conversion of m-cresol

The yield of hydrogenation products was plotted as functions of temperatures as shown in **Figure 19**. When mass of catalyst increases from 7 to 80 mg, the yield of ONE and OL increase, suggesting that the reaction is not under equilibrium limitation, otherwise the yield would not change with increasing amount of catalyst. Secondly, the yield of ONE and OL increase as temperature increases from 150 ℃ to 190 ℃, then drop at temperature higher than 190 ℃. The maximum yield happens at the same temperature (~190 ℃) for changing amount of catalyst from 7-40mg, which is far below the temperature where HDO (to toluene) starts to become significant (270 ℃).
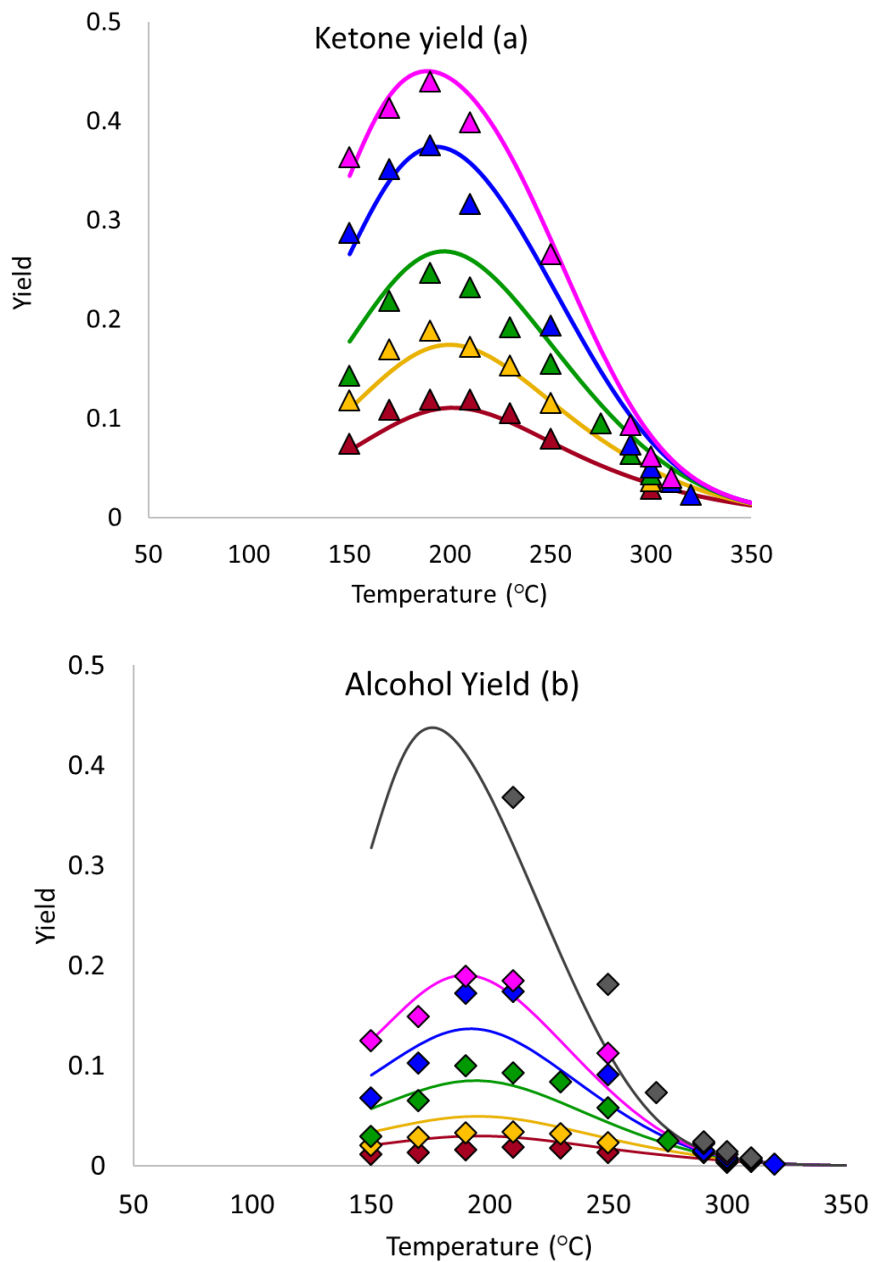
Figure 19. Yield of 3-methylcyclohexanone (a), 3-methylcyclohexanol (b) and total hydrogenation (c) as functions of temperatures at different amount of Pt/SiO2. Reaction conditions: $P_{cresol\ feed}$=0.02 atm, P_{H2}=1 atm. Symbol: Experimental data. Line: Kinetic model.
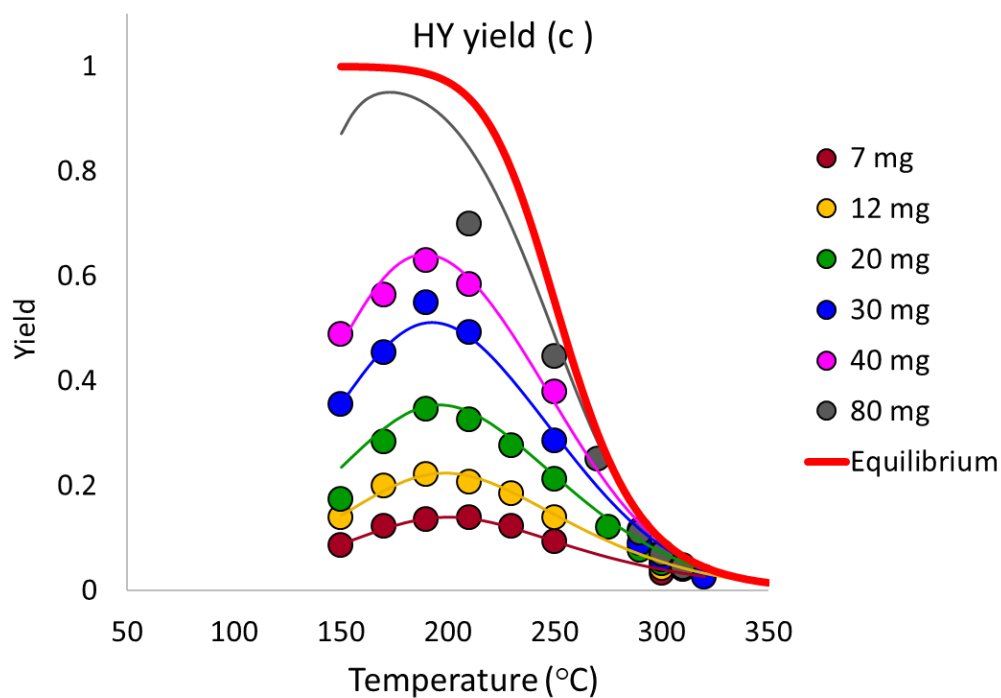
Figure 19. Yield of 3-methylcyclohexanone (a), 3-methylcyclohexanol (b) and total hydrogenation (c) as functions of temperatures at different amount of Pt/SiO2. Reaction conditions: $P_{cresol\ feed}$=0.02 atm, P_{H2}=1 atm. Symbol: Experimental data. Line: Kinetic model.

This negative effect of temperature for hydrogenation reaction has also been observed elsewhere when other aromatic compound such as phenol[68] or benzene[69-70, 72] was used as the feed. This phenomenon could be due to different reasons including (1) site poisoning, (2) equilibrium limitation or (3) change in the surface coverage of m-cresol as T increases. These possibilities will be justified in the following sections to determine which one is the most possible reason for this phenomenon in this case.

45
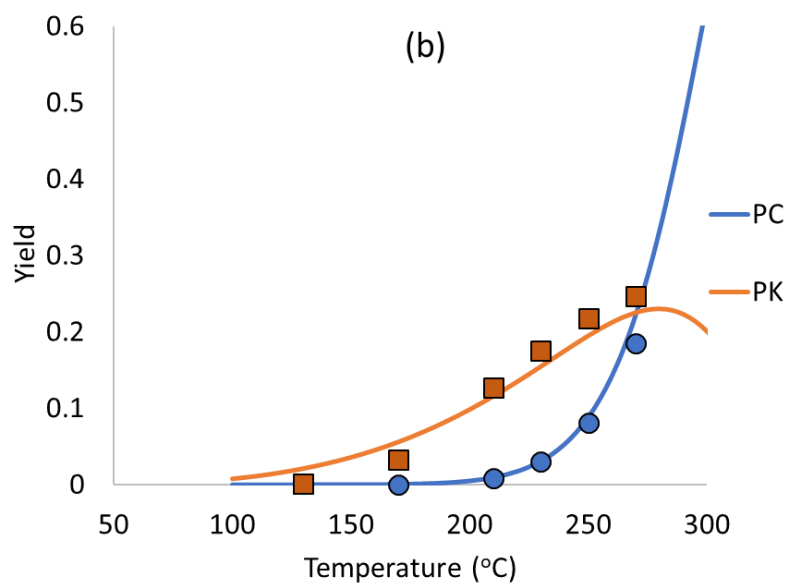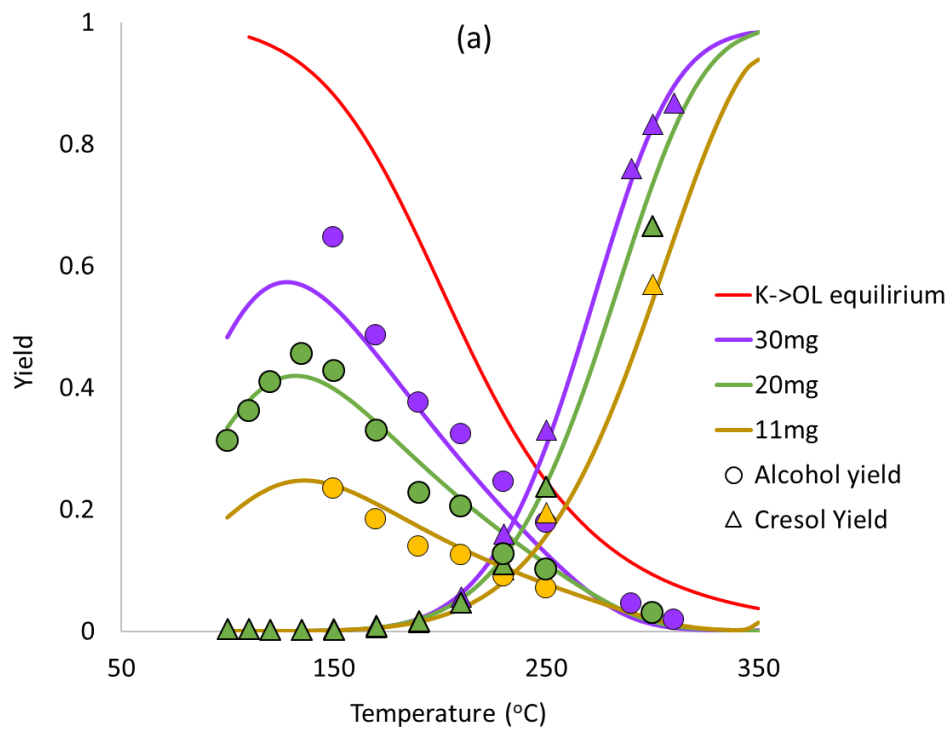
Figure 20. Yield of hydrogenation/dehydrogenation products with (a) 3-methylcyclohexanone feed and (b) 3-methylcyclohexanol feed at different amount of Pt/SiO2.
Reaction conditions: P_{feed}=0.02 atm, P_{H2}=1 atm. Symbol: Experimental data. Line: Kinetic model.

1.1. Site poisoning

As mentioned above, the negative effect of temperature for hydrogenation reaction was also observed for phenol[68], in which the reason was attributed to the poisoning by dehydrogenated phenol species. At high temperature, these species are created at a higher rate, leading to more poisoning and as a result, the yield drops. Also due to this effect, the reaction rate will strongly depend on hydrogen pressure, because hydrogen is crucial to remove these poisoning species.

If this is also true for this case, when we test at low temperature, then increase temperature and go back to the initial low temperature, the activity of the catalyst will significantly drop. Because once the dehydrogenated species are created at high temperature, they will remain adsorbed on the catalyst surface, blocked the active sites and the yield will significantly drop when temperature goes back to lower value. We have also reduced hydrogen pressure to 0.75 atm for this experiment to maximize the poisoning effect so that we can observe it clearly. The results for this experiment was illustrated in **Figure 21**.

It clearly shows that after increasing temperatures from 150 to 170, 190, 210, 230, 250 ℃ and then goes back to 150 ℃, the yield at 150 ℃ does not change, the difference is within experimental error, even at reduced pressure of H_2. Therefore, the site poisoning by dehydrogenated m-cresol species is concluded to be insignificant in this case.
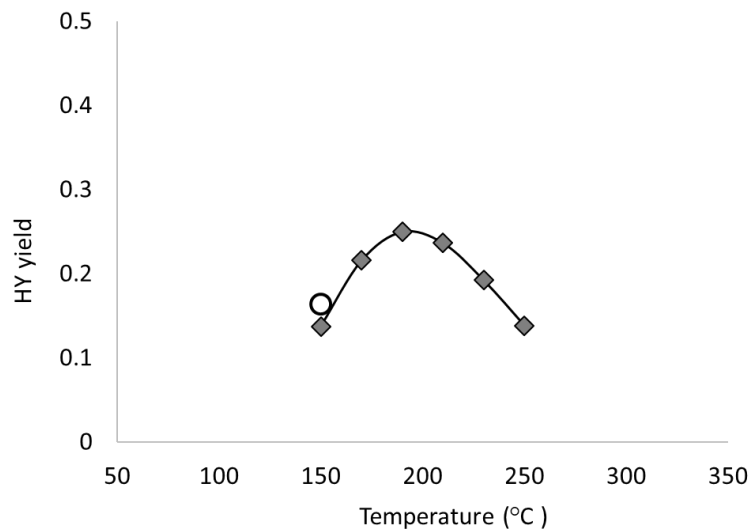
Figure 21. Hydrogenation yield as a function of temperature. Reaction conditions: $P_{cresol\ feed}$=0.02 atm, P_{H2}=0.75 atm, temperature starts from 150 to 170, 190, 210, 230, 250℃ (◆) then goes back to 150℃ (○)

1.2. Equilibrium Limitation

Another possibility is that the decline in yield is due to equilibrium limitation, since hydrogenation is an exothermic reaction, the yield would drop at some point when temperature is high enough. As mention before, as shown in **Figure 19**, the yield keeps increasing as the mass of catalyst increase from 7 to 80 mg catalyst. If the drop is due to equilibrium limitation, we would observe two phenomena, that is the yield after it drops will be the same with different amounts of catalyst, and the maximum temperature where the drop happens will shift to lower values as increasing mass of catalyst, since with higher amount of catalyst, it would reach equilibrium faster. However, as seen from **Figure 19**, the yield after it drops changes with amount of catalyst and the maximum temperature remains the same for different mass from 7-40mg of catalyst. Therefore, the drop in this case is also not due to equilibrium limitation.

The hypothesis can be illustrated with a simple Langmuir-Hinshelwood adsorption model, as following.

$$\theta_C = \frac{K_C \cdot P_C}{1 + K_C \cdot P_C} \text{ and } r = k \cdot \theta_C = \frac{k \cdot K_C \cdot P_C}{1 + K_C \cdot P_C}$$

In which θ_C, K_C, $\cdot P_C$ are coverage, adsorption constant and pressure of m-cresol, and k is the rate constant for hydrogenation reaction.

The adsorption of m-cresol on the Pt surface is exothermic, therefore, at a certain temperature, the coverage of m-cresol will drop significantly, even though the intrinsic hydrogenation rate always increases with temperature, this increase is smaller compared with the decline in cresol coverage, therefore leading to drop in overall rate (illustrated in **Figure 22**).
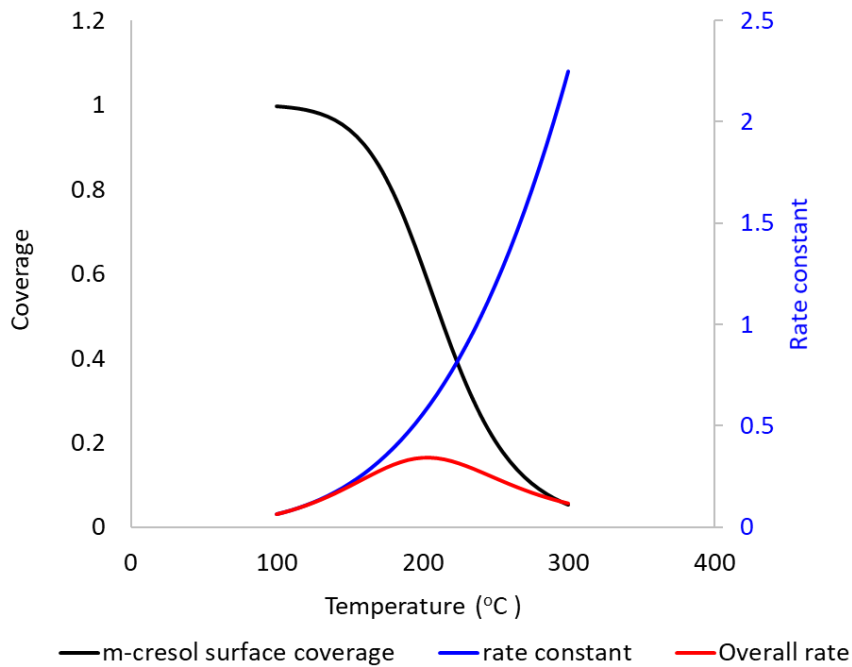
Figure 22. Change if surface coverage, rate constant and overall rate as a function of temperature

49

If this is the case, at the same initial P_C, with increasing mass of catalyst, the temperature where the yield drop will slightly shift to lower values, because P_C decreases with conversion. However, the change is accumulative and will be too small to be observed in current testing temperature increments. On the other hand, the temperature of maximum yield would significantly change with different initial P_C , which is demonstrated in **Figure 23**. It has shown that the curves shift to lower values of temperature as initial P_C drops from 0.03 to 0.005 atm, which agrees with the hypothesis.
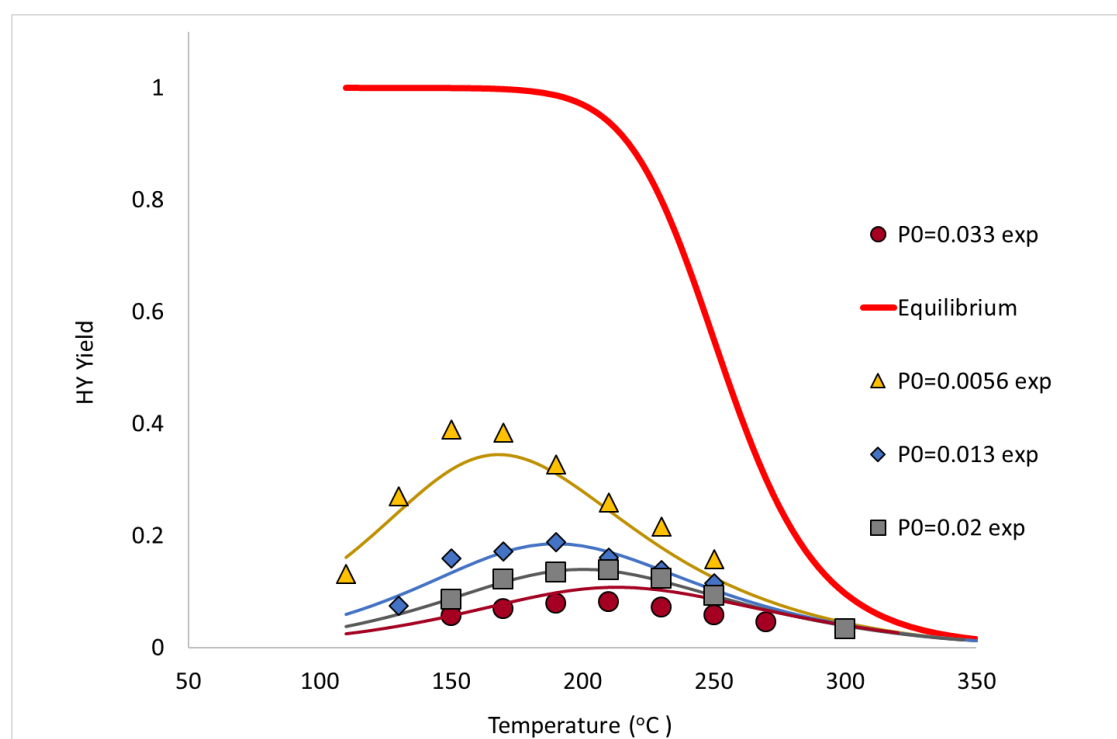
Figure 23. Yield of total hydrogenation products as functions of temperatures at with 7mg of Pt/SiO2. Reaction conditions: $P_{cresol\ feed}$=0.007-0.03 atm, P_{H2}=1 atm. Symbol: Experimental data. Line: Kinetic model.

Moreover, another way to justify this hypothesis is by investigating how the hydrogenation rate depends on m-cresol at different temperatures. At low temperature, when the surface is fully covered, the coverage θ_C reaches maximum of 1 and is independent of m-cresol pressure. The rate becomes $r = k$ and therefore, has zero order

on m-cresol. When the temperature increases, the coverage drops and becomes dependent on m-cresol pressure, the rate now will become $r = k \cdot K_C \cdot P_C$ and the order of dependence on m-cresol will approach 1. As shown in **Figure 24 a-b**, the rate of ketone formation has zero order at low temperatures of 140 and 150℃, then the order increases as temperature increases, to 0.6 ± 0.1 at 250 ℃. The experimental data fit well with the proposed simple Langmuir-Hinshelwood kinetic model, supporting the hypothesis that the yield drop is due to the change in surface coverage.
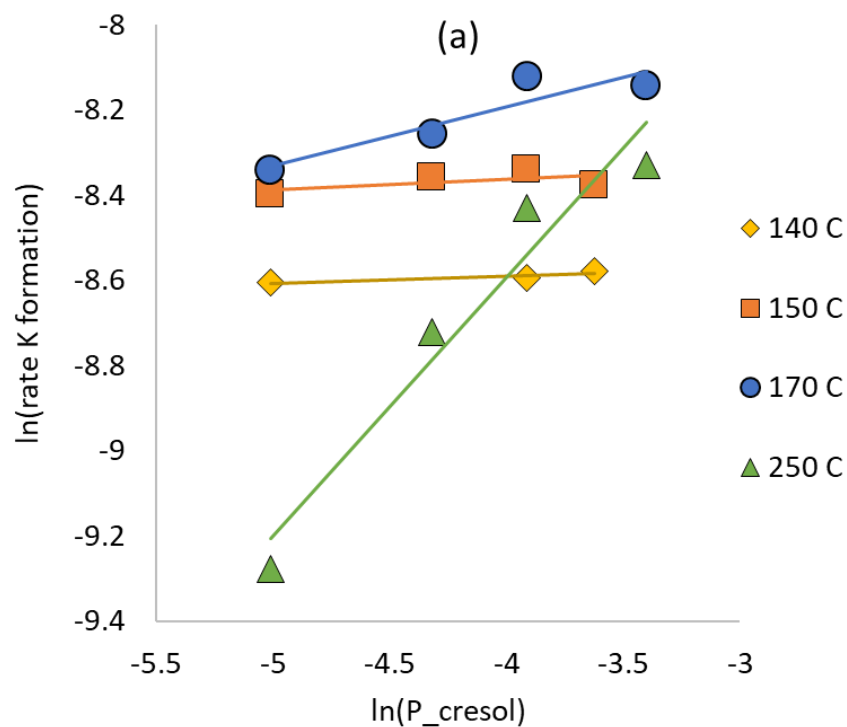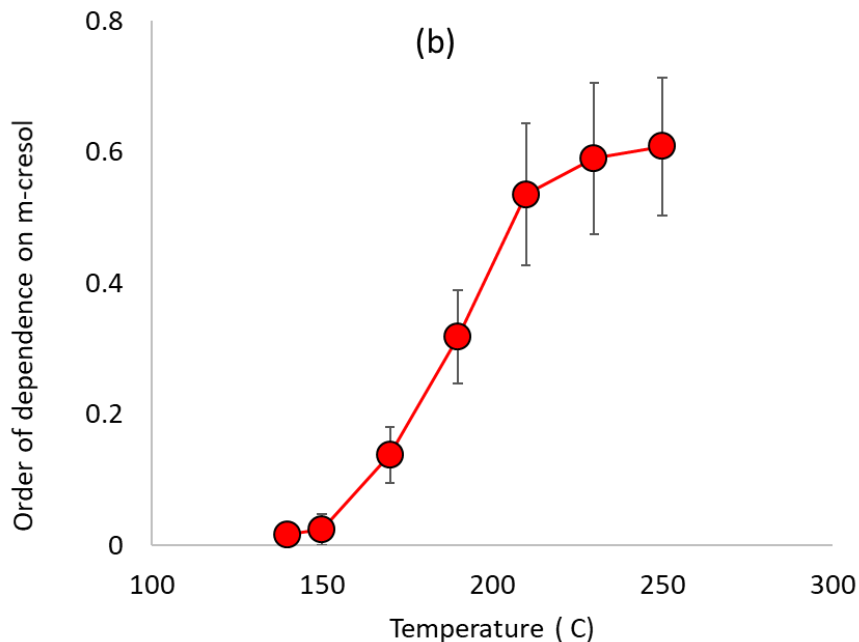
Figure 24. (a) ln of rate of ketone formation as a function of ln of initial cresol partial pressure. The slope of the curve is the order of dependence of the rate on m-cresol pressure. (b) Dependence of 3-methylcyclohexanone formation on cresol pressure at different temperatures

2. Kinetic Modeling

The experimental data suggests that the negative effect of temperature is due to the decline in surface coverage of m-cresol and agrees with the simple Langmuir-Hinshelwood kinetic model. Furthermore, all reactions in **Figure 19, 20 and 23** are executed at constant H_2 pressure of 1atm. Therefore, we have decided to use this simple Langmuir-Hinshelwood kinetic model for all reactions in accordance with the reaction pathway proposed in **Figure 3**.

$$r_{CK} = \frac{k_{CK} K_C P_C}{1 + K_C P_C + K_K P_K + K_O P_O}$$

$$r_{CO} = \frac{k_{CO} K_C P_C}{1 + K_C P_C + K_K P_K + K_O P_O}$$

52

$$r_{KC} = \frac{k_{KC}K_K P_K}{1 + K_C P_C + K_K P_K + K_O P_O}$$

$$r_{KO} = \frac{k_{KO}K_K P_K}{1 + K_C P_C + K_K P_K + K_O P_O}$$

$$r_{OC} = \frac{k_{OC}K_O P_O}{1 + K_C P_C + K_K P_K + K_O P_O}$$

$$r_{OK} = \frac{k_{OK}K_O P_O}{1 + K_C P_C + K_K P_K + K_O P_O}$$

$$r_C = -r_{CK} - r_{CO} + r_{KC} + r_{OC} = \frac{-(k_{CK} + k_{CO})K_C P_C + k_{KC}K_K P_K + k_{OC}K_O P_O}{1 + K_C P_C + K_K P_K + K_O P_O}$$

$$r_K = -r_{KC} - r_{KO} + r_{CK} + r_{OK} = \frac{-(k_{KC} + k_{KO})K_K P_K + k_{CK}K_C P_C + k_{OK}K_O P_O}{1 + K_C P_C + K_K P_K + K_O P_O}$$

$$r_O = -r_{OC} - r_{OK} + r_{CO} + r_{KO} = \frac{-(k_{OC} + k_{OK})K_O P_O + k_{CO}K_C P_C + k_{KO}K_K P_K}{1 + K_C P_C + K_K P_K + K_O P_O}$$

In which k is rate constant for hydrogenation/dehydrogenation reactions as indicated in

Figure 3.

K_C , K_K , K_O are adsorption constants of m-cresol, 3-methylcyclohexanone and 3-methylcyclohexanol

P_C , P_K , P_O are initial partial pressure of m-cresol, 3-methylcyclohexanone and 3-methylcyclohexanol

These rate constants and adsorption constants depend on temperature according to

Arrhenius equation as following:

$$k = A \cdot \exp\left(-\frac{\Delta H}{RT}\right)$$

$$K = exp\left(-\frac{\Delta G_{ads}}{RT}\right) = exp\left(-\frac{\Delta S_{ads}}{R}\right) exp\left(-\frac{\Delta H_{ads}}{RT}\right)$$

In which A is the pre-exponential factors and ΔH is the energy barrier for the reaction

ΔG_{ads}, ΔS_{ads}, ΔH_{ads} are Gibbs free energy, entropy and enthalpy of adsorption

The constants A, ΔH, ΔG_{ads}, ΔS_{ads}, ΔH_{ads} are assumed to be independent with temperature.

Additionally, the hydrogenation/dehydrogenation reactions are related via thermodynamic equilibrium as following:

$$K_{Eq\ CK} = \frac{k_{CK}K_C}{k_{KC}K_K} = exp\left(-\frac{\Delta G_{Eq\ CK}}{RT}\right) = exp\left(-\frac{\Delta S_{Eq\ CK}}{R}\right) exp\left(-\frac{\Delta H_{Eq\ CK}}{RT}\right)$$

$$K_{Eq\ KO} = \frac{k_{KO}K_K}{k_{OK}K_O} = exp\left(-\frac{\Delta G_{Eq\ KO}}{RT}\right) = exp\left(-\frac{\Delta S_{Eq\ KO}}{R}\right) exp\left(-\frac{\Delta H_{Eq\ KO}}{RT}\right)$$

$$K_{Eq\ CO} = \frac{k_{CO}K_C}{k_{OC}K_O} = exp\left(-\frac{\Delta G_{Eq\ CO}}{RT}\right) = exp\left(-\frac{\Delta S_{Eq\ CO}}{R}\right) exp\left(-\frac{\Delta H_{Eq\ CO}}{RT}\right)$$

$\Delta G_{Eq\ CK}$, $\Delta S_{Eq\ CK}$, $\Delta H_{Eq\ CK}$ are Gibbs free energy, entropy and enthalpy of hydrogenation reaction from C to K

$\Delta G_{Eq\ KO}$, $\Delta S_{Eq\ KO}$, $\Delta H_{Eq\ KO}$ are Gibbs free energy, entropy and enthalpy of hydrogenation reaction from K to O

$\Delta G_{Eq\ CO}$, $\Delta S_{Eq\ CO}$, $\Delta H_{Eq\ CO}$ are Gibbs free energy, entropy and enthalpy of hydrogenation reaction from C to O

Additionally, $\Delta S_{Eq\ CK} + \Delta S_{Eq\ KO} = \Delta S_{Eq\ CO}$ and $\Delta H_{Eq\ CK} + \Delta H_{Eq\ KO} = \Delta H_{Eq\ CO}$

These thermodynamic equilibrium parameters can be estimated independently, based on the Gibbs free energy, entropy and enthalpy of formation of C, K and O. In this work, we will derive these parameters from the fitting and listed in **Table 10**. There are total of

16 independent parameters in this fitting, therefore, to ensure a good and meaningful kinetic fitting, we start with simplified rate expressions at low conversions.

At low conversion, the rate become:

$$r_K = -r_{CK} = \frac{k_{CK} K_C P_C}{1 + K_C P_C}$$

$$r_O = -r_{CO} = \frac{k_{CO} K_C P_C}{1 + K_C P_C}$$

Based on these simplified rates at different temperatures, we can get initial guesses for $A_{CK}, \Delta H_{CK}, A_{CO}, \Delta H_{CO}, \Delta S_{ads,cresol}, \Delta H_{ads,cresol}$. The fitting at high conversion will be developed based on these initial guesses. Furthermore, 3-methylcyclohexanone and 3-methylcyclohexanol are also fed at different temperatures, as shown in **Figure 20**. Based on **Figure 19 and 20**, the symbols are experimental data while the solid lines are kinetic models, it shows that this simple Langmuir-Hinshelwood model fits the data very well and the values for the parameters are presented in **Table 8 and 9**. In the next section, we will discuss about the validity of the parameters and the real physical meaning behind the numbers.

Table 8. Adsorption parameters of m-cresol, 3-methylcyclohexanone and 3-methylcyclohexanol

	Cresol	**Ketone**	**Alcohol**
ΔS_{ads}(**J/mol K**)	-124	-100	-118
ΔH_{ads} (**kJ/mol**)	-76	-54	-52

Table 9. Reaction rate parameters for different reaction pathways

	Pre-exponential factor (10^3/s)	**Energy barrier (kJ/mol)**
C -> K	1.6	32

K -> C	$5.5*10^9$	118
C -> O	0.09	26
O -> C	$1.2*10^{16}$	171
K -> O	3.9	29
O ->K	$8.7*10^7$	86

Table 10. Thermodynamic parameters for hydrogenation reactions

	delta H (kJ/mol)	Delta S (J/mol.K)
C->K	-112	-215
K->O	-57	-119
C->O	-169	-334

3. *Sensitivity Analysis of the Model*

The total of independent parameters in the kinetic model is 16, while the total number of data points are about 200. The R^2 value is calculated to be 0.96 and the parity plot is shown in **Figure 10**. It can be seen that the model for m-cresol hydrogenation fit well over a wide range of temperature from 100 to 300℃.
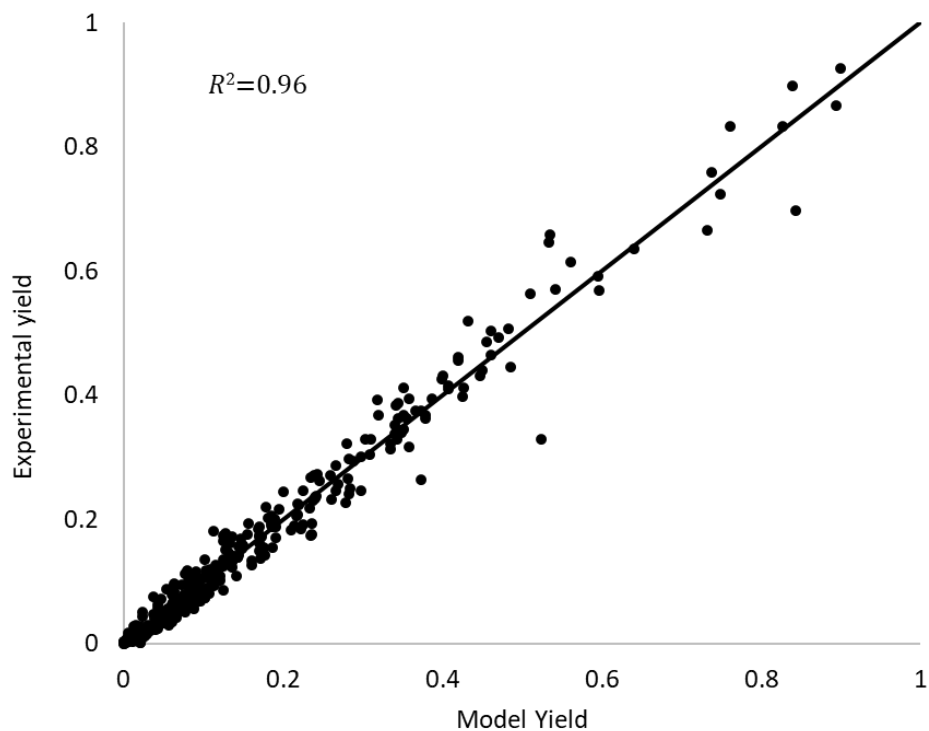
Figure 25. Parity plot

4. *Physical Meanings of the Parameters*

To understand the physical meaning of the obtained kinetic parameters, first we need to determine the rate limiting step for hydrogenation of m-cresol and develop the kinetic models based on that. As seen from **Figure 24 and 26**, the reaction rate depends on m-cresol with order from 0 to 1 as temperature increases, while depends on hydrogen with a higher order, which is about 2 for ketone formation and 3 for alcohol formation.
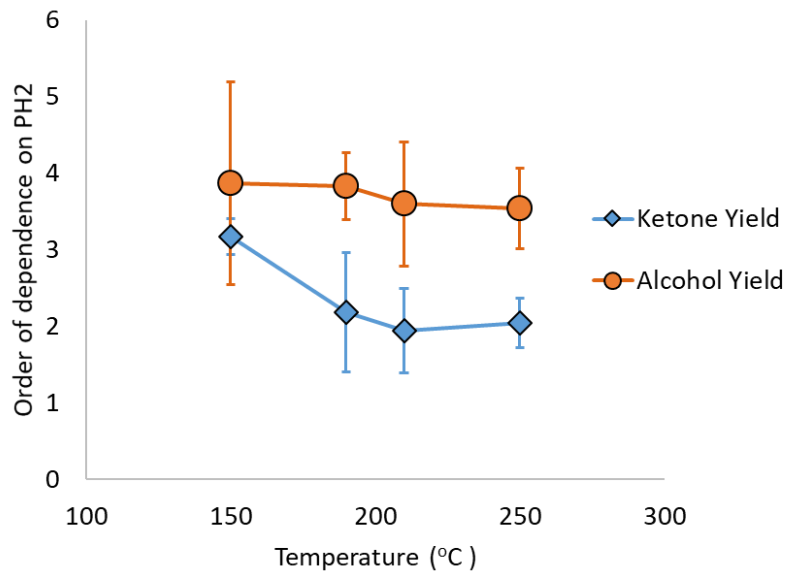
Figure 26. Order of dependence of ketone and alcohol formation on H2 pressure from 0.75-1 atm

After investigating different possible rate limiting steps, the only case where we have this high order of dependence on hydrogen is when the last hydrogenation step is rate-limiting for both ketone and alcohol. The elementary steps are as following.

$$Cr + * \overset{K_C}{\rightleftharpoons} Cr *$$

$$H_2 + 2 ** \overset{K_H}{\rightleftharpoons} 2H **$$

$$Cr * + H ** \overset{K_1}{\rightleftharpoons} CrH * + **$$

$$CrH * + H ** \overset{K_2}{\rightleftharpoons} CrH_2 * + **$$

$$CrH_2 * + H ** \overset{K_3}{\rightleftharpoons} CrH_3 * + **$$

For ketone formation

$$CrH_3 * + H ** \overset{k'}{\rightarrow} ONE * + ** \qquad \text{RDS}$$

$$ONE * \overset{K_K^{-1}}{\rightleftharpoons} ONE + *$$

For alcohol formation

$$CrH_3 * + H ** \overset{K_4}{\rightleftharpoons} CrH_4 * + **$$

$$CrH_4 * + H ** \overset{K_5}{\rightleftharpoons} CrH_5 * + **$$

$$CrH_5 * + H ** \overset{k''}{\rightarrow} OL * + ** \qquad \text{RDS}$$

$$OL * \overset{K_O^{-1}}{\rightleftharpoons} OL + *$$
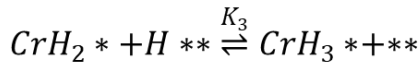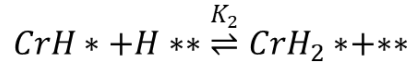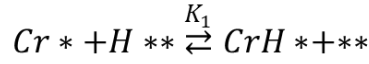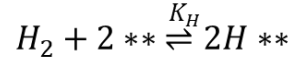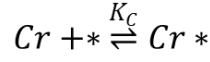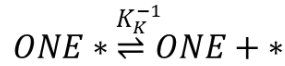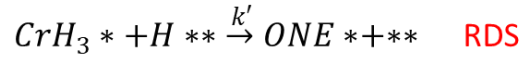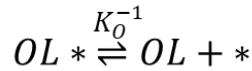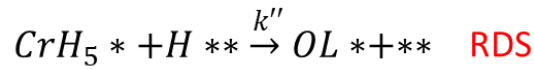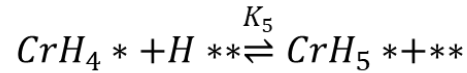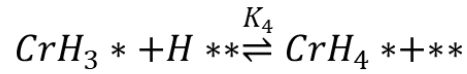
Based on these elementary steps, the reaction rates for ketone and alcohol formation from m-cresol were derived and we obtain these following rate expressions.

$$r_{CK} = \frac{k_{CK} K_C P_C P_{H_2}^2}{(1 + K_C P_C + K_K P_K + K_O P_O)} \qquad \text{With } k_{CK} = k' K_1 K_2 K_3 K_H^2$$

$$r_{CO} = \frac{k_{CO}K_C P_C P_{H_2}^3}{(1 + K_C \, P_C + K_K P_K + K_O P_O)} \quad \text{With } k_{CO} = k'' K_1 K_2 K_3 K_4 K_5 K_H^3$$

From these rate expressions, we can see that the adsorption enthalpy and entropy for

K_C , K_K , K_O we have obtained in **Table 8** are the adsorption enthalpy and entropy for m-

cresol, ketone and alcohol.

Adsorption configuration of the kinetically active species

Using transition-state theory, it is possible to estimate the entropy lost upon

adsorption with different degree of freedom of the adsorbed molecule on the catalyst

surface.[79-81] The total entropy lost upon adsorption is the sum of translational, vibration

and rotational entropy lost. The translational entropy change from 3D in the gas phase to

2D on the catalyst surface is -77 J/molK while the vibrational entropy change is +4

J/molK because now the adsorbed species has extra C-Pt bond with stretching frequency

of ~300 cm^{-1}. The rotational entropy of m-cresol gas molecule is 34, 37 and 39 J/molK

for 3 rotational axes. Depending on the mobility of the adsorbed species, it can lose a

fraction or all rotational entropy. **Table 11** has listed the value for entropy of adsorption

at different degree of rotational freedom.

Table 11. Entropy of adsorption of m-cresol at different degree of rotational freedom

	m-Cresol entropy of adsorption (J/molK)
Preserve all degree of rotational freedom	-73
Lost 1 degree of rotational freedom	-112
Lost 2 degree of rotational freedom	-149
Lost all degree of rotational freedom	-183
Value from our kinetic model	-124

Based on the results in **Table 11**, we can see that the entropy of desorption derived from the fitting is in between losing 1 and 2 degrees of rotational freedom, which means that the molecule is quite mobile on the catalyst surface. The low adsorption enthalpy and entropy both indicate that the kinetically active species is a weakly adsorbed species.

The adsorption enthalpy of m-cresol is also compared with the literature values as listed in **Table 12**, which includes both experimental and theoretical DFT calculations for the binding energy of phenolic molecules on Pt(111) surface from different authors.

Table 12. Binding energy of m-cresol and phenol on Pt(111) from other works

Compound	Binding energy on Pt (kJ/mol)	Sources
m-Cresol	176	DFT, Tan et al.[13]
Phenol	$220 - 115\theta$	Calorimetry, Campbell et al.[82]
Phenol	215	DFT, Honkela et al.[83]

The adsorption enthalpy of m-cresol obtained from the kinetic model is only -76 kJ/mol and much smaller than the reported values in **Table 12**. Pt(111) is used as the model surface because it is one of the most common and stable surfaces of Pt metal.

One way to testify the numbers in **Table 12** is to force the kinetic model to have such a high adsorption enthalpy for m-cresol, as a result, the absolute value of adsorption entropy must significantly increase so that the model can catch up with the experimental data. However, at adsorption enthalpy of -150 to -200 kJ/mol, the entropy lost must be ~ 250-300 J/molK, which is extremely high. This means that the molecule loses most of its gas phase entropy and become completely immobile on the catalyst surface, which does not make much physical meaning because the adsorbed species needs some mobility so that the hydrogen addition/removal can happen. More importantly, with the high absolute

value for enthalpy and entropy of adsorption, the model fails to catch up with the experimental data satisfactorily, compared with the existing model.

Campbell has experimentally measured the heat of adsorption as a function of coverage and observed that the heat of adsorption of m-cresol strongly depends on the coverage. At full coverage of 1 (monolayer adsorption), the adsorption energy significantly drops to only ~85 kJ/mol from 220 kJ/mol at zero coverage. The measurement is executed by calorimetry measurement. However, the kinetically active species may not be able to be measured or quantified by calorimetry, because it could be just weakly adsorbed species whose heat of adsorption are completely overwhelmed by the strongly adsorbed but kinetically inactive spectators. To justify this hypothesis, the adsorption of m-cresol is set as a function of coverage, similar to the expression in **Table 12** from calorimetry measurement. The best fitting with this hypothesis gives the following expression for m-cresol heat of adsorption.

$$-\Delta H_{ads} = 115 - 11 * \theta$$

We can see that even with this coverage dependence enthalpy of adsorption, the change with coverage is not as significant as the values measured from calorimetry experiments. The adsorption energy is only 115 kJ/mol at zero coverage and drops to 104 at full coverage. With this coverage dependence adsorption enthalpy model, the adsorption entropy also must be more negative, at -185 J/molK, which means that the molecule is immobile on the surface. Similar to the above case, this does not make much physical sense either. More importantly, similar to the previous case when the adsorption

enthalpy is forced to have a bigger value than 150 kJ/mol, the model also fails to fit the experimental results satisfactorily.

Conclusion

The hydrogenation of m-cresol was studied over a wide range of temperature from 100 to 300℃ over Pt/SiO$_2$ catalyst. The hydrogenation yield was found to increases then drops as increasing temperature. The reason for this drop is determined to be due to the fast drop in m-cresol coverage at increasing temperature, while the other causes such as poisoning or equilibrium limitation are ruled out. The overall hydrogenation rate is found to have 0 order on cresol at low temperature (<150 ℃) and approaching order of 1 at higher temperature (~250 ℃), while the order of dependence on H2 pressure is higher, about 2 for 3-methylcyclohexanone formation and 3 for 3-methylcyclohexanone formation. The only scenario where that can happen is when the last hydrogenation step is rate limiting. Based on that observation, elementary steps are developed with a simple Langmuir-Hinshelwood model, which was able to fit the experimental data very satisfactorily with R^2=0.96.

Based on the developed kinetic model, the barrier for each hydrogenation steps are determined as well as the adsorption enthalpy and entropy for cresol, ketone and alcohol. The adsorption of m-cresol is determined to have a low enthalpy and entropy lost upon adsorption, which suggests that the kinetically active species for hydrogenation are the mobile and weakly bound species on Pt surface. This is also reasonable as hydrogenation require sequential addition of hydrogen atoms to the aromatic ring, if the m-cresol

molecule is too strongly adsorbed to the surface, it may inhibit the hydrogen addition ability, thus the strongly adsorb would be kinetically inert while the weakly adsorbed ones are the actual active species.

III. Controlling phenolic hydrodeoxygenation (HDO) by tailoring metal-O bond strength via specific catalyst metal type and particle size selection

Motivation and Literature Reviews

As shown in chapter 1, the oxygen functionalities in phenolic compounds, usually in the form of hydroxy $-OH$ or methoxy $-OCH_3$, make them reactive for many different $C-C$ bond formation chemistries such as alkylation, hydroxyalkylation, acylation [11, 17, 84] etc. to create longer chain molecules that fit into the fuel pool. However, after the $C-C$ bond forming step, these oxygen functionalities still remain on the aromatic ring, and it is necessary to perform hydrodeoxygenation (HDO) chemistry to remove oxygen and create hydrocarbon fuels. This work focuses on the removal of hydroxy $-OH$ functionality, with *m*-cresol as the model compound, since it is one of the dominant functionalities in biomass-derived compounds.

The HDO reaction of phenolic compounds has been extensively studied and reported in the literature over different metals and bimetallic alloys [85-89], different supports [90-92] or in cooperation with an acidic function [93-100]. Understanding the reaction mechanisms and finding relationships between the observed catalytic behavior and the catalyst structure is of crucial significance for optimizing catalyst design and selection.

In our previous studies, we have shown that the oxophilicity of the metal catalysts, reflecting the metal$-O$ bond strength, is a crucial descriptor of their HDO activity [101]. In a series of studies on the HDO of *m*-cresol and phenol as the model compounds, we have compared the reactivity and prevalent mechanisms over different metals, including

monometallic (Pt, Pd, Ru, Fe, Ni) and bimetallic catalysts supported on inert (SiO_2) [62,101-103] or more oxophilic supports [91]. In particular, SiO_2 is an inert support with minimum participation in the reaction, which has allowed us to focus on the catalytic behavior of the metals.

In this contribution, we analyze the observed trends with the oxophilicity of the metals and present new results on the effect of extent of metal atoms coordination, which can be controlled by varying the metal cluster size, which in turn affects oxophilicity, and consequently the HDO activity. The dramatic effects of particle size were also observed for other chemistries such as hydrogenolysis and isomerization over metal catalysts. Works from Gault et al. have shown that the changes commonly observed in product selectivity with varying particle size can be traced to changes in reaction mechanisms, which in turn are related to the number of low-coordination (corner and edge) atoms relative to high-coordination (face or terrace) atoms [104-108]. The same concept can be applied in this case to interpret changes in HDO reaction mechanism and selectivity changes for the conversion of phenolics on different metal catalysts.

1. HDO of m-Cresol on Different Types of Metal

As depicted in **Figure 27**, when *m*-cresol is converted in the presence of H_2 over different metal catalysts, two types of products are typically observed: (a) hydrogenation products (3-methylcyclohexanone and 3-methylcyclohexanol) and (b) hydrodeoxygenation products (toluene, methylcyclohexane and 3-methylcyclohexene). In principle, toluene could be produced via two different pathways: (1) hydrogenation of *m*-cresol to 3-methylcyclohexanol, followed by dehydration to 3-methylcyclohexene and further dehydrogenation to toluene, and (2) direct HDO from *m*-cresol.
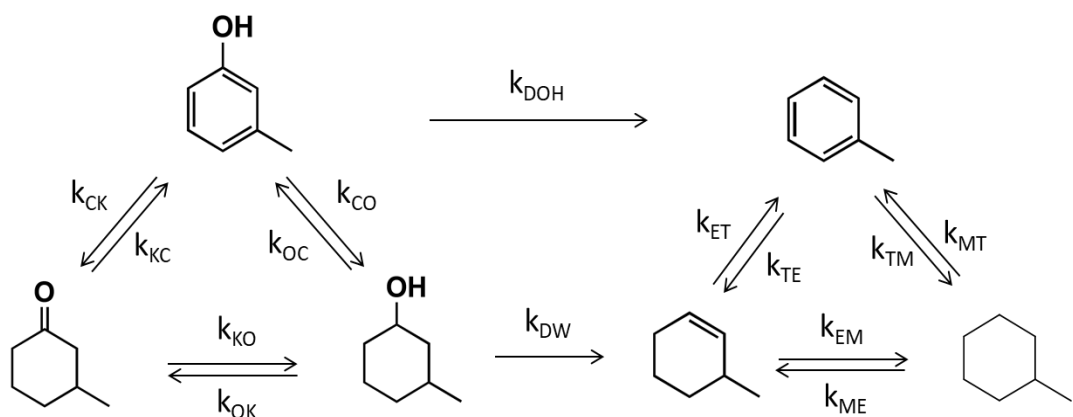
Figure 27. Reaction pathway for HDO of m-cresol (modified with permission from [1]

HDO of m-cresol over Pt catalyst

In a detailed kinetic study conducted with a Pt/SiO_2 catalyst, [103, 109] we showed that pathway (1) only occurs to a very low extent due to the low acidity of the SiO_2 support. As shown in **Figure 28**, the yield of toluene increases with increasing *m*-cresol conversion but when 3-methylclohexanol or 3-methylcyclohexanone was used as feed, the yield of toluene remains almost zero in all cases, even at high feed conversions, which shows that toluene is not obtained from the alcohol or the saturated ketone.

67
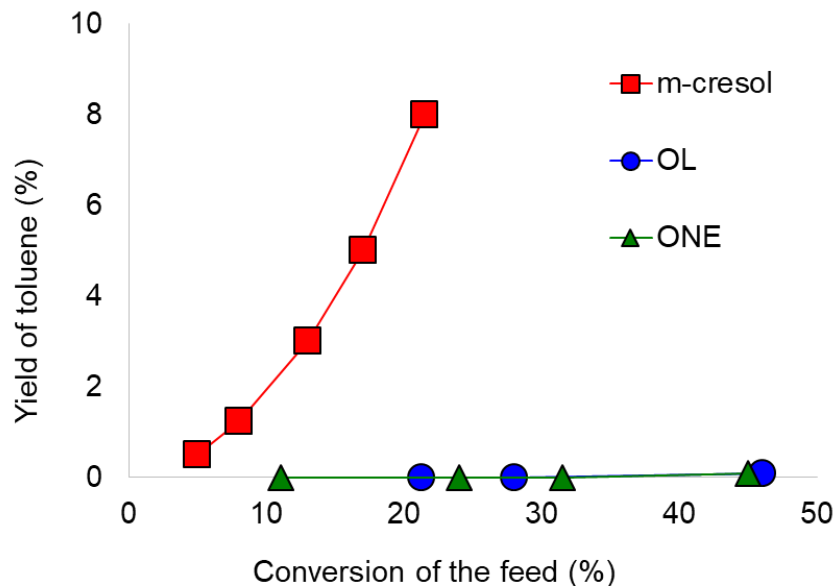
Figure 28. The yield of toluene vs. conversion of feed over Pt/SiO$_2$ at 300°C with different feeds including m-cresol, 3-methylcyclohexanol (OL) and 3-methycyclohexanone (ONE) (modified with permission from [1]).

Table 13. The yield of toluene (TOL) and methylcyclohexane(MCH) when 3-methylcyclohexene was fed over Pt/SiO$_2$ at 300°C (modified with permission from [103]).

Conversion of 3-methylcyclohexene (%)	Yield (%)		Ratio TOL/MCANE
	TOL	MCANE	
13.3	1.7	1.9	0.89
18.9	4.7	3.9	1.2

It was also clearly demonstrated that toluene was not derived from methylcyclohexene either. In fact, as shown in **Table 13**, at low conversions over Pt/SiO$_2$, methylcyclohexene results in a toluene to methylcyclohexane ratio of about unity. This ratio gradually increases to its equilibrium value (~11 at 300°C) with feed conversion. That is, far from equilibrium, the methylcyclohexene-to-toluene and methylcyclohexene-to- methylcyclohexane reactions occur at similar rates, but as conversion increases, the

68

secondary methylcyclohexane to toluene reaction drives the toluene/methylcyclohexane ratio close to the equilibrium of 11. This was indeed the trend observed when the feed was either 3-methylcyclohexanol or 3-methylcyclohexanone over the Pt/SiO$_2$ catalyst.
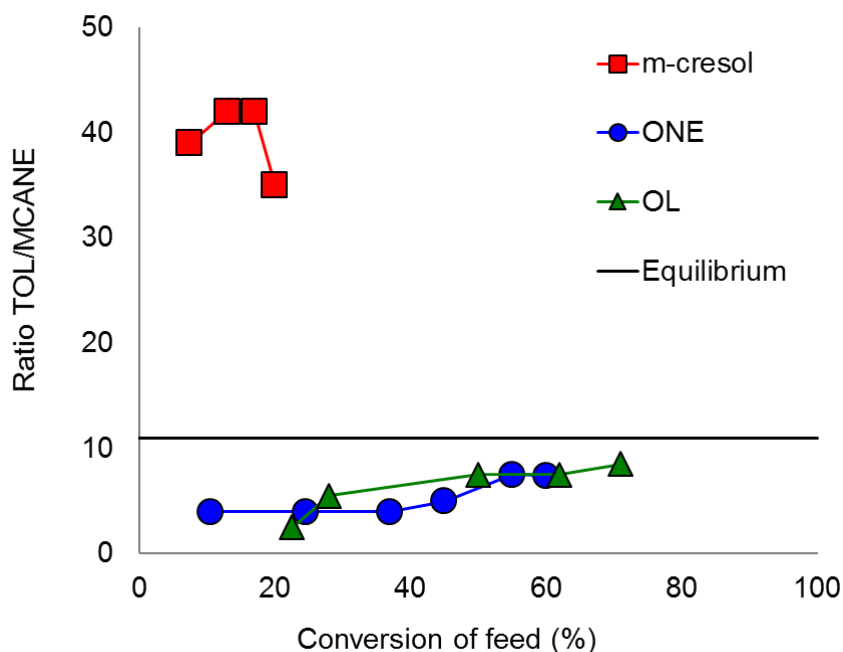
Figure 29. The ratio of toluene (TOL) to methylcyclohexane (MCANE) vs. conversion of different kinds of feed including m-cresol, 3-methylcyclohexanone (ONE) and 3-methylcyclohexanol (OL) over Pt/SiO2 at 300°C (modified with permission from [54]).

As shown in **Figure 29**, when 3-methylcyclohexanol or 3-methylcyclohexanone was fed over the Pt/SiO$_2$ catalyst, the toluene/methylcyclohexane ratio was near unity at low feed conversion and only increased to near 10-11 as the feed conversion increased. This is reasonable since 3-methylcyclohexanol was slowly dehydrated to methylcyclohexene, followed by simultaneous hydrogenation to methylcyclohexane and dehydrogenation to toluene. However, a drastically different pattern was observed when *m*-cresol was used as the feed. In this case, even at the lowest feed conversions, the

toluene/methylcyclohexane ratio was much greater than the equilibrium value of 11. Clearly, this trend indicates that toluene is not formed from any of the hydrogenated intermediates, but rather directly from *m*-cresol, while methylcyclohexane is mostly produced from secondary hydrogenation of toluene. It should be noticed that this may not be the case when Pt is supported on more acidic supports, in which the acid-catalyzed dehydration of 3-methylcyclohexanol become significant [110].

The mechanism of *m*-cresol conversion to toluene is rather puzzling since a direct C−O bond cleavage may not be possible on Pt due to the low metal-oxygen bond strength which results in a high activation energy for direct deoxygenation. Therefore, a different reaction pathway must be considered to explain the production of toluene as an observed primary product.

Mechanism of hydroxy -OH removal from m-cresol

As illustrated in the reaction scheme of **Figure 30,** we have proposed that the direct conversion of *m*-cresol to toluene can alternatively happen via two different mechanisms, direct deoxygenation (DDO) and tautomerization (TAU) [101]. In the DDO mechanism, the $C_{aromatic}$−O bond would undergo direct cleavage to toluene and water, while in the TAU mechanism, the keto-enol isomer of *m*-cresol would undergo hydrogenation at the C=O to an intermediate alcohol followed by dehydration to toluene. The nature of the metal catalyst determines which one is the more plausible mechanism.

Our previous study using DFT calculations has shown that, in the case of Pt(111), the energy barrier for the DDO pathway is exceedingly high (242 kJ/mol). Therefore, on such a surface, the HDO has to proceed via a different mechanism. In fact, the DFT

calculations show that the proposed TAU pathway is plausible, with a significantly lower energy barrier (203 kJ/mol) and the rate limiting step is determined by the final dehydration of the cyclic diene alcohol intermediate. While dehydration is not particularly favorable over Pt, this path is energetically favored compared to the direct C−O bond cleavage [101].
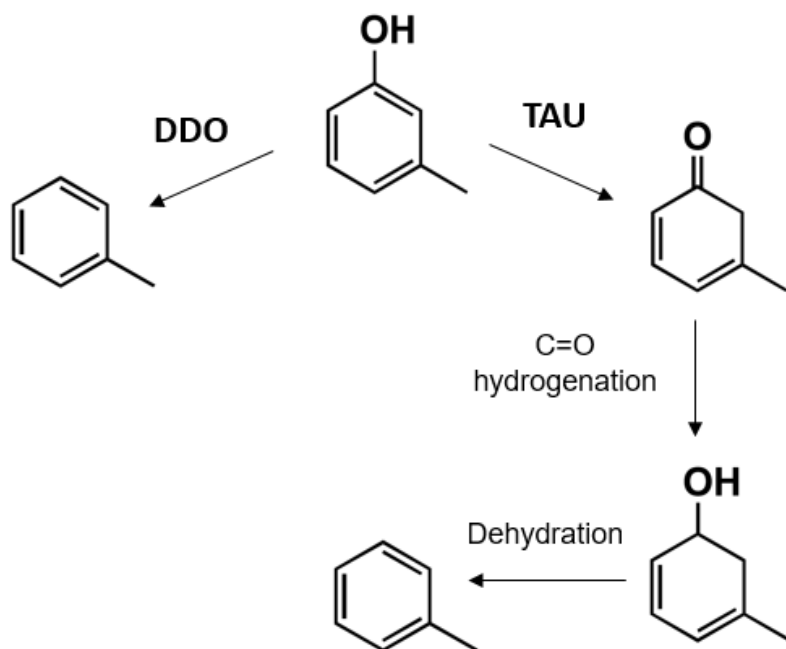
Figure 30. HDO mechanism for the conversion of m-cresol to toluene, direct deoxygenation (DDO) and tautomerization (TAU).

As shown in **Figure 31**, the DFT calculated energy barriers for the direct deoxygenation (DDO) of *m*-cresol correlate very well with the oxophilicity of the metal catalysts. That is, the metal-O bond strength (oxophilicity) increases in the order Pt < Pd < Rh < Ru < Fe. When plotted in the same graph, the calculated energy barriers for the DDO of *m*-cresol decease linearly from Pt to Fe. As a result, while over Pt, the TAU

71

pathway is more favorable than the DDO pathway, the opposite is true on more oxophilic

metals such as Rh, Ru or Fe.
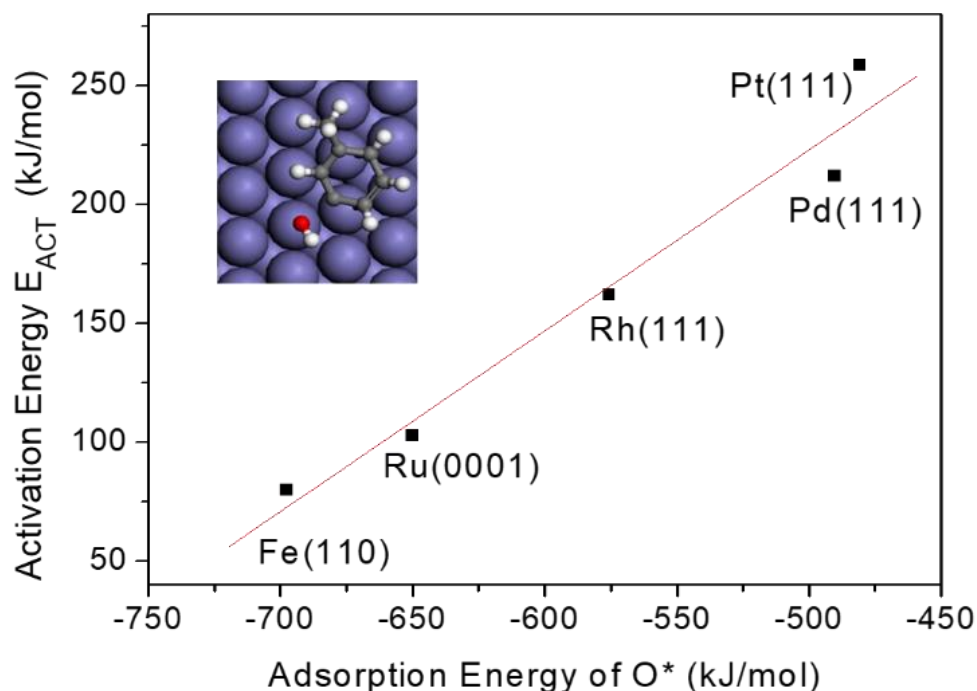
Figure 31. Correlation between activation energy for direct deoxygenation (DDO) of m-cresol and the adsorption energy of O* over different metals. Modified with permission from [101]

2. *HDO of Anisole on Different Types of Metal*

Anisole is an interesting model compound for HDO reactions since the methoxy

functionality has two possible types of C-O bond cleavage, that is, Caryl-O or Calkyl-O.

In recent work, we have comparatively studied the HDO reaction of anisole over Pt, Ru

and Fe catalysts. Interestingly, on all three metals, the Calkyl-O bond is cleaved first,

produce the same phenoxy intermediate, C6H5O* (see **Figure 32**). However, the fate of

this intermediate varies from metal to metal, and the mechanisms responsible for the

different outcomes are directly related to the metal oxophilicity. Indeed, as shown in

Figure 33, the ratio of phenol to benzene was plotted versus anisole conversion over Pt, Ru and Fe. This ratio, particularly at low anisole conversion, reflects the fate of the phenoxy intermediate C6H5O* on different metals. The higher ratio means that the catalyst favors hydrogenation of the phenoxy intermediate to phenol, while lower ratio means the catalyst favors deoxygenation of the phenoxy intermediate to benzene. Over Pt catalyst, this ratio is very high at low anisole conversion, which means that phenol is the primary product. This ratio drops at increasing anisole conversion indicates that benzene is a secondary product that is formed from HDO of phenol. This phenomenon is in good agreement with the DFT calculations that on a low oxophilicity metal like Pt, the barrier for Caryl-O cleavage is very high (270 kJ/mol), so DDO cannot occur. By contrast, the hydrogenation of the phenoxy intermediate has a low energy barrier (17 kJ/mol) and it produces phenol as the primary product.
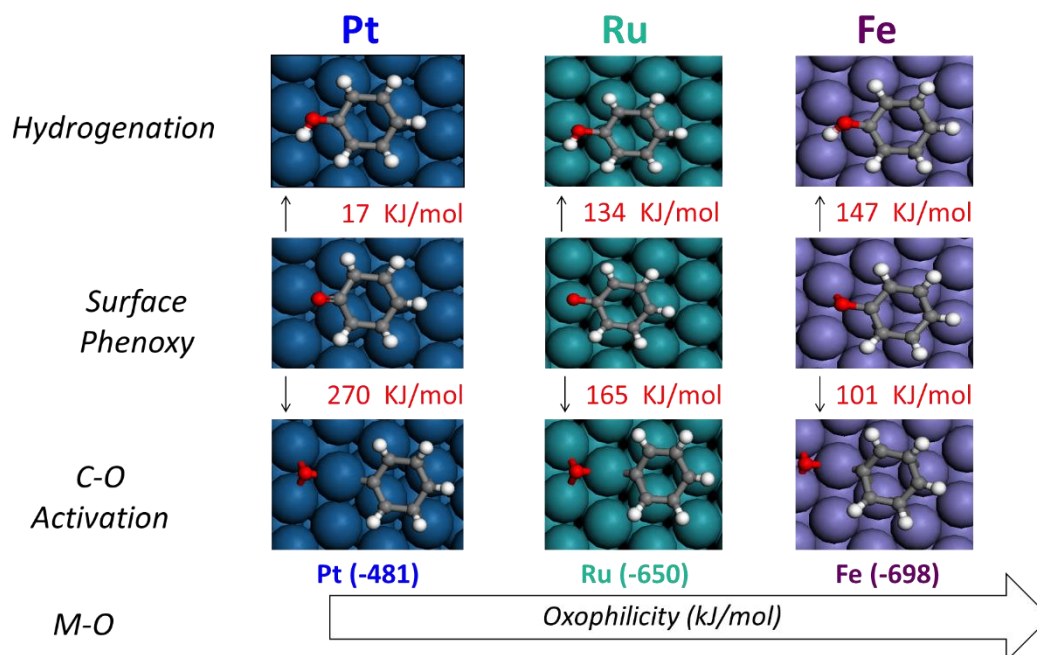
Figure 32. Energy barriers for hydrogenation and C-O bond cleavage of surface phenoxy intermediate C6H5O* on Pt, Ru and Fe (Modified with permission from [62]
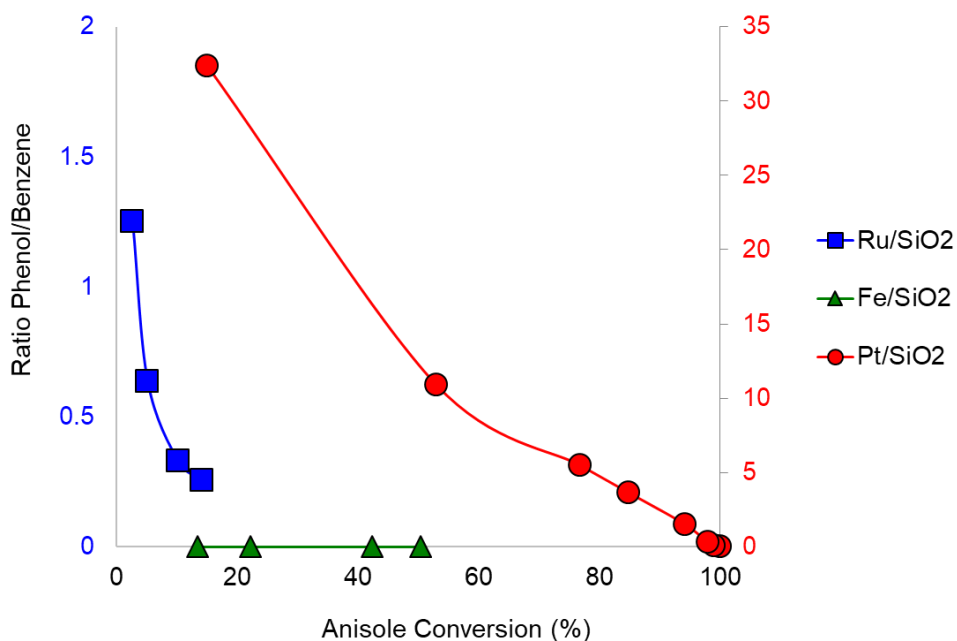
Figure 33. Ratio of phenol to benzene as a function of anisole conversion over different catalysts. Modified with permission from [62]

An opposite behavior is observed on a more oxophilic metal like Fe, over which the phenoxy intermediate undergoes direct Caryl-O cleavage, producing benzene (energy barrier for DDO is lower than that for hydrogenation). As seen in **Figure 33**, phenol to benzene ratio is zero at all anisole conversion, which means that benzene is the only primary product and no phenol is observed. This is also in good agreement with the DFT calculations, giving support to the proposed reaction pathways. On a metal with intermediate oxophilicity like Ru, this ratio is in between Pt and Fe, both benzene and phenol are primary products. This is also in good agreement with DFT calculations that the energy barriers for hydrogenation and C-O bond cleavage of the phenoxy intermediate are in the same range

74

3. *Relationship between Metal Atoms Coordination and Oxophilicity*

Oxophilicity, as measured by the M$-$O bond strength, is a direct function of the position of the d-band center [111]. As the d-band center is closer to the Fermi level, the antibonding orbital of the hybridization between metal and oxygen is further away from the Fermi level and has a low electron occupancy. Therefore, the M$-$O bond becomes stronger and the metal is more oxophilic. The d-band center gets closer to the Fermi level as one moves upward and to the left in the periodic table. To further illustrate this trend, as shown in **Figure 34**, the adsorption energy of O* increases as the d-band center is closer to the Fermi energy (0 eV). Theoretical and experimental studies have shown that the d-band center also depends on the extent of metal atom coordination. That is, surface defects such as steps, edges and kinks with smaller coordination are more free atom-like and have sharper d-bands. Thus, to maintain the same occupancy of d-state electrons, the d-band center shifts closer to the Fermi level. This shift does not occur to such a large extent for terrace atoms with high coordination and broader d-bands [112-115]. Therefore, we can expect that the HDO activity of metal should be strongly influenced not only by the metal type, but also by the atomic coordination. Lower coordination sites are more dominant on small metal clusters, while the high coordination sites are more dominant on large metal clusters.
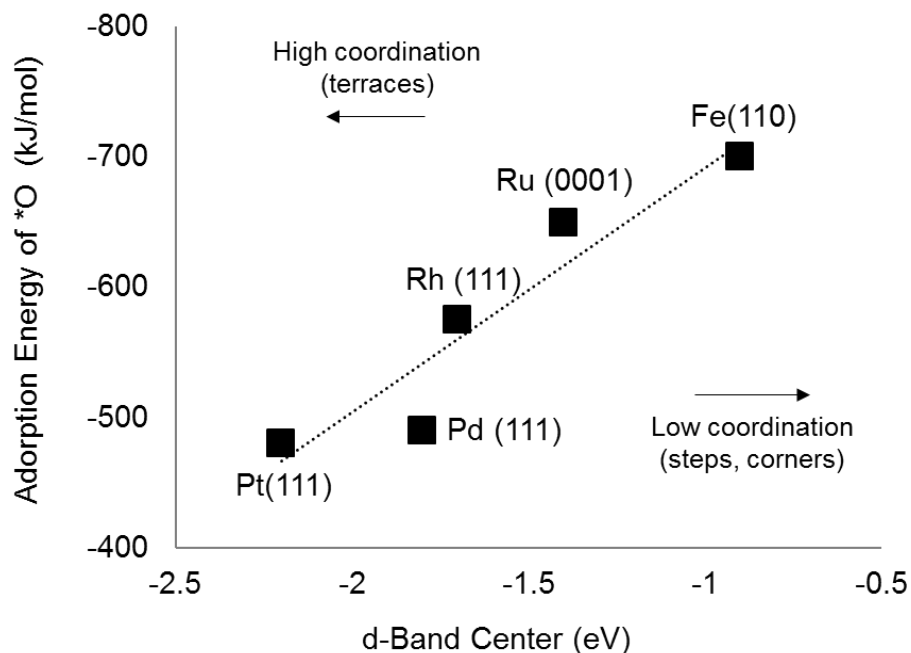
Figure 34. Correlation between adsorption energy of O*(kJ/mol) and d-band center (eV).

To further explore this concept, the hydrodeoxygenation of *m*-cresol was investigated on two Rh catalysts with varying particle size to compare the resulting product distributions and overall catalytic behavior. The metal Rh was chosen because it has an intermediate oxophilicity (bulk d-band center = -1.7 eV, M−O bond = -575 kJ/mol), which is between those of Pt and Ru and may thus evidence the particle-size effects more clearly. On the former, the M−O bond strength is too weak to catalyze DDO and on the latter it may be too strong to show variations between low- and high-coordination sites.

Characterization of Rh/SiO$_2$ Catalysts of Different Particle Sizes

Two Rh/SiO$_2$ catalysts were synthesized with varying metal loading (2.5 and 7 wt %) and treated at different reduction temperatures to obtain different ranges of particle sizes and surface defects. The two catalysts were characterized by HRTEM and DRIFTS

analysis of adsorbed CO after in-situ reduction. As shown in **Figure 35**, TEM analysis of the two catalysts clearly reflect the different ranges of metal cluster sizes and shapes. The high-temperature treated 7 wt. % Rh/SiO$_2$ catalyst contains bigger and better-defined metal particles compared with the low-temperature treated 2.5 wt.% Rh/SiO$_2$ catalyst. A histogram indicating the different average particle sizes (4 vs. 2 nm) is included in the **Figure 36**.
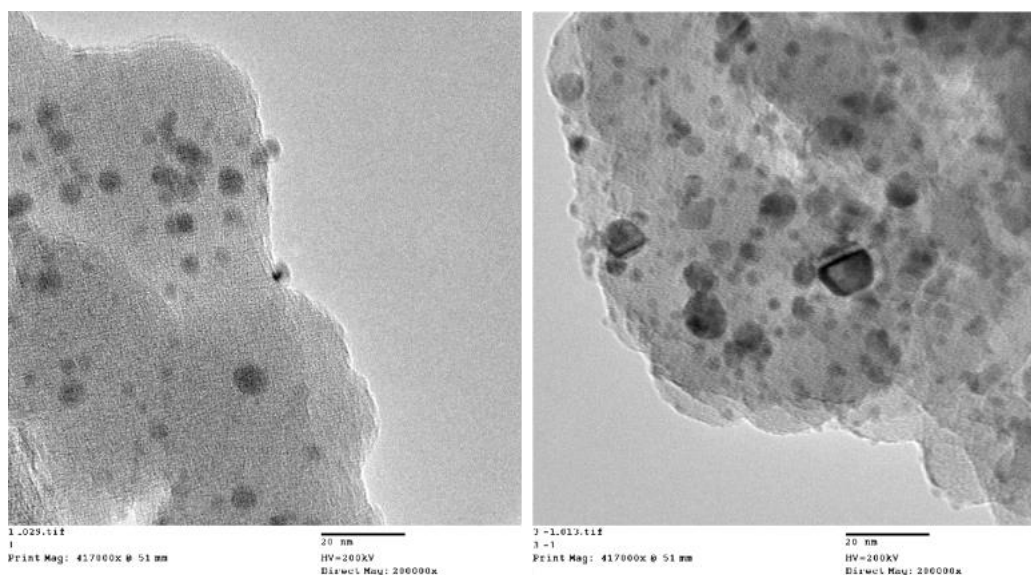
Figure 35. HRTEM of 2.5 wt.% Rh/SiO2 (left) and 7 wt.% Rh/SiO2 (right) catalysts
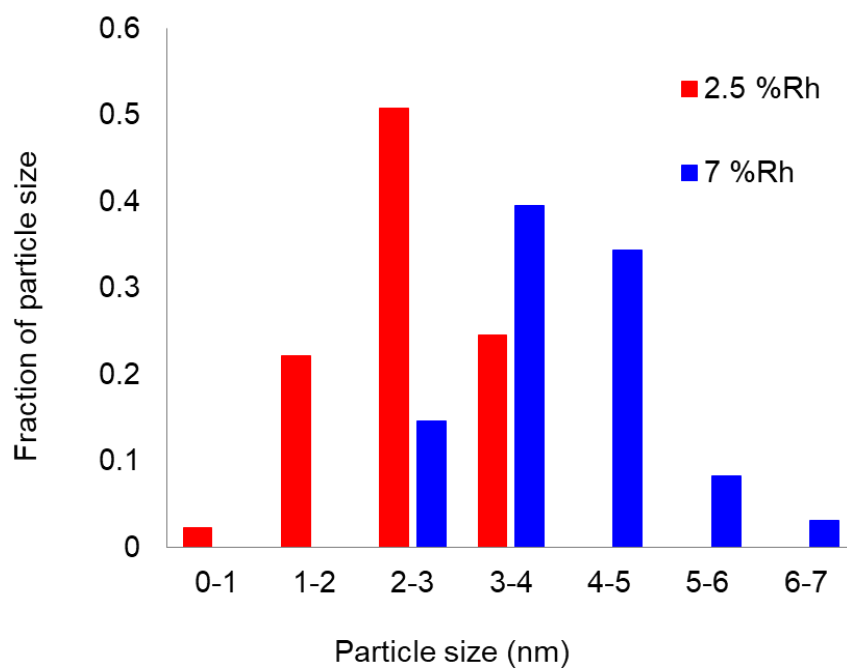
Figure 36. Particle size distribution 2.5 wt.% Rh/SiO2 and 7 wt.% Rh/SiO2 catalysts
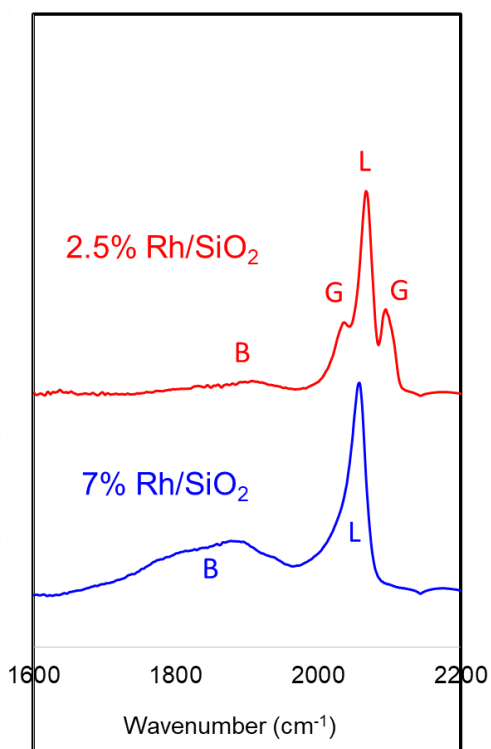
Figure 37. DRIFTS of CO adsorption over 2.5 wt.% Rh/SiO2 and 7 wt.% Rh/SiO2 catalysts.

These observations were further corroborated by DRIFT analysis of adsorbed CO (see **Figure 37**). This technique is particularly suited to characterize Rh catalysts of varying coordination numbers and particle sizes. It is well known that CO can adsorb on Rh via three different adsorption modes: linear (L), gem (G) and bridge (B). In the linear mode (2050-2070 cm^{-1}), a single CO molecule adsorbs on a top single metal site. Generally, the frequency of this band shifts to lower values as the surface coverage increases. In the gem mode, two CO molecules adsorb on a single metal site, generating a doublet of vibrational modes, corresponding to the concerted symmetric and asymmetric (2030 and 2100 cm^{-1}) vibrational modes. When CO molecules adsorb on small metal particles, the repulsion forces among adsorbed CO molecules can be strong enough to disrupt the metal cluster [116]. This phenomenon could happen when the metal-support interaction is weak, which is our case since SiO_2 was used as an inert support. The resulting single metal atom can accomodate two CO molecules, giving rise to the gem vibrational modes (G). This doublet is a fingerprint for the presence of small, defective Rh clusters in a high state of dispersion over the support [117-119]. Finally, the bridge mode corresponds to one CO molecule adsorbed on an ensemble of metal sites (1800-1900 cm^{-1}) [120]. While the gem and linear mode are usually rather sharp bands, the bridge mode is significantly broader, since CO can adsorb on metal site multiple of varying number (2, 3 or 4), which results in a broad band including a range of frequencies.

Significant differences in the IR spectra are clearly evident in **Figure 37**. The low-temperature treated 2.5 wt.% Rh/SiO_2 catalyst, with the smaller metal particles, exhibits features that are consistent with a high density of low-coordination surface sites. In

addition to the linear CO band (L), this catalyst (TEM ~ 2 nm) shows intense gem (G) dicarbonyl bands and a much smaller bridge (B) band than the 7 wt.% Rh catalyst (TEM ~ 4 nm), which shows a dominant bridge (B) band, and complete absence of the gem dicarbonyl bands (G). Also, the shift to lower frequencies observed on the linear (L) band for this catalyst is consistent with a higher extent of adsorbate-adsorbate interaction, also typical of flat planes and generally associate to dipole-dipole interactions [121].

That is, the TEM results and DRIFT profiles unequivocally demonstrate that the 7 wt.% Rh/SiO_2 contains a higher density of flat plane terraces than the 2.5 wt.% Rh/SiO_2 catalyst, which in turn contains a higher proportion of small metal clusters with more steps and edges. The 2.5 wt.% Rh/SiO_2 with more steps and edges will have the d-band center closer to the Fermi level, which makes it more oxophilic, while the 7 wt.% Rh/SiO_2 would be less oxophilic [122].

m-Cresol Conversion on Rh of Different Particle Size

1. Testing catalytic activity

To precisely monitor the change in activity of the two different surfaces (i.e. 2.5 and 7 wt % Rh), starting from the pristine surface to one partially covered by poisons such as carbonaceous fragments or oxygen species, catalytic measurements were conduct in a micro-pulse reactor. In this device, the catalyst after in-situ reduction was kept at the reaction temperature (285°C in this study) under pure H_2 stream all the time, while a small and controlled amount of feed was periodically injected into the catalyst bed. This micro-pulse reactor system allows us to precisely monitor the effects of the initial stages of catalyst deactivation and approach to steady state conditions starting with the pristine

catalyst. This reactor is particularly valuable for observing activity/structure relationships, minimizing the secondary effects that carbonaceous deposits may have on the activity and selectivity of the catalyst, which is not possible in a conventional steady-state continuous flow reactor. Moreover, the study of the behavior of pristine catalysts can be more directly related to DFT calculations, which typically simulate the interaction of the reactants with a pristine metal surface.

In this case, the two catalysts (2.5 wt.% and 7 wt.% Rh/SiO_2) were tested for their catalytic activity for the HDO of *m*-cresol, keeping the overall *m*-cresol conversion at ~30% and constant *m*-cresol partial pressure in the feed. The turnover number of each product was normalized by the number of exposed Rh metal atoms, calculated based on particle size from TEM with the assumption of hemispherical particle shape. **Figure 38** shows the variation of normalized turnover number (TON) for each product as a function of the pulse number. It is observed that the TON to HDO (toluene) and hydrogenation (OL and ONE) products is higher on the 2.5 wt.% Rh than on the 7 wt.% Rh, which means that the small particle size is more active for HDO and hydrogenation of *m*-cresol. On the other hand, the TON to cracking products C2-C6 is similar for both cases. It should be noticed that the cracking products (lighter than C6) were not observed over Pt catalyst at the same reaction conditions. By contrasts, over more oxophilic metals such as Rh and Ru significant amount of cracking products were observed.

81
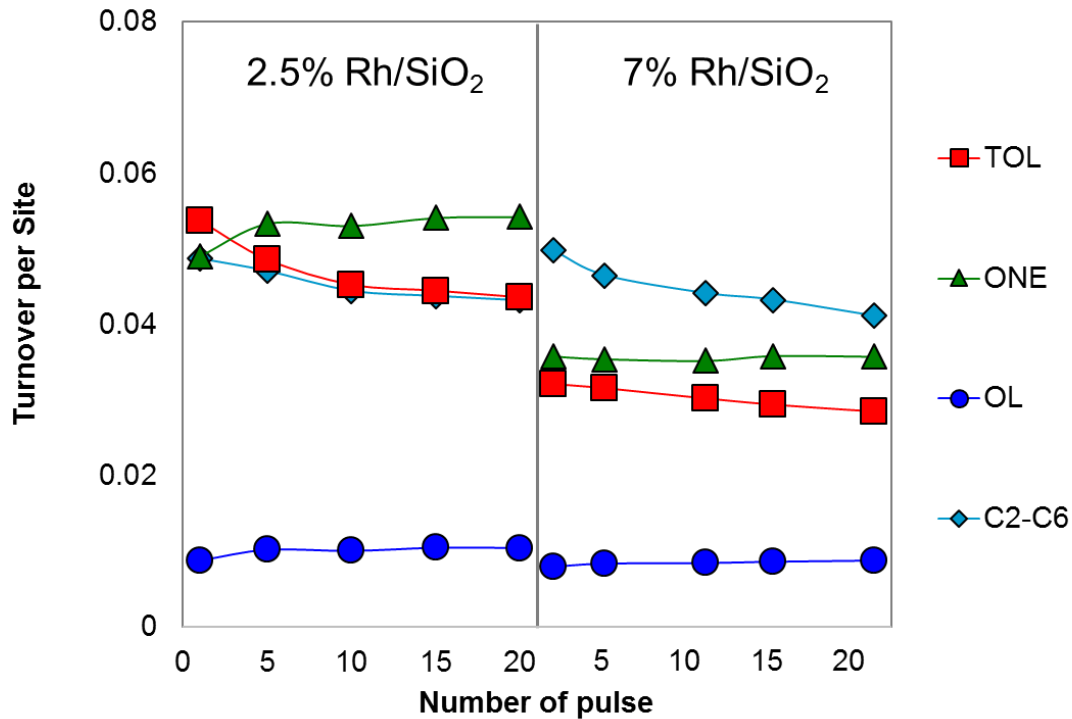
Figure 38. The turnover frequency (TOF) from m-cresol to different products including toluene(TOL), 3-methylcyclohexanone (ONE), 3-methylcyclohexanol (OL) and cracking products (C2-C6) at increasing number of pulses of 2.5 wt% and 7.5 wt.% Rh/SiO$_2$ at 285°C.

Interestingly, in the case of 2.5 wt.% Rh/SiO$_2$ catalyst, the rate of formation of toluene in the first pulse was higher than that of 3-methylcyclohexanone (ONE) (0.054 vs 0.049), but toluene quickly dropped while ONE increased. As a result, at the 20th pulse, the TON of toluene became smaller than that of ONE (0.043 vs. 0.054). This trend may indicate that very active HDO sites are initially present on the small Rh particles, readily converting *m*-cresol to toluene, but they are quickly deactivated, allowing hydrogenation to ONE and OL become dominant.

By contrast, in the case of the 7 wt.% Rh/SiO$_2$ catalyst, TON of toluene is lower than that on 2.5 wt.% Rh catalyst (0.032 vs. 0.054) even during the first pulse, but, does toluene not drop much in the subsequent pulses; that is, toluene only dropped from 0.032 in the

1st pulse to 0.028 in the 20th pulse. This behavior indicates that the high-coordination terraces sites (typical of large particles) in 7% Rh catalyst are less active for HDO but they retain their activity more effectively.

The common trend observed on both large and small Rh particles is that as the catalyst deactivates, the yield to HDO product decreases while that for the hydrogenation products increases. Micro-pulse reactor is proven in this study to be a very useful tool to monitor the deactivation and has helped us to follow changes in activity and selectivity as some of the most active sites become deactivated.

2. DFT Calculations of m-Cresol on Different Rh Surfaces

To model the behavior of a flat terrace and a defective surface, DFT calculations were conducted over a Rh(111) terrace site and a Rh(533) step site, respectively. These calculations have allowed to understand how the different sites influence the HDO of *m*-cresol and how they deactivate. First, the binding energy of atomic oxygen was calculated over the two surfaces. As shown in **Table 14**, the strength of the O bonding was significantly higher on the stepped Rh(533) surface (-610 kJ/mol) than on the Rh(111) flat surface (-575 kJ/mol), which substantiates the initial expectation that the step site is more oxophilic than the terrace site.

Table 14. Summary of the adsorption energies of atomic oxygen and carbon, and the energy barriers and reaction energies for the hydrogenation of OH* and carbon species CH_x* on Rh(111) and Rh(533) in kJ/mol.

	Rh(111)		Rh(533)	
	E_{ads}		E_{ads}	
O*	-575		-610	
C*	-699		-766	
	E_{ACT}	E_{RXN}	E_{ACT}	E_{RXN}
OH* + H* -> H_2O*	68	-16	127	42
C* + H* -> CH*	67	-30	90	11
CH* + H* -> CH_2*	62	58	113	42
CH_2* + H* -> CH_3*	43	9	50	22
CH_3* + H* -> CH_4	53	-8	57	6

The removal of hydroxy $-$OH of *m*-cresol over Rh catalyst was proven to happen via direct deoxygenation (DDO), which is similar to the reaction observed on Ru, rather than the tautomerization (TAU) pathway predicted for Pt. That is, the energy barrier for DDO over Rh(111) is 164 kJ/mol, while the energy barrier for TAU is exceedingly high of 289 kJ/mol, the same trend that we calculated for Ru(0001) [101].

Therefore, the DDO reaction was modeled over the two surfaces Rh(111) and Rh(533). The structures of reactant, transition state and product are compared in **Figure 39**. It can be seen that, over the two metal surfaces, the C$-$O bond elongates from around 1.4 Å in the reactant to the transition state (2.09 Å for the Rh(111) and 2.15 Å for the Rh(533)). While the structure of the transition states is similar on the two surfaces the energetics is very different. For the Rh(111) terrace site, the energy barrier and reaction

energy for the C−O scission of *m*-cresol were calculated to be 164 and 90 kJ/mol, respectively. These values are significantly higher than the corresponding values for Rh(533) step site, which were calculated as 122 and 10 kJ/mol respectively. The less endothermic C−O cleavage reaction over the more oxophilic Rh(533) surface is consistent with the trends of the energy barrier vs. oxophilicity of different metals that we reported earlier [101]. This result is in good agreement with the experimental results that clearly show that the catalyst with the smaller Rh particles is more active.
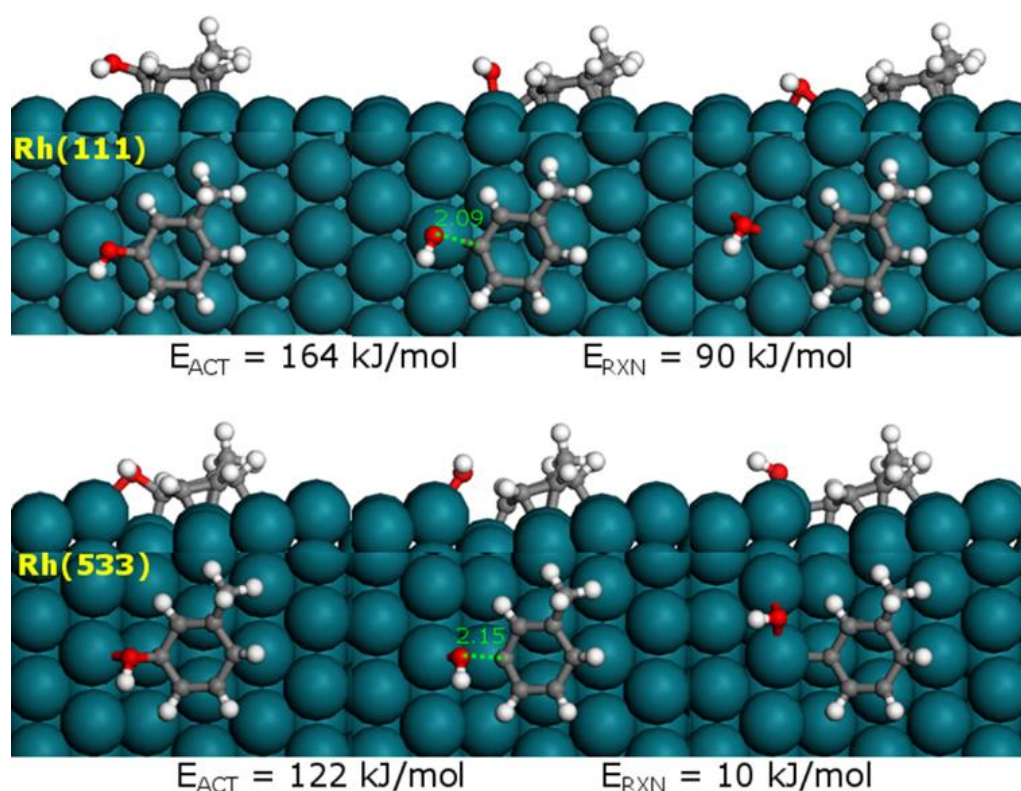
Figure 39. DFT calculated reactant, transition state and product structures for the deoxygenation of m-cresol on Rh(111) and Rh(533)
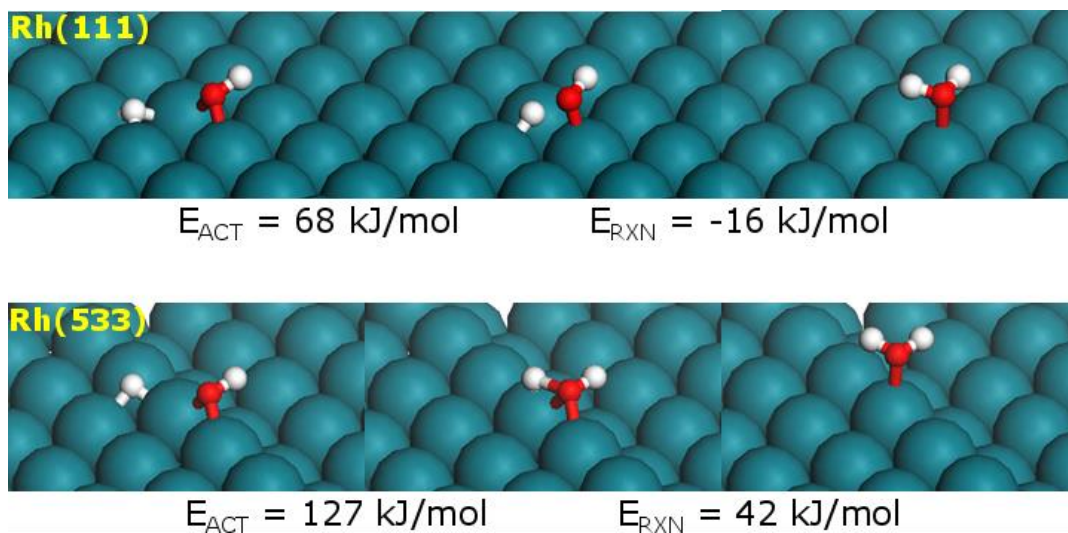
Figure 40. DFT calculated reactant, transition state and product structures for the hydrogenation of OH* on Rh(111) and Rh(533).

To rationalize the observed deactivation behavior displayed by the two different catalysts as a function of the number of subsequent pulses, we conducted additional DFT calculations. We speculate that upon deoxygenation of *m*-cresol, the surface OH* formed as a fragment of the DDO reaction needs to be removed via hydrogenation and formation of water. The energy requirement for this "site cleaning" will be a measure of the propensity of a given site to catalyst deactivation. As shown in **Figure 40**, the energy barrier for the hydrogenation of OH* to form water on the Rh(533) step site is calculated to be 127 kJ/mol, which is much higher than the energy barrier required over the Rh(111) terrace site (68 kJ/mol). Consistently, the reaction energy for the "site cleaning" is more endothermic for the step site (42 kJ/mol) than for the terrace site (-16 kJ/mol). It is then clear that the oxophilicity of the surface site influences the *m*-cresol deoxygenation and OH* hydrogenation reactions in the opposite direction. The more oxophilic is the site and the stronger it binds to oxygen, the more active it is for the DDO reaction. However, the

86

hydrogenation reaction requires the weakening of the metal-oxygen bond to reconstitute the clean active site. Obviously, this step is disfavored on the more oxophilic site. That is, the more difficult removal of the OH* from the Rh(533) step site reflects a higher tendency for site blockage.

Additionally, since C−C cracking occurs to a significant extent during the HDO of *m*-cresol over the Rh catalysts, carbon species could also be formed on the metal surfaces, participating in site blocking and consequent deactivation. Therefore, we have also calculated the hydrogenation of different carbon species CH_x (x = 1~3) on the two Rh surfaces. The calculated energetics are summarized in **Table 14**. We can see that similar to case of OH*, the hydrogenation of carbon species CH_x is more difficult on the Rh(533) step site with higher energy barrier and more endothermic reaction energies than on the Rh(111) terrace site. This is expected, and in correspondence with the stronger metal-carbon bonding at the Rh(533) site (-766 kJ/mol) compared to the Rh(111) (-699 kJ/mol).

Based on this analysis, it can be concluded that the step and other low-coordination sites, which are more dominant on small metal particles, are initially more active for the direct deoxygenation reaction of *m*-cresol due to its higher oxophilicity. However, the stronger binding of oxygen and carbon species at these step sites also inhibits their subsequent removal to keep the low-coordination site available, which leads to deactivation. This conclusion is supported by experimental observations, which demonstrates that the 2.5%Rh/SiO$_2$ catalyst with smaller metal particles is more active and selective in the HDO of *m*-cresol. However, it deactivates faster than the 7%Rh/SiO$_2$ catalyst.

Conclusion

Metal particle size strongly affects HDO activity of rhodium catalysts. Small Rh particles with low coordination sites are more active than large particles with high coordination sites for HDO of *m*-cresol to toluene, but also get more easily deactivated. The experimental results are confirmed by DFT calculations, which show that the energy barrier for direct C−O bond cleavage is lower on Rh(533) step sites than on Rh(111) terraces. Furthermore, the energy barrier required to remove the adsorbed O* or C* is higher on Rh(533), therefore it is harder to clean the step sites and the deactivation is more pronounced.

Aligned with previous study, the metal oxophicility is proven to be good descriptor for the corresponding metal HDO activity. We can control the metal oxophilicity by tailoring d-band center by either changing the type of metal or the coordination of the metal atoms. This is important in the design and selection of metal catalysts for HDO of phenolic compounds.

Materials and Methods

Catalysts preparation

Two Rh/SiO$_2$ samples with different metal particle sizes were prepared by incipient wetness impregnation of SiO$_2$ (Hi-sil 290), used as the support, with an aqueous solution of Rhodium(III) nitrate, purchased from Sigma-Aldrich (10 wt. % Rh in >5 wt. % HNO$_3$). The metal loading and treatment conditions were manipulated to control the particle sizes of these catalysts. After impregnation, the low-loading catalyst (2.5 wt.% Rh/SiO$_2$) was

heated under H_2 at 200°C for 2 h, while the high-loading catalyst (7 wt.% Rh/SiO_2) was heated under N_2 at 550°C for 2 h, and then for additional 12 h at 550°C under H_2.

Catalysts characterization

Samples were characterized by transmission electron microscopy (TEM) and diffuse reflectance infrared Fourier transform spectroscopy (DRIFTS). TEM images were obtained on a JEOL 2000 field emission system operated at 200 kV. For this analysis, the pre-reduced catalysts were dispersed in ethanol and sonicated with a horn sonicator (Cole-Parmer), operating at 25% amplitude for 10 min before deposition onto holey carbon coated copper grids. DRIFTS of adsorbed CO was performed on a Perkin-Elmer Spectrum 100 FTIR spectrometer, equipped with a MCT detector. Experiments were conducted in a diffuse reflectance cell from Harrick Scientific, type HVC-DR2 with CaF_2 windows that allowed us to perform in situ thermal pretreatments. For each IR spectrum, taken at a resolution of 4 cm^{-1}, 256 scans were added. Prior to each spectrum, the catalyst was reduced in situ in a flow of H_2 for 1 h at 300°C, cooled under He flow, and purged in He at room temperature for 30 min. The background was recorded at this time. Then, the catalyst was exposed to a flow of 5% CO in He for 30 min at room temperature and purged in He for 30 min, prior to obtaining the scans, to remove the contributions from gas phase and weakly adsorbed CO.

Catalytic Measurements

In a typical experiment, a small amount of catalyst (~5-10 mg) was packed in the middle of a 20-cm glass tube reactor and re-reduced in-situ under continuous flow of H_2 at 400°C for 1 h. Subsequently, the temperature was lowered to the reaction temperature (285°C), keeping the catalyst bed under H_2 flow during the entire time of the experiment. When the temperature was stabilized, a 50 μL pulse was injected into the H_2 carrier gas from a sample loop filled with controlled partial pressure of *m*-cresol vapor diluted in N_2 by a separate line. The carrier gas drives the feed from the sample loop over the catalyst bed, introducing a known amount of *m*-cresol (1.3 μmole) in each pulse.

DFT calculations

We have compared the experimental results with DFT calculations performed with methods implemented in the Vienna ab initio Simulation Package (VASP) [123], using the PBE functional for the exchange correlation energy within the generalized gradient approximation (GGA) [53]. The DFT-D3 method was used to account for van der Waals (vdW) interactions [124]. The projector augmented wave method (PAW) was used to describe the electron-ion interactions [54]. The cutoff energy of 400 eV was applied for the plane-wave basis set to represent valence electrons.

The 4x4 Rh(111) surface and the Rh(533) surface with four metal layers and 15 Å of vacuum separating the slabs in the z-direction were used to model the Rh terrace and step sites. The top two metal layers were allowed to relax during the calculations, and the bottom two layers were held fixed to their initial bulk position. The electronic energies were converged within 10^{-6} eV. The geometric structures for all of reactants,

intermediates and products were optimized until the forces on each atom were below 0.01

eV/ Å. A 3×3×1 k-point mesh was used to sample the first Brillouin zone [125]. Transition

state searches were performed using the dimer method [126] with the initial guesses for the

transition state structure and the reaction trajectory obtained through the nudged elastic

band (NEB) method [127].

References

1.   Nie, L.; Resasco, D. E., Kinetics and mechanism of m-cresol hydrodeoxygenation on a Pt/SiO2 catalyst. *J Catal* **2014,** *317*, 22-29.

2.   Zapata, P. A.; Faria, J.; Ruiz, M. P.; Resasco, D. E., Condensation/Hydrogenation of Biomass-Derived Oxygenates in Water/Oil Emulsions Stabilized by Nanohybrid Catalysts. *Top Catal* **2012,** *55* (1-2), 38-52.

3.   Resasco, D. E.; Crossley, S. P., Implementation of concepts derived from model compound studies in the separation and conversion of bio-oil to fuel. *Catal Today* **2015,** *257*, 185-199.

4.   Resasco, D. E.; Wang, B.; Crossley, S., Zeolite-catalysed C-C bond forming reactions for biomass conversion to fuels and chemicals. *Catalysis Science & Technology* **2016,** *6* (8), 2543-2559.

5.   Pham, T. N.; Shi, D. C.; Resasco, D. E., Reaction kinetics and mechanism of ketonization of aliphatic carboxylic acids with different carbon chain lengths over Ru/TiO2 catalyst. *J Catal* **2014,** *314*, 149-158.

6.   Mohan, D.; Pittman, C. U.; Steele, P. H., Pyrolysis of Wood/Biomass for Bio-oil: A Critical Review. *Energy & Fuels* **2006,** *20* (3), 848-889.

7.   Pham, T. N.; Shi, D. C.; Sooknoi, T.; Resasco, D. E., Aqueous-phase ketonization of acetic acid over Ru/TiO2/carbon catalysts. *J Catal* **2012,** *295*, 169-178.

8.   Zapata, P. A.; Faria, J.; Ruiz, M. P.; Jentoft, R. E.; Resasco, D. E., Hydrophobic Zeolites for Biofuel Upgrading Reactions at the Liquid-Liquid Interface in Water/Oil Emulsions. *J Am Chem Soc* **2012,** *134* (20), 8570-8578.

9.   Nguyen, H.; DeJaco, R. F.; Mittal, N.; Siepmann, J. I.; Tsapatsis, M.; Snyder, M. A.; Fan, W.; Saha, B.; Vlachos, D. G., A Review of Biorefinery Separations for Bioproduct Production via Thermocatalytic Processing. *Annual Review of Chemical and Biomolecular Engineering* **2017,** *8* (1), 115-137.

10.   Bu, Q.; Lei, H.; Zacher, A. H.; Wang, L.; Ren, S.; Liang, J.; Wei, Y.; Liu, Y.; Tang, J.; Zhang, Q.; Ruan, R., A review of catalytic hydrodeoxygenation of lignin-derived phenols from biomass pyrolysis. *Bioresource Technology* **2012,** *124*, 470-477.

11.   Bui, T. V.; Sooknoi, T.; Resasco, D. E., Simultaneous Upgrading of Furanics and Phenolics through Hydroxyalkylation/Aldol Condensation Reactions. *Chemsuschem* **2017,** *10* (7), 1631-1639.

12.   Zhang, L.; Pham, T. N.; Faria, J.; Resasco, D. E., Improving the selectivity to C4 products in the aldol condensation of acetaldehyde in ethanol over faujasite zeolites. *Applied Catalysis A: General* **2015,** *504* (Supplement C), 119-129.

13.   Tan, Q. H.; Wang, G. H.; Nie, L.; Dinse, A.; Buda, C.; Shabaker, J.; Resasco, D. E., Different Product Distributions and Mechanistic Aspects of the Hydrodeoxygenation of m-Cresol over Platinum and Ruthenium Catalysts. *ACS Catalysis* **2015,** *5* (11), 6271-6283.

14.   Tran, N.; Uemura, Y.; Chowdhury, S.; Ramli, A., A Review of Bio-Oil Upgrading by Catalytic Hydrodeoxygenation. *Applied Mechanics and Materials* **2014,** *625*, 255-258.

15.   Lee, H.; Kim, H.; Yu, M. J.; Ko, C. H.; Jeon, J.-K.; Jae, J.; Park, S. H.; Jung, S.-C.; Park, Y.-K., Catalytic Hydrodeoxygenation of Bio-oil Model Compounds over Pt/HY Catalyst. *Scientific Reports* **2016,** *6*, 28765.

16.   Pham, T. N.; Shi, D. C.; Resasco, D. E., Evaluating strategies for catalytic upgrading of pyrolysis oil in liquid phase. *Appl Catal B-Environ* **2014,** *145*, 10-23.

17.   Gonzalez-Borja, M. A.; Resasco, D. E., Reaction Pathways in the Liquid Phase Alkylation of Biomass-Derived Phenolic Compounds. *Aiche J* **2015,** *61* (2), 598-609.

18.   Dallas Swift, T.; Nguyen, H.; Anderko, A.; Nikolakis, V.; Vlachos, D. G., Tandem Lewis/Bronsted homogeneous acid catalysis: conversion of glucose to 5-hydoxymethylfurfural in an aqueous chromium(iii) chloride and hydrochloric acid solution. *Green Chemistry* **2015,** *17* (10), 4725-4735.

19.   Nguyen, H.; Nikolakis, V.; Vlachos, D. G., Mechanistic Insights into Lewis Acid Metal Salt-Catalyzed Glucose Chemistry in Aqueous Solution. *ACS Catalysis* **2016,** *6* (3), 1497-1504.

20.   Nguyen, H.; Xiao, N.; Daniels, S.; Marcella, N.; Timoshenko, J.; Frenkel, A.; Vlachos, D. G., Role of Lewis and Brønsted Acidity in Metal Chloride Catalysis in Organic Media: Reductive Etherification of Furanics. *ACS Catalysis* **2017,** *7* (10), 7363-7370.

21.   Swift, T. D.; Nguyen, H.; Erdman, Z.; Kruger, J. S.; Nikolakis, V.; Vlachos, D. G., Tandem Lewis acid/Brønsted acid-catalyzed conversion of carbohydrates to 5-hydroxymethylfurfural using zeolite beta. *J Catal* **2016,** *333*, 149-161.

22.   Herron, J. A.; Vann, T.; Duong, N.; Resasco, D. E.; Crossley, S.; Lobban, L. L.; Maravelias, C. T., A Systems-Level Roadmap for Biomass Thermal Fractionation and Catalytic Upgrading Strategies. *Energy Technology* **2017,** *5* (1), 130-150.

23.   Sartori, G.; Maggi, R., Use of solid catalysts in Friedel-Crafts acylation reactions. *Chem Rev* **2006,** *106* (3), 1077-1104.

24.   Sartori, G.; Maggi, R., Update 1 of: Use of Solid Catalysts in Friedel Crafts Acylation Reactions. *Chem Rev* **2011,** *111*, Pr181-Pr214.

25.   Gumidyala, A.; Sooknoi, T.; Crossley, S., Selective ketonization of acetic acid over HZSM-5: The importance of acyl species and the influence of water. *J Catal* **2016,** *340*, 76-84.

26.   Gumidyala, A.; Wang, B.; Crossley, S., Direct carbon-carbon coupling of furanics with acetic acid over Bronsted zeolites. *Science Advances* **2016,** *2* (9).

27.   Park, D. S.; Joseph, K. E.; Koehle, M.; Krumm, C.; Ren, L. M.; Damen, J. N.; Shete, M. H.; Lee, H. S.; Zuo, X. B.; Lee, B.; Fan, W.; Vlachos, D. G.; Lobo, R. F.; Tsapatsis, M.; Dauenhauer, P. J., Tunable Oleo-Furan Surfactants by Acylation of Renewable Furans. *Acs Central Science* **2016,** *2* (11), 820-824.

28.   Rohan, D.; Canaff, C.; Fromentin, E.; Guisnet, M., Acetylation of anisole by acetic anhydride over a HBEA zeolite - Origin of deactivation of the catalyst. *J Catal* **1998,** *177* (2), 296-305.

29.   Rohan, D.; Canaff, C.; Magnoux, P.; Guisnet, M., Origin of the deactivation of HBEA zeolites during the acylation of phenol with phenylacetate. *Journal of Molecular Catalysis a-Chemical* **1998,** *129* (1), 69-78.

30.   Derouane, E. G.; Crehan, G.; Dillon, C. J.; Bethell, D.; He, H.; Derouane-Abd Hamid, S. B., Zeolite catalysts as solid solvents in fine chemicals synthesis - 2. Competitive adsorption of the reactants and products in the Friedel-Crafts acetylations of anisole and toluene. *J Catal* **2000,** *194* (2), 410-423.

31.   Derouane, E. G.; Dillon, C. J.; Bethell, D.; Derouane-Abd Hamid, S. B., Zeolite Catalysts as Solid Solvents in Fine Chemicals Synthesis. *J Catal* **1999,** *187* (1), 209-218.

32.   Ma, Y. D.; Wang, Q. L.; Jiang, W.; Zuo, B. J., Friedal-Crafts acylation of anisole over zeolite catalysts. *Applied Catalysis a-General* **1997,** *165* (1-2), 199-206.

33.   Kresnawahjuesa, O.; Gorte, R. J.; White, D., Characterization of acylating intermediates formed on H-ZSM-5. *Journal of Molecular Catalysis A: Chemical* **2004,** *208* (1–2), 175-185.

34.   Gaare, K.; Akporiaye, D., Modified zeolites as catalysts in the Friedel-Crafts acylation. *Journal of Molecular Catalysis A: Chemical* **1996,** *109* (2), 177-187.

35.   Singh, A. P.; Pandey, A. K., Acetylation of benzene to acetophenone over zeolite catalysts. *Journal of Molecular Catalysis a-Chemical* **1997,** *123* (2-3), 141-147.

36.   Bezouhanova, C. P., Synthesis of aromatic ketones in the presence of zeolite catalysts. *Applied Catalysis a-General* **2002,** *229* (1-2), 127-133.

37.   Kumari, V. D.; Saroja, G.; Ratnamala, A.; Noorjahan, M.; Subrahmanyam, M., Vapor phase acylation of phenol over H beta, CeH beta and SO42-/ZrO2a. *Reaction Kinetics and Catalysis Letters* **2003,** *79* (1), 43-51.

38.   Vogt, A.; Kouwenhoven, H. W.; Prins, R., Fries Rearrangement over Zeolitic Catalysts. *Applied Catalysis a-General* **1995,** *123* (1), 37-49.

39.   Pouilloux, Y.; Gnep, N. S.; Magnoux, P.; Perot, G., Zeolite-Catalyzed Rearrangement of Phenyl Acetate. *J Mol Catal* **1987,** *40* (2), 231-233.

40.   Chaube, V. D.; Moreau, P.; Finiels, A.; Ramaswamy, A. V.; Singh, A. P., A novel single step selective synthesis of 4-hydroxybenzophenone (4-HBP) using zeolite H-beta. *Catal Lett* **2002,** *79* (1-4), 89-94.

41.   Chaube, V. D.; Moreau, P.; Finiels, A.; Ramaswamy, A. V.; Singh, A. P., Propionylation of phenol to 4-hydroxypropiophenone over zeolite H-beta. *Journal of Molecular Catalysis a-Chemical* **2001,** *174* (1-2), 255-264.

42.   Wang, Q. L.; Ma, Y. D.; Ji, X. D.; Yan, H.; Qiu, Q., Regioselective Acylation of Anisole with Carboxylic-Acids over Hzsm-5 Catalyst. *Journal of the Chemical Society-Chemical Communications* **1995,** (22), 2307-2308.

43.   Loudon, G. M., *Organic Chemistry*. Roberts and Company: 2009.

44.   Neves, I.; Jayat, F.; Magnoux, P.; Perot, G.; Ribeiro, F. R.; Gubelmann, M.; Guisnet, M., Acylation of Phenol with Acetic-Acid over a Hzsm5 Zeolite, Reaction Scheme. *J Mol Catal* **1994,** *93* (2), 169-179.

45.   Cundy, C. S.; Higgins, R.; Kibby, S. A. M.; Lowe, B. M.; Paton, R. M., Para-Selective Fries Rearrangement of Phenyl Acetate in the Presence of Zeolite Molecular-Sieves. *Tetrahedron Letters* **1989,** *30* (17), 2281-2284.

46.   Hoefnagel, A. J.; van Bekkum, H., Direct fries reaction of resorcinol with benzoic acids catalyzed by zeolite H-beta. *Applied Catalysis A: General* **1993,** *97* (2), 87-102.

47.   Freese, U.; Heinrich, F.; Roessner, F., Acylation of aromatic compounds on H-Beta zeolites. *Catal Today* **1999,** *49* (1-3), 237-244.

48.   Cohen, A. J.; Mori-Sanchez, P.; Yang, W. T., Insights into current limitations of density functional theory. *Science* **2008,** *321* (5890), 792-794.

49.   Meng, Q. L.; Fan, H. L.; Liu, H. Z.; Zhou, H. C.; He, Z. H.; Jiang, Z. W.; Wu, T. B.; Han, B. X., Efficient Transformation of Anisole into Methylated Phenols over High-Silica HY Zeolites under Mild Conditions. *Chemcatchem* **2015,** *7* (18), 2831-2835.

50.   Gonzalez, C.; Marin, P.; Diez, F. V.; Ordonez, S., Hydrodeoxygenation of Acetophenone over Supported Precious Metal Catalysts at Mild Conditions: Process Optimization and Reaction Kinetics. *Energy Fuels* **2015,** *29* (12), 8208-8215.

51.   Bui, T. V.; Sooknoi, T.; Resasco, D. E., Simultaneous upgrading of furanics and phenolics via hydroxyalkylation/aldol condensation reactions. *ChemSusChem* **2016,** n/a-n/a.

52.   Kresse, G.; Furthmuller, J., Efficient iterative schemes for ab initio total-energy calculations using a plane-wave basis set. *Phys Rev B* **1996,** *54* (16), 11169-11186.

53.   Perdew, J. P.; Burke, K.; Ernzerhof, M., Generalized gradient approximation made simple. *Phys Rev Lett* **1996,** *77* (18), 3865-3868.

54.   Kresse, G.; Joubert, D., From ultrasoft pseudopotentials to the projector augmented-wave method. *Phys Rev B* **1999,** *59* (3), 1758-1775.

55.   Blochl, P. E., Projector Augmented-Wave Method. *Phys Rev B* **1994,** *50* (24), 17953-17979.

56.   Grimme, S.; Antony, J.; Ehrlich, S.; Krieg, H., A consistent and accurate ab initio parametrization of density functional dispersion correction (DFT-D) for the 94 elements H-Pu. *J Chem Phys* **2010,** *132* (15).

57.   Grimme, S.; Ehrlich, S.; Goerigk, L., Effect of the Damping Function in Dispersion Corrected Density Functional Theory. *J Comput Chem* **2011,** *32* (7), 1456-1465.

58.   Alberti, A.; Cruciani, G.; Galli, E.; Millini, R.; Zanardi, S., In situ X-ray single-crystal study on the dehydration mechanism in the monoclinic polytype of tschernichite, the mineral analog of zeolite beta. *Journal of Physical Chemistry C* **2007,** *111* (12), 4503-4511.

59.   Henkelman, G.; Uberuaga, B. P.; Jonsson, H., A climbing image nudged elastic band method for finding saddle points and minimum energy paths. *J Chem Phys* **2000,** *113* (22), 9901-9904.

60.   Heyd, J.; Scuseria, G. E.; Ernzerhof, M., Hybrid functionals based on a screened Coulomb potential (vol 118, pg 8207, 2003). *J Chem Phys* **2006,** *124* (21).

61.   Heyd, J.; Scuseria, G. E.; Ernzerhof, M., Hybrid functionals based on a screened Coulomb potential. *J Chem Phys* **2003,** *118* (18), 8207-8215.

62.   Tan, Q.; Wang, G.; Long, A.; Dinse, A.; Buda, C.; Shabaker, J.; Resasco, D. E., Mechanistic analysis of the role of metal oxophilicity in the hydrodeoxygenation of anisole. *J Catal* **2017,** *347*, 102-115.

63.   Duong, N.; Tan, Q. H.; Resasco, D. E., Controlling phenolic hydrodeoxygenation by tailoring metal-O bond strength via specific catalyst metal type and particle size selection. *Comptes Rendus Chimie* **2018,** *21* (3-4), 155-163.

64.   Li, Y.; Liu, Z.; Xue, W.; Crossley, S. P.; Jentoft, F. C.; Wang, S., Hydrogenation of o-cresol on platinum catalyst: Catalytic experiments and first-principles calculations. *Applied Surface Science* **2017,** *393*, 212-220.

65.   Li, Y.; Liu, Z.; Crossley, S. P.; Jentoft, F. C.; Wang, S., Effect of hydrogen coverage on hydrogenation of o-cresol on Pt(111). *Applied Surface Science* **2018,** *443*, 575-580.

66.   Talukdar, A. K.; Bhattacharyya, K. G.; Sivasanker, S., Hydrogenation of phenol over supported platinum and palladium catalysts. *Applied Catalysis A: General* **1993,** *96* (2), 229-239.

67.   Liu, H.; Jiang, T.; Han, B.; Liang, S.; Zhou, Y., *Selective Phenol Hydrogenation to Cyclohexanone Over a Dual Supported Pd-Lewis Acid Catalyst*. 2009; Vol. 326, p 1250-2.

68.   Singh, N.; Song, Y.; Gutiérrez, O. Y.; Camaioni, D. M.; Campbell, C. T.; Lercher, J. A., Electrocatalytic Hydrogenation of Phenol over Platinum and Rhodium: Unexpected Temperature Effects Resolved. *ACS Catalysis* **2016,** *6* (11), 7466-7470.

69.   Chou, P.; Vannice, M. A., Benzene hydrogenation over supported and unsupported palladium: II. Reaction model. *J Catal* **1987,** *107* (1), 140-153.

70.   Chou, P.; Vannice, M. A., Benzene hydrogenation over supported and unsupported palladium: I. Kinetic behavior. *J Catal* **1987,** *107* (1), 129-139.

71.   Lin, S. D.; Vannice, M. A., Hydrogenation of Aromatic Hydrocarbons over Supported Pt Catalysts .II. Toluene Hydrogenation. *J Catal* **1993,** *143* (2), 554-562.

72.   Lin, S. D.; Vannice, M. A., Hydrogenation of Aromatic Hydrocarbons over Supported Pt Catalysts .I. Benzene Hydrogenation. *J Catal* **1993,** *143* (2), 539-553.

73.   Lin, S. D.; Vannice, M. A., Hydrogenation of Aromatic Hydrocarbons over Supported Pt Catalysts .III. Reaction Models for Metal Surfaces and Acidic Sites on Oxide Supports. *J Catal* **1993,** *143* (2), 563-572.

74.   Poondi, D.; Albert Vannice, M., Competitive Hydrogenation of Benzene and Toluene on Palladium and Platinum Catalysts. *J Catal* **1996,** *161* (2), 742-751.

75.   Vannice, M. A.; Neikam, W. G., Benzene hydrogenation over a PdAl2O3 catalyst. *J Catal* **1971,** *23* (3), 401-403.

76.   Saeys, M.; Reyniers, M. F.; Neurock, M.; Marin, G. B., Density functional theory analysis of benzene (De)hydrogenation on Pt(111): Addition and removal of the first two H-atoms. *Journal of Physical Chemistry B* **2003,** *107* (16), 3844-3855.

77.   Castano, P.; Arandes, J. M.; Pawelec, B.; Fierro, J. L. G.; Gutierrez, A.; Bilbao, J., Kinetic model discrimination for toluene hydrogenation over noble-metal-supported catalysts. *Ind. Eng. Chem. Res.* **2007,** *46* (23), 7417-7425.

78.   Borodzinski, A.; Bonarowska, M., Relation between crystallite size and dispersion on supported metal catalysts. *Langmuir* **1997,** *13* (21), 5613-5620.

79.   Cortright, R.; Dumesic, J., Kinetics of heterogeneous catalytic reactions: Analysis of reaction schemes. **2001**.

80.   Dumesic, J. A., *The microkinetics of heterogeneous catalysis*. An American Chemical Society Publication: 1993.

81.   Saeys, M.; Reyniers, M.-F.; Thybaut, J.; Neurock, M.; Marin, B., *First-principles based kinetic model for the hydrogenation of toluene*. 2005; Vol. 236, p 129-138.

82.   Spencer J. Carey, W. Z., Zhongtian Mao, Charles T. Campbell, The Energetics of Adsorbed Phenol on Ni(111) and Pt(111) by Calorimetry. **2018**.

83.   Honkela, M. L.; Bjork, J.; Persson, M., Computational study of the adsorption and dissociation of phenol on Pt and Rh surfaces. *Physical Chemistry Chemical Physics* **2012,** *14* (16), 5849-5854.

84.   Duong, N. N.; Wang, B.; Sooknoi, T.; Crossley, S. P.; Resasco, D. E., Enhancing the Acylation Activity of Acetic Acid by Formation of an Intermediate Aromatic Ester. *ChemSusChem* **2017,** *10* (13), 2823-2832.

85.   Rensel, D. J.; Rouvimov, S.; Gin, M. E.; Hicks, J. C., Highly selective bimetallic FeMoP catalyst for C–O bond cleavage of aryl ethers. *J Catal* **2013,** *305*, 256-263.

86.   Do, P. T. M.; Foster, A. J.; Chen, J.; Lobo, R. F., Bimetallic effects in the hydrodeoxygenation of meta-cresol on [gamma]-Al2O3 supported Pt-Ni and Pt-Co catalysts. *Green Chemistry* **2012,** *14* (5), 1388-1397.

87.   Lee, K.; Gu, G. H.; Mullen, C. A.; Boateng, A. A.; Vlachos, D. G., Guaiacol Hydrodeoxygenation Mechanism on Pt(111): Insights from Density Functional Theory and Linear Free Energy Relations. *ChemSusChem* **2015,** *8* (2), 315-322.

88.   Robinson, A.; Ferguson, G. A.; Gallagher, J. R.; Cheah, S.; Beckham, G. T.; Schaidle, J. A.; Hensley, J. E.; Medlin, J. W., Enhanced Hydrodeoxygenation of m-Cresol over Bimetallic Pt–Mo Catalysts through an Oxophilic Metal-Induced Tautomerization Pathway. *ACS Catalysis* **2016,** *6* (7), 4356-4368.

89.   Robinson, A. M.; Mark, L.; Rasmussen, M. J.; Hensley, J. E.; Medlin, J. W., Surface Chemistry of Aromatic Reactants on Pt- and Mo-Modified Pt Catalysts. *The Journal of Physical Chemistry C* **2016,** *120* (47), 26824-26833.

90.   de Souza, P. M.; Rabelo-Neto, R. C.; Borges, L. E.; Jacobs, G.; Davis, B. H.; Resasco, D. E.; Noronha, F. B., Hydrodeoxygenation of phenol over Pd catalysts. Effect of support on reaction mechanism and catalyst deactivation. *ACS Catalysis* **2017,** *7* (3), 2058-2073.

91.   de Souza, P. M.; Nie, L.; Borges, L. E.; Noronha, F. B.; Resasco, D. E., Role of Oxophilic Supports in the Selective Hydrodeoxygenation of m-Cresol on Pd Catalysts. *Catal Lett* **2014,** *144* (12), 2005-2011.

92.   Griffin, M. B.; Ferguson, G. A.; Ruddy, D. A.; Biddy, M. J.; Beckham, G. T.; Schaidle, J. A., Role of the Support and Reaction Conditions on the Vapor-Phase Deoxygenation of m-Cresol over Pt/C and Pt/TiO2 Catalysts. *ACS Catalysis* **2016,** *6* (4), 2715-2727.

93.   Furimsky, E., Catalytic hydrodeoxygenation. *Applied Catalysis A: General* **2000,** *199* (2), 147-190.

94.   Hensley, A. J. R.; Hong, Y. C.; Zhang, R. Q.; Zhang, H.; Sun, J. M.; Wang, Y.; McEwen, J. S., Enhanced Fe2O3 Reducibility via Surface Modification with Pd: Characterizing the Synergy within Pd/Fe Catalysts for Hydrodeoxygenation Reactions. *Acs Catalysis* **2014,** *4* (10), 3381-3392.

95.   Zhao, C.; Kou, Y.; Lemonidou, A. A.; Li, X. B.; Lercher, J. A., Highly Selective Catalytic Conversion of Phenolic Bio-Oil to Alkanes. *Angew. Chem.-Int. Edit.* **2009,** *48* (22), 3987-3990.

96.   Zhao, C.; Yu, Y. Z.; Jentys, A.; Lercher, J. A., Understanding the impact of aluminum oxide binder on Ni/HZSM-5 for phenol hydrodeoxygenation. *Appl Catal B-Environ* **2013,** *132*, 282-292.

97.   Zhu, X. L.; Nie, L.; Lobban, L. L.; Mallinson, R. G.; Resasco, D. E., Efficient Conversion of m-Cresol to Aromatics on a Bifunctional Pt/HBeta Catalyst. *Energy Fuels* **2014,** *28* (6), 4104-4111.

98.   Zhao, C.; He, J.; Lemonidou, A. A.; Li, X.; Lercher, J. A., Aqueous-phase hydrodeoxygenation of bio-derived phenols to cycloalkanes. *J Catal* **2011,** *280* (1), 8-16.

99.   Zhao, C.; Kou, Y.; Lemonidou, A. A.; Li, X.; Lercher, J. A., Hydrodeoxygenation of bio-derived phenols to hydrocarbons using RANEY® Ni and Nafion/SiO 2 catalysts. *Chemical Communications* **2010,** *46* (3), 412-414.

100.   Zhao, C.; Lercher, J. A., Selective Hydrodeoxygenation of Lignin-Derived Phenolic Monomers and Dimers to Cycloalkanes on Pd/C and HZSM-5 Catalysts. *Chemcatchem* **2012,** *4* (1), 64-68.

101.   Tan, Q.; Wang, G.; Nie, L.; Dinse, A.; Buda, C.; Shabaker, J.; Resasco, D. E., Different product distributions and mechanistic aspects of the hydrodeoxygenation of m-cresol over platinum and ruthenium catalysts. *ACS Catalysis* **2015,** *5* (11), 6271-6283.

102.   Nie, L.; de Souza, P. M.; Noronha, F. B.; An, W.; Sooknoi, T.; Resasco, D. E., Selective conversion of m-cresol to toluene over bimetallic Ni–Fe catalysts. *Journal of Molecular Catalysis A: Chemical* **2014,** *388*, 47-55.

103.   Nie, L.; Resasco, D. E., Kinetics and mechanism of m-cresol hydrodeoxygenation on a Pt/SiO 2 catalyst. *J Catal* **2014,** *317*, 22-29.

104.   Maire, G.; Plouidy, G.; Prudhomme, J. C.; Gault, F. G., The mechanisms of hydrogenolysis and isomerization of hydrocarbons on metals. *J Catal* **1965,** *4* (5), 556-569.

105.   Corolleur, C.; Corolleur, S.; Gault, F., The mechanisms of hydrogenolysis and isomerization of hydrocarbons on metals. VI. Isomerization of labeled hexanes on a 0.2% platinum-alumina catalyst. *J Catal* **1972,** *24* (3), 385-400.

106.   Gault, F., Mechanisms of skeletal isomerization of hydrocarbons on metals. *Advances in Catalysis* **1981,** *30*, 1-95.

107.   Dartigues, J. M.; Chambellan, A.; Gault, F., Isomerization on metals. Correlation between metal particle size and reaction mechanisms. *J Am Chem Soc* **1976,** *98* (3), 856-857.

108.   Gault, F., Effet de la dispersion du platine sur le support dans lhydrogenolyse des hydrocarbures cyclopentaniques. *Comptes Rendus Hebdomadaires Des Seances De L Academie Des Sciences* **1957,** *245* (19), 1620-1623.

109.   Nie, L. Catalytic hydrodeoxygenation of phenolic compounds of importance in bio-oil upgrading Doctoral Dissertation, University of Oklahoma, 2014.

110.   Foster, A. J.; Do, P. T. M.; Lobo, R. F., The Synergy of the Support Acid Function and the Metal Function in the Catalytic Hydrodeoxygenation of m-Cresol. *Top Catal* **2012,** *55* (3), 118-128.

111. Greeley, J.; Nørskov, J. K., A general scheme for the estimation of oxygen binding energies on binary transition metal surface alloys. *Surface science* **2005,** *592* (1), 104-111.

112. Watwe, R. M.; Cortright, R. D.; Nørskov, J. K.; Dumesic, J. A., Theoretical Studies of Stability and Reactivity of C2 Hydrocarbon Species on Pt Clusters, Pt(111), and Pt(211). *The Journal of Physical Chemistry B* **2000,** *104* (10), 2299-2310.

113. Kleis, J.; Greeley, J.; Romero, N. A.; Morozov, V. A.; Falsig, H.; Larsen, A. H.; Lu, J.; Mortensen, J. J.; Dułak, M.; Thygesen, K. S.; Nørskov, J. K.; Jacobsen, K. W., Finite Size Effects in Chemical Bonding: From Small Clusters to Solids. *Catal Lett* **2011,** *141* (8), 1067-1071.

114. Mavrikakis, M.; Hammer, B.; Nørskov, J. K., Effect of Strain on the Reactivity of Metal Surfaces. *Phys Rev Lett* **1998,** *81* (13), 2819-2822.

115. Kitchin, J. R.; Nørskov, J. K.; Barteau, M. A.; Chen, J. G., Role of Strain and Ligand Effects in the Modification of the Electronic and Chemical Properties of Bimetallic Surfaces. *Phys Rev Lett* **2004,** *93* (15), 156801.

116. Koningsberger, D.; van't Blik, H.; van Zon, J.; Huizinga, T.; Vis, J.; Prins, R., An extended X-ray absorption fine structure spectroscopy study of a highly dispersed rhodium/aluminum oxide catalyst: the influence of carbon monoxide chemisorption on the topology of rhodium. *Journal of physical chemistry* **1983,** *87* (13), 2264-2267.

117. Yates, D. J. C.; Murrell, L. L.; Prestridge, E. B., Ultradispersed rhodium rafts: Their existence and topology. *J Catal* **1979,** *57* (1), 41-63.

118. Rice, C. A.; Worley, S. D.; Curtis, C. W.; Guin, J. A.; Tarrer, A. R., The oxidation state of dispersed Rh on Al2O3. *The Journal of Chemical Physics* **1981,** *74* (11), 6487-6497.

119. Haller, G. L.; Resasco, D. E., Metal–support interaction: Group VIII metals and reducible oxides. *Advances in Catalysis* **1989,** *36*, 173-235.

120. Trautmann, S.; Baerns, M., Infrared Spectroscopic Studies of CO Adsorption on Rhodium Supported by SiO2, Al2O3, and TiO2. *J Catal* **1994,** *150* (2), 335-344.

121. Toolenaar, F. J. C. M.; Stoop, F.; Ponec, V., On electronic and geometric effects of alloying. *J Catal* **1983,** *82* (1), 1-12.

122. Abild-Pedersen, F.; Lytken, O.; Engbæk, J.; Nielsen, G.; Chorkendorff, I.; Nørskov, J. K., Methane activation on Ni (111): Effects of poisons and step defects. *Surface Science* **2005,** *590* (2), 127-137.

123. Kresse, G.; Hafner, J., Ab initio molecular-dynamics simulation of the liquid-metal–amorphous-semiconductor transition in germanium. *Phys. Rev. B* **1994,** *49* (20), 14251-14269.

124. Grimme, S.; Antony, J.; Ehrlich, S.; Krieg, H., A consistent and accurate ab initio parametrization of density functional dispersion correction (DFT-D) for the 94 elements H-Pu. *J. Chem. Phys.* **2010,** *132* (15), 154104.

125. Monkhorst, H. J.; Pack, J. D., Special points for Brillouin-zone integrations. *Phys. Rev. B* **1976,** *13* (12), 5188-5192.

126. Henkelman, G.; Jónsson, H., A dimer method for finding saddle points on high dimensional potential surfaces using only first derivatives. *J. Chem. Phys.* **1999,** *111* (15), 7010-7022.

127. Henkelman, G.; Jónsson, H., Improved tangent estimate in the nudged elastic band method for finding minimum energy paths and saddle points. *J. Chem. Phys.* **2000,** *113* (22), 9978-9985.